Phase-Transformation Kinetics of TiCr$_2$ Laves Phases

Wolfgang Baumann

Phase-Transformation Kinetics of TiCr₂ Laves Phases

Von der Fakultät Chemie der Universität Stuttgart
zur Erlangung der Würde eines Doktors der Naturwissenschaften (Dr. rer. nat.)
genehmigte Abhandlung

vorgelegt von

Wolfgang Baumann

aus Zipplingen

Hauptberichter:	Prof. Dr. Ir. E. J. Mittemeijer
Mitberichter:	Prof. Dr. J. Bill
Prüfungsvorsitzender:	Prof. Dr. R. Niewa

Tag der Einreichung:	25.05.2010
Tag der mündlichen Prüfung:	26.07.2010

MAX-PLANCK-INSTITUT FÜR METALLFORSCHUNG IN STUTTGART
INSTITUT FÜR MATERIALWISSENSCHAFT DER UNIVERSITÄT STUTTGART

Stuttgart 2010

Contents

Chapter 1

General introduction

1.1 Global view on Laves phases

Intermetallics are metallic compounds of metals which have a crystal structure different from the involved metallic components. Laves phases (AB_2) are the largest group of intermetallic phases. Especially transition-metal Laves phases are very promising candidates as basic components for the design of new *metallic* materials with special properties; i.e. metallic materials of high strength, corrosion resistance and long-term stability at temperatures well above 1000 °C [1-4]. For example, current research on turbine steels considers the use of fine Laves-phase precipitates for improving the fatigue resistance. The interest in Laves phases not only increased due to current research on turbine steels, but also because of their promising properties for the use as functional materials like hydrogen-storage materials in nickel-metal hydride batteries based on the $Zr(V, Mn, Ni)_2$ Laves phase, superconducting materials (e.g. $(Hf, Zr)V_2$) and magnetic materials (e.g. $(Hf, Zr, Ti, Nb)Fe_2$) [5, 6].

Consequently, Laves phases are an upcoming class of materials with a wide range of properties competing with commercial materials. But in comparison to (most) important commercial materials Laves phases are not well understood (see Section 1.4). One reason for the insufficient knowledge is that minor impurities (e.g. H, C, N and O) strongly influence the stability and the properties of Laves phases. Because of this, information on stability, structure or properties of Laves phases is generally incomplete and unreliable. Therefore, for basic investigations it is essential to produce pure homogeneous samples without impurities (see Sections 1.5 and 1.6).

However, in the past several geometrical concepts to describe the stability of Laves phases have been derived. These concepts rely in particular on symmetry, packing density, or electronic factors. None of these concepts is valid for all the compounds of the large class of Laves phases [5], and a complete and consistent description of Laves phases is still lacking.

The most prominent crystal structures (see Sections 1.2, 3.1.1 and 5.1.1) of Laves phases can be described by different stacking variants of layers; in literature it

was proposed that the temperature dependent phase-transformations between these polytypes occur by a *synchroshear mechanism*, which involves the cooperative, *synchronous* movement of Shockley-partial dislocations [7-9] (see Sections 1.4.2.1, 3.1 and 5.1). In order to tailor the properties of *new class* materials it is necessary to understand the mechanism and the kinetics of the phase transformations between these different stacking variants since a precise tuning of materials is only feasible by the understanding of the corresponding phase transformations.

This means the investigation of the phase transformations of Laves phases is of great technological importance, but also very interesting from a scientific point of view, since the proposed mechanism of the phase transformations still has to be confirmed or modified.

The $TiCr_2$ Laves phases are well-suited model system for the investigation of the mechanism and the kinetics of the phase transformations in Laves phases because of the occurrence of the three most prominent Laves phase polytypes (see next section) as a function of temperature. Furthermore, the phase transformation temperatures between the Laves-phase polytypes are comparatively *low* for Laves phases.

1.2 Crystal structure of Laves phases

The three most prominent Laves-phase polytypes are the cubic $MgCu_2$ modification (C15/*Strukturbericht designation*), the dihexagonal $MgNi_2$ modification (C36) and the hexagonal $MgZn_2$ modification (C14). The unit cells of the different structure types are shown in Figure 1.1. For a more detailed description of the crystal structures see Sections 1.2, 3.1.1 and 5.1.1.
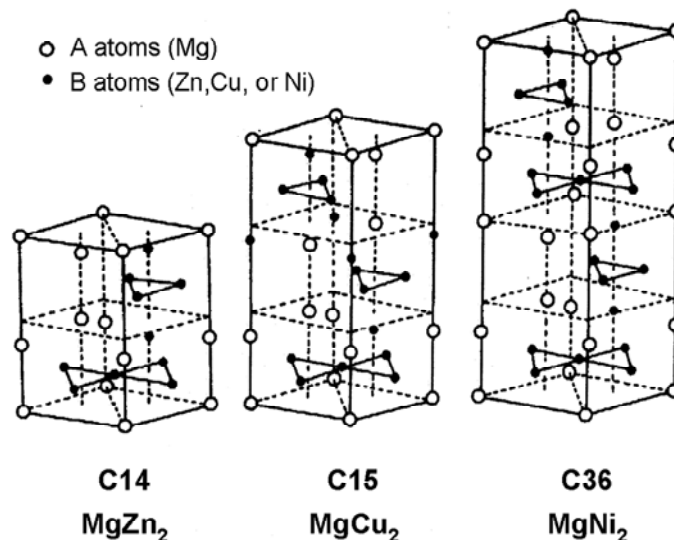
Figure 1.1: Crystal structures of the three Laves phase prototypes in a hexagonal setting [5].

1.3 Chemical bonding type in Laves phases

Zhu *et al*. [10-12] gathered data for the enthalpies of formation of Laves phases and analysed them systematically. They found that the enthalpies of formation vary from 0 up to 350 kJ/mol, which is the typical range for metallic, covalent and ionic bonding. Finally they concluded that the chemical bonds for both non-transition metal Laves phases and transition metal Laves phases are very complicated and most likely of mixed metallic-covalent-ionic character [5].

Furthermore, charge density distribution calculations for the Laves phase *prototypes* $MgZn_2$ and $MgCu_2$ showed that there is a coexistence of covalent, metallic and ionic bonding [5, 13, 14].

1.4 Literature review

In this section a short literature review will be given which concerns in particular with factors controlling the stability of Laves phases.

1.4.1 Phase/polytype stability

It is generally accepted that geometrical aspects like the size ratio of the atoms A and B as well as the electronic factors like the number of valence electrons of the atoms A and B strongly influence the occurrence of a Laves phase. In literature there exist various simple models which are based on these parameters and have the ambition to predict the stable Laves phase polytype [5]. In the following some of these factors/models will be briefly presented. Subsequently, it will be shown that none of the models provides a complete and consistent description valid for all Laves phases.

1.4.1.1 Atom size factors

It is well established that models for the formation of Laves phases including only one of the above-mentioned (geometrical or electronical) factors are not successful [1]. Due to geometrical reasons the closed packing of hard spheres is achieved for an ideal radius ratio of $r_A/r_B = 1.225$ [15-18].
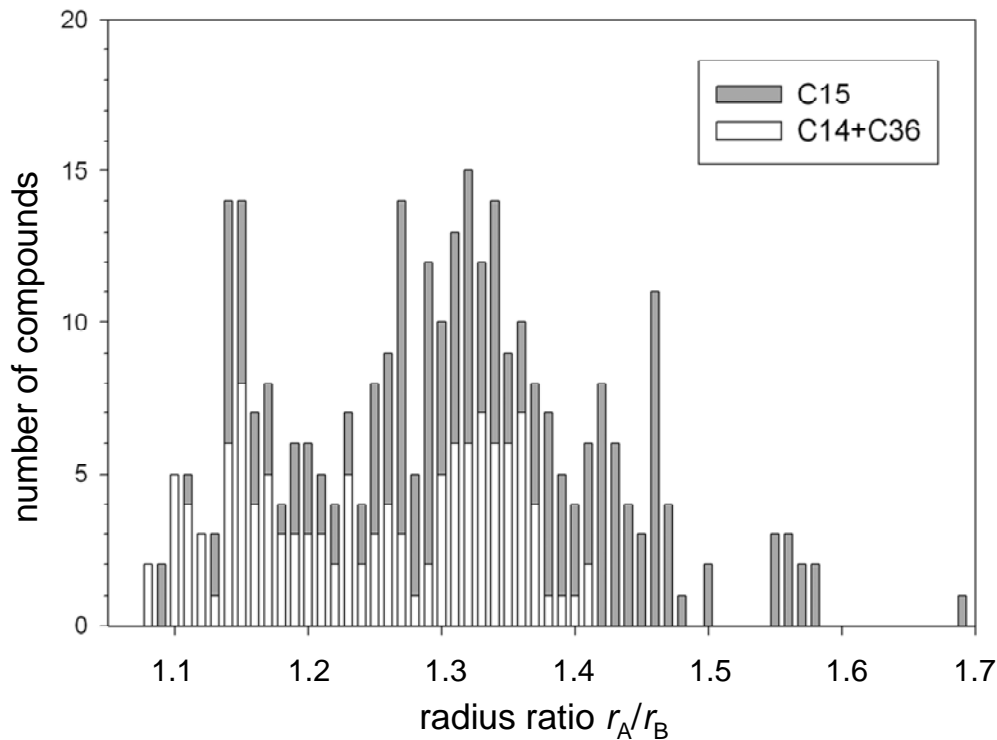
Figure 1.2: Frequency of Laves phase polytype versus atomic radius ratio r_A/r_B [5, 19].

As it is shown in Figure 1.2, in reality the radius ratio between Laves-phase forming atoms varies from 1.05 to 1.68 and evidently there is no correlation between the atom size ratio and the Laves-phase polytype formed, in particular if one additionally considers the C14 Laves phases of $YbCu_2$ and KAu_2 with the very large size ratios of 1.517 and 1.648, respectively [20] (not included in Figure 1.2). The deviations from the ideal radius ratio were explained by the author of Ref. [21] by a deviation of the radii of the atoms in the Laves phase from the radii of the pure metals. Thus it was concluded that the atoms contract or expand such that the ideal radius ratio is fulfilled for a particular pair of elements constituting a Laves phase. Already Laves himself [22, 23] (also Schulze [17] and Dehlinger [24]) mentioned and discussed the discrepancies between the atomic radii in the Laves phases from those of pure metals [5].

Note that metals with a radius ratio higher or smaller than the above-mentioned radius-ratio range have not been observed to form Laves phases.

1.4.1.2 Valence electron concentration VEC

Already Laves tried to correlate the stable Laves phase polytype with the average number of valence electrons, i.e. he thought about the possibility that the electronic structure affects the resulting structure [25, 26]. In Figure 1.3 the frequency of Laves phase structure type as a function of the valence electron concentration VEC is shown. Evidently a prediction of the stable structure solely from the valence electron concentration is impossible.
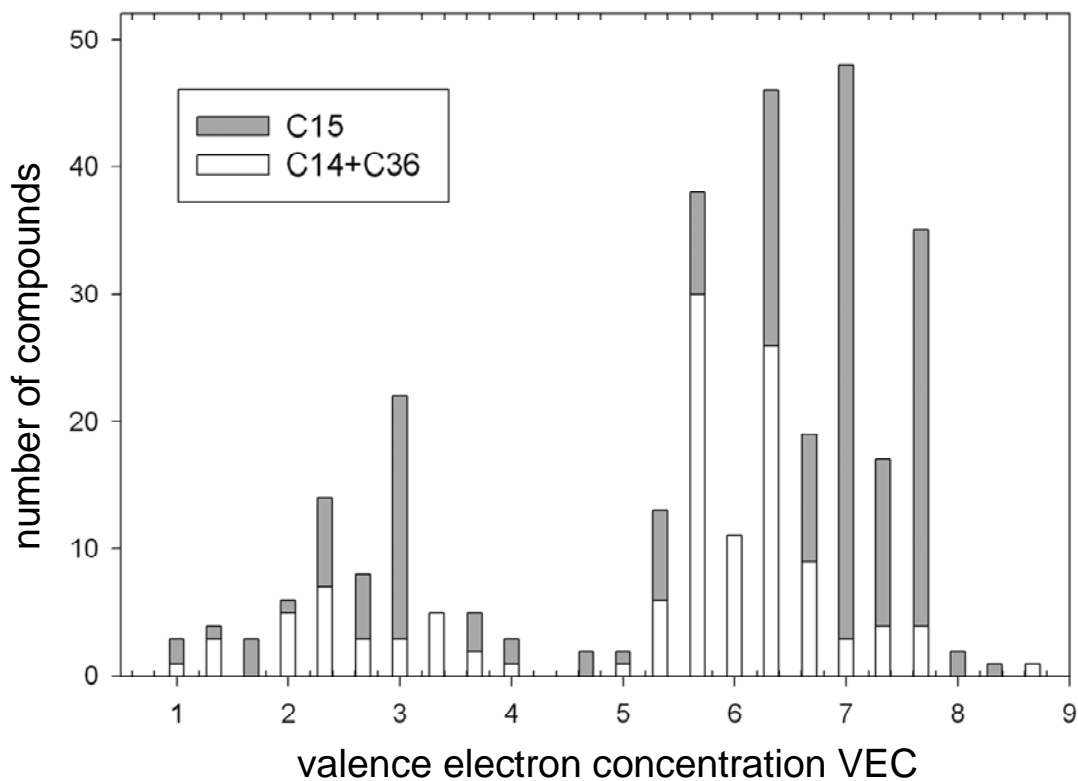
Figure 1.3: Frequency of Laves phase structure type versus valence electron concentration VEC [5, 19].

Anyhow, Laves and Witte [25] found a clear dependence of the stable structure type on the valence electron concentration VEC (see Figure 1.4) but such a simple behaviour is only valid for particular Laves phase alloy systems.
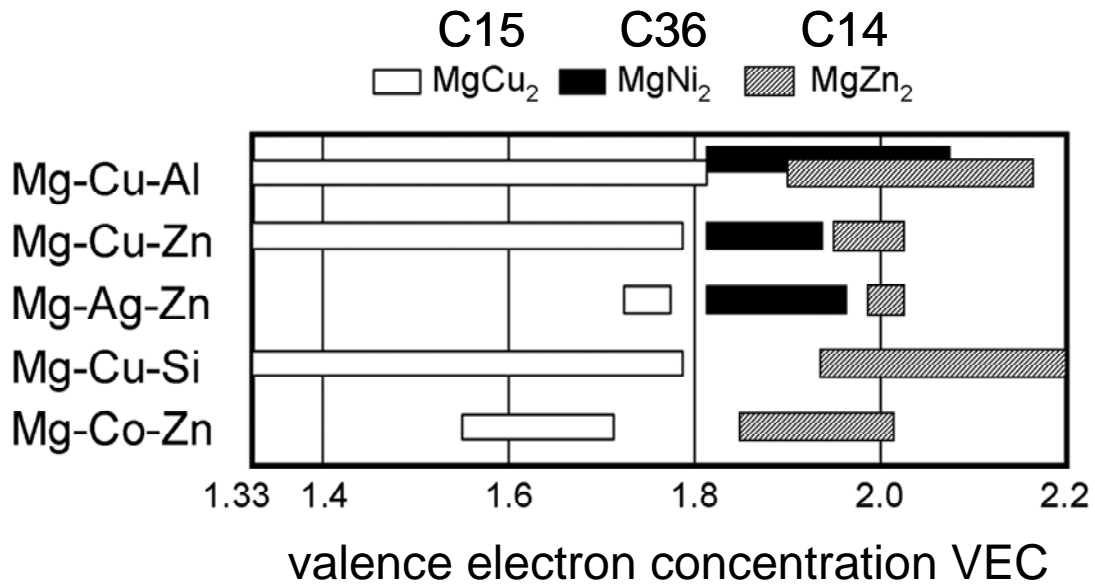
Figure 1.4: Stable Laves phase structure type as a function of the valence electrons per atom (VEC) [5, 25] for ternary Mg-based Laves phase alloys.

The authors of [27-29] also found such a simple correlation for some transition metal Laves phases (see Figure 1.5) using the average number of 3d + 4s electrons per atom as the VEC. Also in this case the correlation is only valid for the particular alloys investigated, since other transition metal Laves phases like $ZrFe_2$ and $TiCo_2$, which have the cubic C15 structure at the stoichiometric composition, obviously are not in agreement with the diagram (compare Figure 1.5).
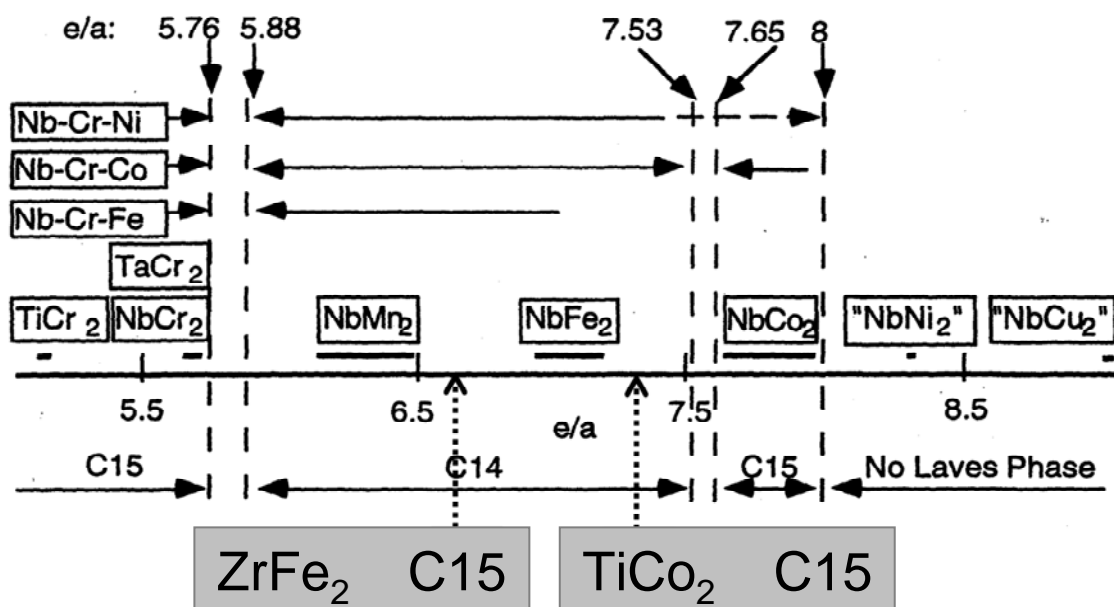
Figure 1.5: Stable Laves phase structure type as a function of the valence electrons per atom for transition metal Laves phases (e/a = VEC) [5, 27, 28].

1.4.1.3 Structure maps

So-called compound-formation diagrams or rather *structure maps* have the aim to predict the stable Laves phase type in terms of *several* structure controlling factors like atom size, radius ratio r_A/r_B, atom numbers, VECs or cohesive energies [4, 30-38]. That is the structure maps try to extend the simple predictions presented above. In Figure 1.6 the radius ratio r_A/r_B is plotted over the valence electron concentration VEC. In this plot the Laves phase of C14 occurs within a limited area of radius ratio and valence electron concentration VEC.

However, this structure map again provides no general description which is valid for all Laves phases. If, for example the C14-ZrAl$_2$ Laves phase (radius ratio $r_A/r_B = 1.19$ /VEC = 3.33) is added to the plot it is located outside the C14 area.
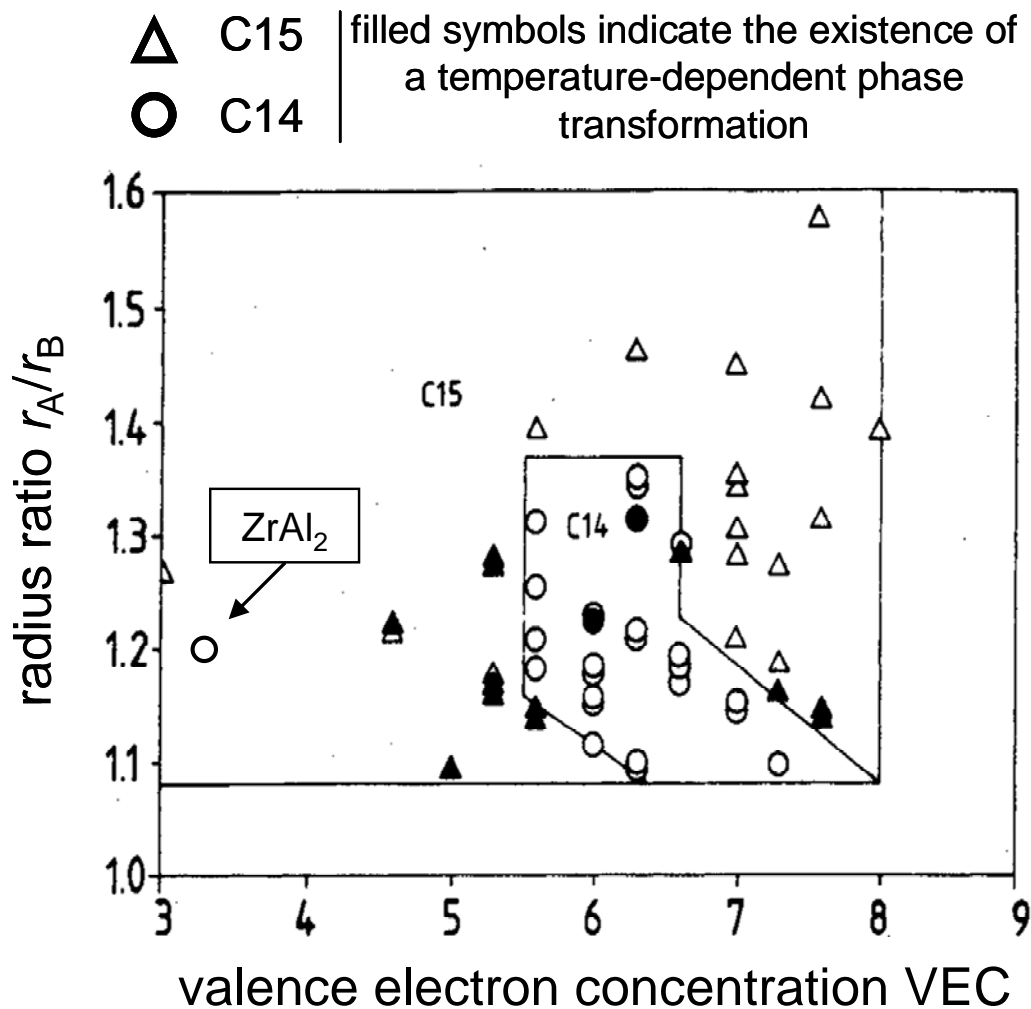
Figure 1.6: Structure map showing the stability ranges of hexagonal C14 and cubic C15 Laves phases for binary transition alloys as a function of the radius ratio r_A/r_B versus the VECs (redrawn after [5]; [38]).

Pettifor established the Mendeleev number M as a phenomenological number which sorts the elements of the periodic table in a one-dimensional string [36, 37, 39, 40]. In Figure 1.7 the Mendeleev number of the element B, M_B, (of the AB_2 Laves phases) is plotted against the Mendeleev number of the element A, M_A, for transition metal Laves phases. Figure 1.7 shows that the Laves phases consisting of the transition metals are systematically situated above the diagonal $M_A = M_B$. Additionally all Laves phase modifications (i.e. C14/C15 and C36) are arranged in well defined areas. However, if the three *prototype* Laves phases $MgCu_2$ (C15), $MgZn_2$ (C14) and $MgNi_2$ (C36) (with Mg as non-transition metal) are included into the structure map, the systematic arrangement clearly breaks down (compare Figure 1.7).
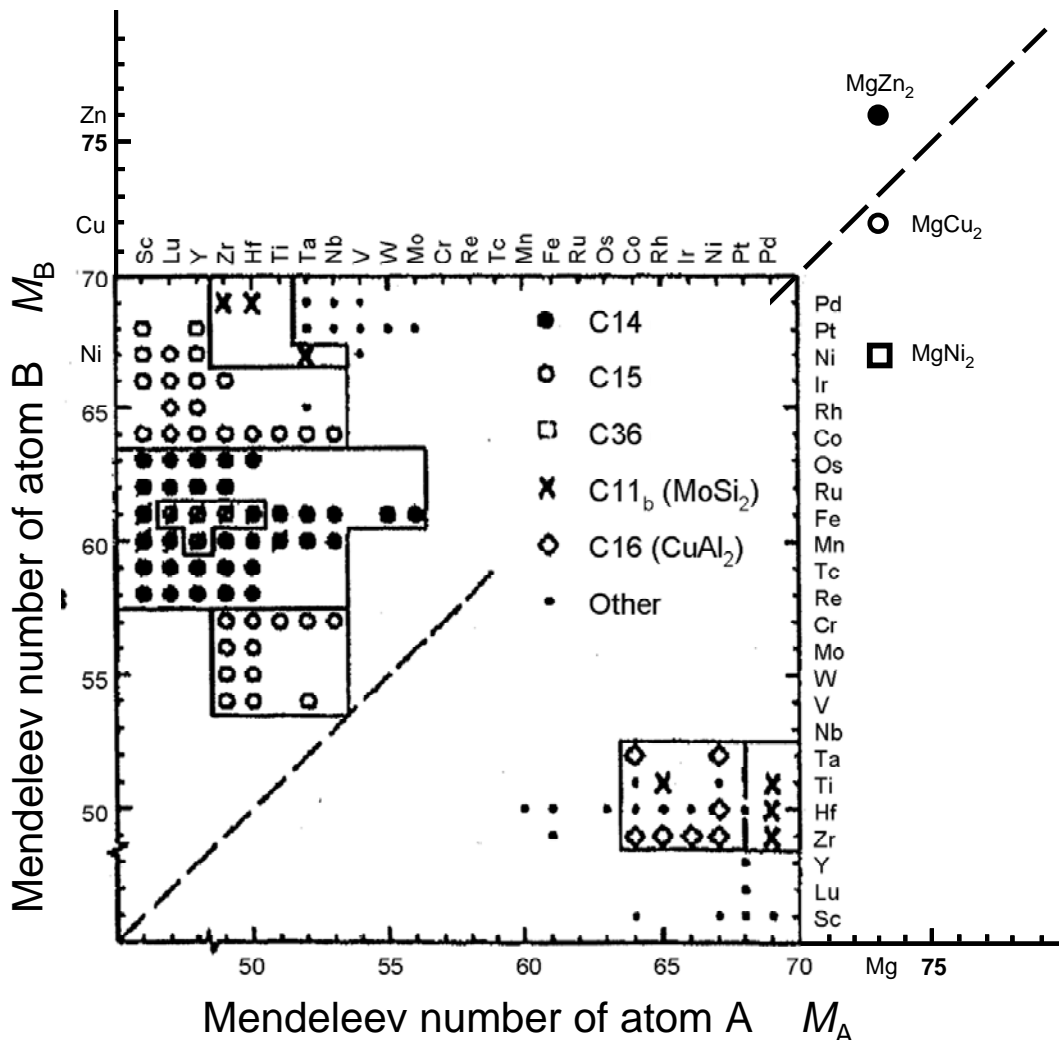
Figure 1.7: Structure map showing the stability ranges of the structures indicated as a function of the Mendeleev numbers of the atoms A and B (redrawn after [5]; [30]).

1.4.2 Temperature dependent phase transformations

Several binary Laves-phase systems occur with more than one stable Laves-phase polytype. The different Laves-phase modifications are stable as a function of temperature, i.e. they exhibit a temperature-dependent phase transformation. One example is the Ti-Cr system which is shown in Figure 1.8. In the Ti-Cr system the cubic C15 phase is stable at low temperatures, the hexagonal C14 phase is stable at high temperatures and the dihexagonal C36 phase is stable in between. Further systems which show a temperature-dependent Laves-phase structure change are Cr-Ta, Cr-Hf, Cr-Zr, Hf-Mo and Ta-V [41]. In all these systems the cubic C15 phase is stable at low temperatures and the hexagonal C14 phase is stable at high temperatures. Furthermore, in several of the above-mentioned systems the C36 phase exists as intermediate-temperature phase [41], like in the Ti-Cr system.

Note that the Mg-Th system is the only known system which is inconsistent with these regularities. Peterson *et al.* stated that in this system the dihexagonal C36 Laves-phase polytype is stable at low temperatures and transforms to the cubic C15 phase at elevated temperatures [42]. However, years later Peterson himself (as co-author) arrived at the conclusion that it is very doubtful that the observed C36 polytype is the stable phase at low temperatures [43].
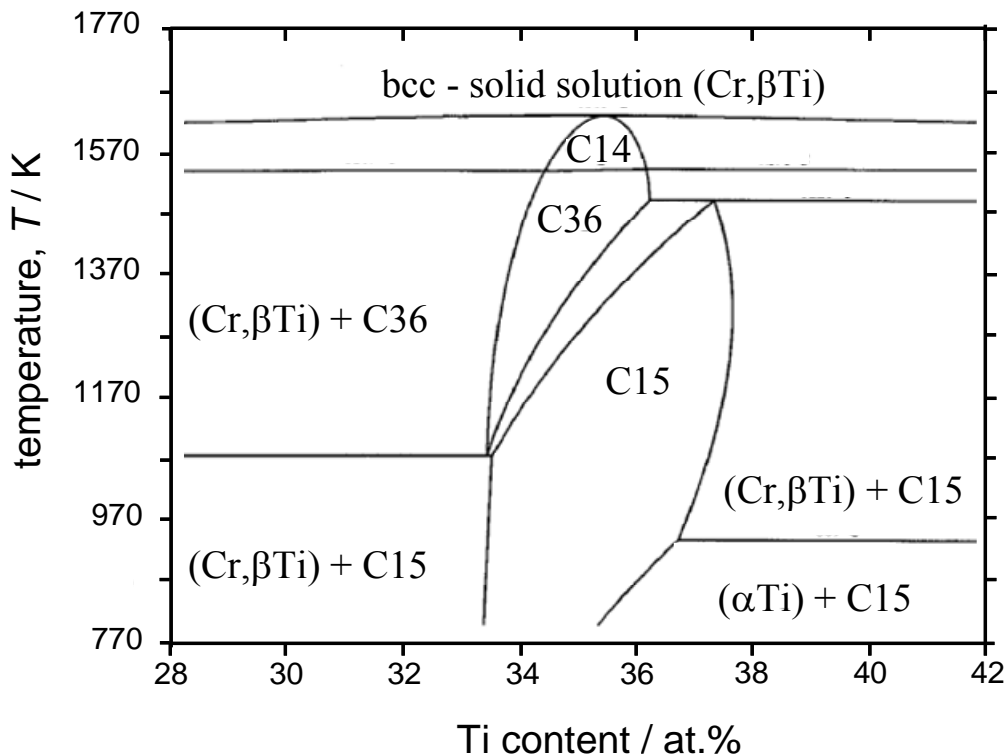
Figure 1.8: Laves-phase containing composition range of the Ti-Cr phase diagram (redrawn after [44]).

1.4.2.1 Phase transformation mechanism - synchroshear

The temperature dependent phase transformations are thought to occur by a special shear mechanism; the so-called *synchroshear* mechanism. The concept of synchroshear is based on several experimental observations. A historical survey of the concept of synchroshear is given in Sections 3.1 and 5.1.

1.5 Synthesis of TiCr$_2$ Laves phase alloys

The synthesis of pure, homogeneous TiCr$_2$-Laves phase alloys with well-defined compositions is very difficult, because of high temperatures involved, the danger of sample contamination (e.g. oxygen) and evaporation of the constituents.

In the following an overview of the sub-steps involved in the synthesis of the Laves phase alloys will be presented.

1.5.1 Preparation of button ingots by arc melting

For the production of the samples high-purity metals were used (Ti 99.999 %; Cr 99.999 %). The raw alloys were produced as button ingots in an arc melting furnace under titanium-gettered argon atmosphere including a water cooled copper hearth. The oxygen content of the argon atmosphere was controlled by an oxygen measurement facility.

Subsequently the alloy metals were melted down; the produced button ingots (see Figure 1.9) have been remelted and flipped several times in order to ensure macroscopic chemical homogeneity of the samples.

Figure 1.9: Top (left) and bottom side (right) of a TiCr$_2$ button ingot produced by arc melting.

1.5.2 Homogenisation of the button ingots

The as-cast samples were subjected to further heat treatments to ensure also micro-scopic chemical homogeneity of the Laves phase (as single phase alloy). For that the samples (ingots) were annealed for 50 h at 1668 K (in the bcc-solid solution region, see Figure 1.8) to ensure chemical homogeneity. Afterwards the samples were annealed for 50 h at 1470 K (in the C36 Laves-phase region). These heat treatments were done in a vacuum melting and casting facility (cf. Section 1.5.2.1).

1.5.2.1 Experimental setup and execution of the test

As furnace for the homogenization treatments the vacuum melting and casting facility VSG002 (PVA/formerly Balzers), which is an induction furnace, was used. The experimental setup of the VSG002 is shown in Figures 1.10 and 1.11.
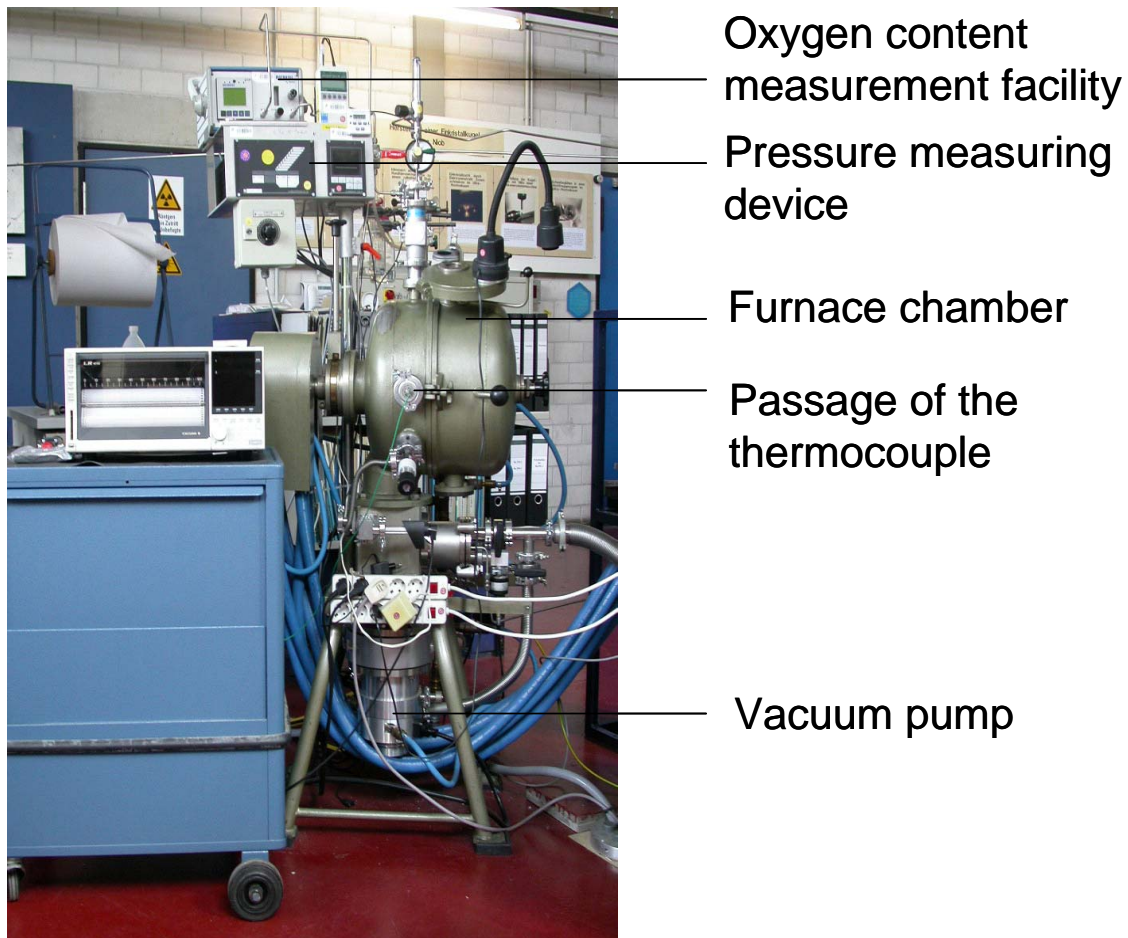
Figure 1.10: VSG002 - induction furnace; experimental setup.
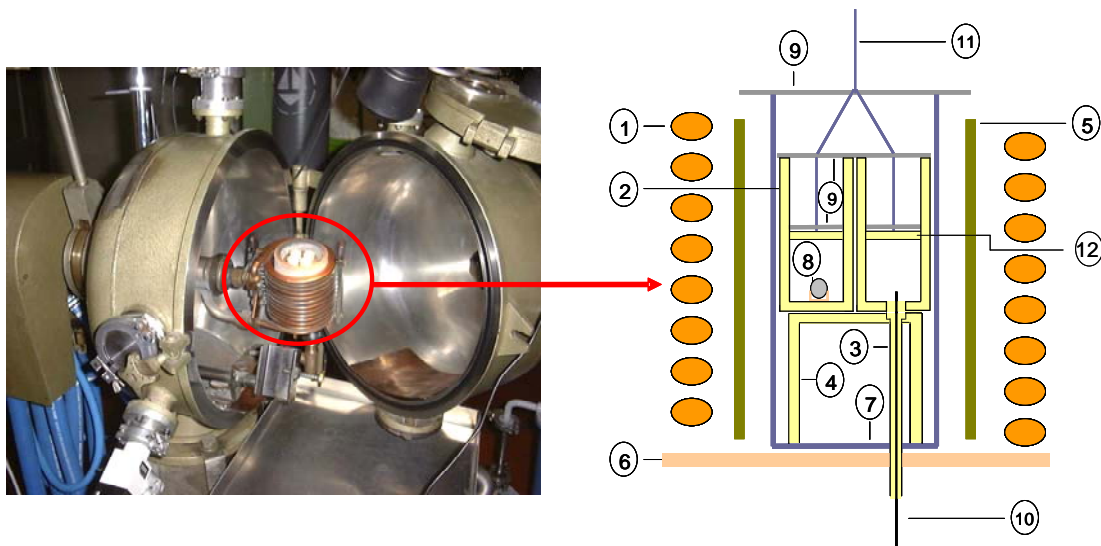
1. Cu-induction coil
2. Al_2O_3 crucible
3. Al_2O_3 protection cover of the thermocouple
4. Al_2O_3 crucible with drill-hole
5. Al_2O_3 protection cover of the induction coil
6. SiO_2 disc

7. Mo susceptor
8. Sample
9. 1st, 2nd und 3rd Ti-getter sheet
10. Thermocouple Type B (PtRh)
11. Ta wire
12. Al_2O_3 lid

Figure 1.11: Left: Inside of the furnace chamber with induction heating device. Right: Schematic cross section of the heating device. Note that the sample (8) was placed upon an Y_2O_3 crucible.

Before the heat treatment was accomplished the furnace chamber (see Figures 1.10 and 1.11) was evacuated to a high vacuum of 10^{-6} mbar and backfilled with Argon (purity 6.0) several times. This procedure yielded a residual oxygen content in the Argon atmosphere (700 mbar/at room temperature) of 0.4 ppm measured with a oxygen content measurement facility (oxygen/lambda sensor of the Metrotec company; see Figure 1.10). However, since the furnace chamber has a volume of 20 litres, the amount of oxygen is sufficient to contaminate the samples. For this reason three consecutive Ti-getter sheets were added to the experimental setup (no. 9 in Figure 1.11). The sample itself was placed on an Y_2O_3 pan because Al_2O_3 would react with the sample at elevated temperatures. The two-step homogenisation process requires an exact temperature control since, in particular, the temperature window of the bcc region (solid solution) extends only over 40 K (see Figure 1.8/melting point approx. 1683 K). However, it was not possible to measure the temperature directly beneath the sample since this would lead to a functionality loss of the Ti-getter sheets. For this reason a reference cell was built up in which the temperature was measured. The temperature measurement was done using a mineral-insulated Type B thermocouple (Pt 30 % Rh (+)/Pt 6 % Rh (-)) which allows temperature measurements up to 1970 K. The thermo-

couple was calibrated by melting high purity Si (melting point 1685 K). With this experimental setup it was possible to determine the temperature within 1 K.

1.6 Characterisation of TiCr$_2$ Laves-phase alloys

In Figure 1.12 the Ti-getter sheets, which were used for the described homogenisation procedure (cf. Section 1.5.2.1; in particular Figure 1.11), and also the homogenised samples are shown. The 1st Ti-getter sheet has been strongly contaminated, whereas the 2nd sheet experienced only minor contamination. The 3rd Ti getter and also the samples looked clean and shiny. Already these observations indicate that the Ti getter sheets efficiently protect the samples from contamination.
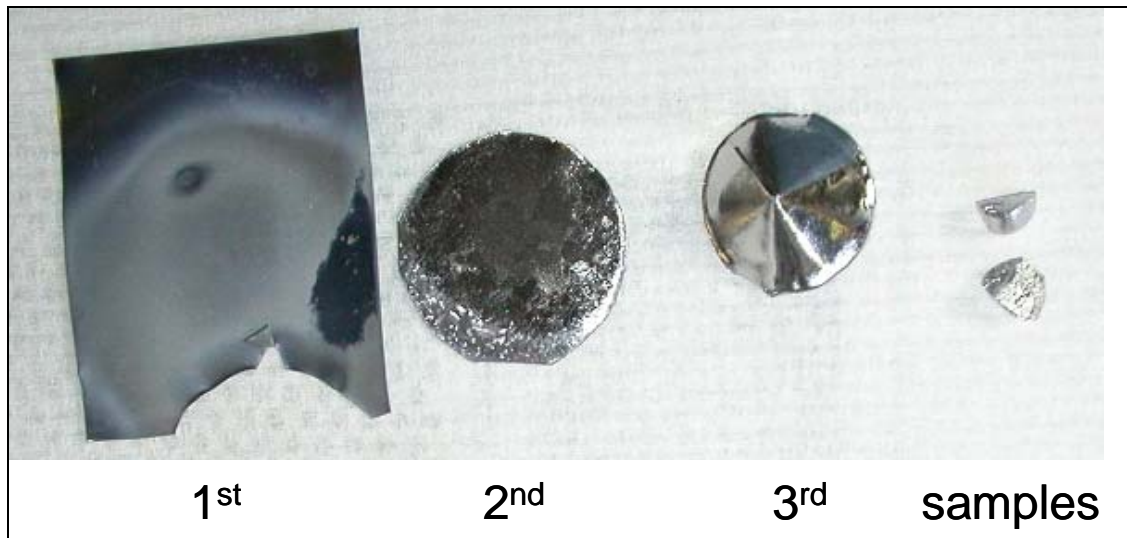
Figure 1.12: 1st, 2nd and 3rd Ti-getter sheet and TiCr$_2$ samples after the two-step homogenisation procedure.

The produced TiCr$_2$ alloy was characterised by chemical analysis, optical microscopy, scanning electron microscopy (SEM) energy/electron probe microanalysis (EDX/EPMA), X-ray powder diffractometry (XRPD), electron backscatter diffraction (EBSD) and high-resolution transmission-electron microscopy (HRTEM).

For the HRTEM and XRPD measurements powders were produced within a mortar; for the SEM, EDX, microprobe and EBSD analyses metallographic cross sections were prepared and manually grinded and polished.

1.6.1 Chemical analysis

Chemical analysis by carrier-gas hot extraction (ELTRA ONH 2000), combustion technology (ELTRA CS-800) and inductively coupled plasma optical emission (Spectro – CIROS CCD) showed that no uptake of metallic or non-metallic impurities during sample production and treatment took place.

Chemical analyses were made after the arc melting process and after the sample was homogenised. The sample was investigated for oxygen, nitrogen, carbon, aluminium (from Al_2O_3 crucible/see Figure 1.11) and molybdenum (from Mo susceptor/see Figure 1.11) impurities; the results are shown in Table 1.1. The values, which were marked with "<", indicate that the contents were below the detection limit; the detection limit is given by the ensuing number. The results of the chemical analyses showed that no detectable impurities get incorporated into the sample during the sample production process.

Table 1.1 Results of the chemical analysis in weight %.

sample condition	O	N	C	Al	Mo
as-cast	< 0.0005	< 0.0005	0.0030 ± 0.0005	< 0.0040	-
after homogenisation	< 0.0005	< 0.0005	0.0036 ± 0.0005	< 0.0020	< 0.0010

1.6.2 Electron probe microanalysis - EPMA

All samples were analysed by electron probe microanalysis (EPMA) to determine the Laves phase composition and to ensure that there is no concentration gradient within the sample. The measuring points were spread on three measuring lines with a distance of 300 μm (compare Figure 1.13). For a selected sample the results are shown in Figure 1.14, demonstrating that there is no macroscopic concentration gradient within the sample and that the average value lies within the standard deviation of the measuring points, i.e. the sample is homogeneous. All samples investigated in this work show no concentration gradient.
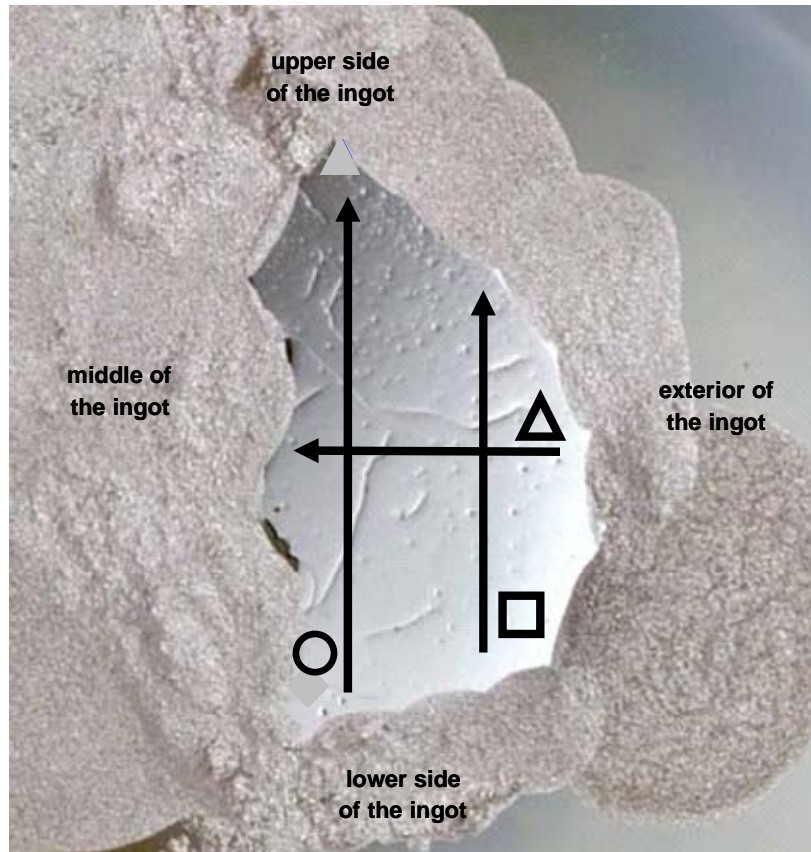
Figure 1.13: Schematic picture of a sample investigated by means of EPMA; the arrows and the symbols mark the measuring lines; compare Figure 1.14.
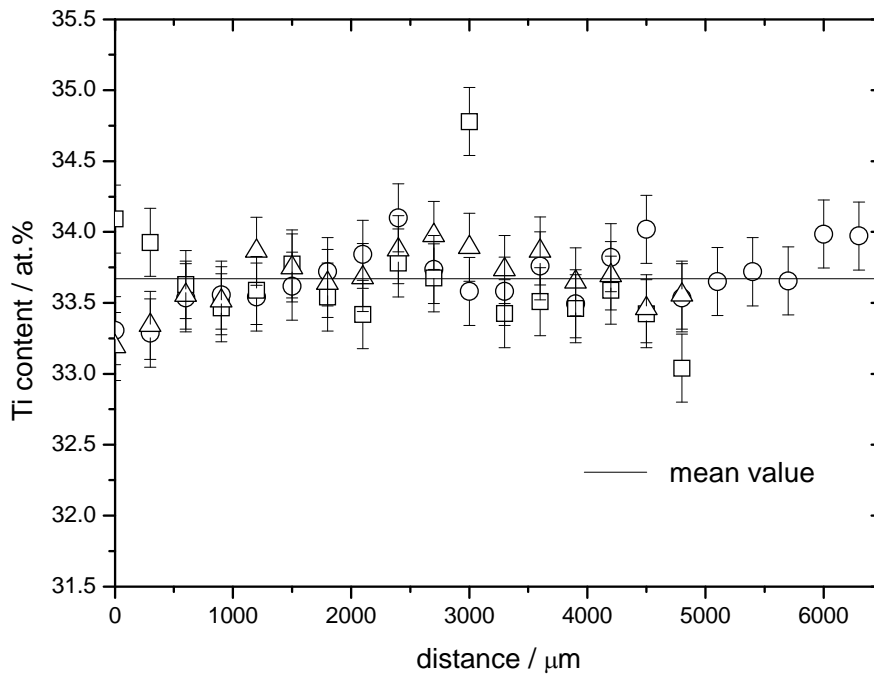
Figure 1.14: Ti content in dependence of the sample location. The different symbols indicate the different measurement lines; compare Figure 1.13. The error bars indicate the standard deviation.

1.6.3 X-ray powder diffractometry - XRPD

The X-ray powder diffraction measurements on the $TiCr_2$ powder samples were performed using a "Philips X`Pert MPD" diffractometer equipped with a germanium-monochromator, using Cu-$K_{\alpha1}$ radiation.

The phase analysis and the determination of the lattice parameters were performed using the software TOPAS [45]. In Figure 1.15a, for example, the powder diffraction pattern of an as-cast sample is shown, indicating that the present samples in the as-cast condition contain the hexagonal high temperature Laves phases, i.e. C14 and C36. This means the as-cast samples are (chemically) inhomogeneous.
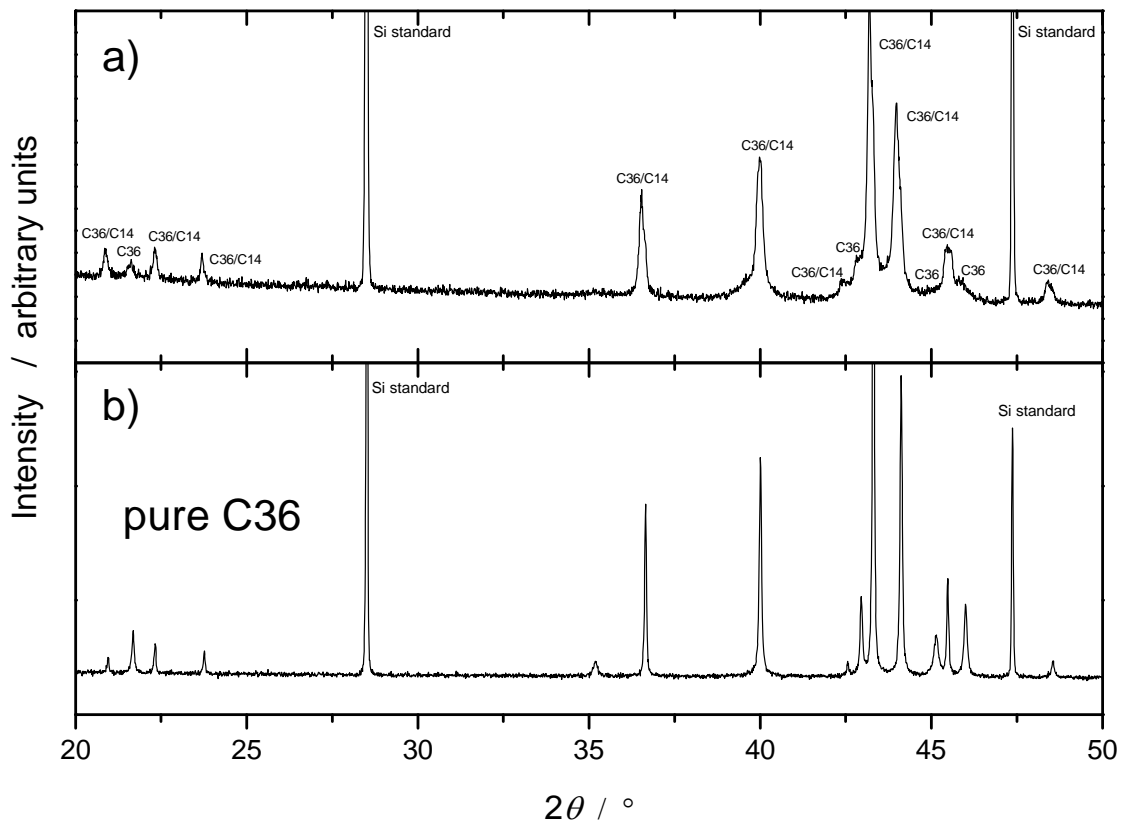
Figure 1.15: a) Powder diffraction pattern of an as-cast sample. b) Powder diffraction pattern of a homogenised sample (i.e. after the two step heat-treatment).

The XRPD pattern in Figure 1.15b shows that after the two step heat-treatment the sample contains the pure C36 high temperature Laves phase, i.e. the C36 phase is metastably retained at room temperature. The facts that the as cast sample consist of the high temperature phases C36/C14 and that the C36 phase was metastably retained at room temperature are in agreement with literature [8, 46, 47].

1.7 Focus of the thesis

The thesis concentrates on providing understanding of the mechanism of phase transformations in Laves phases and to develop a model based on the modular transformation model which describes the kinetics of the phase transformations in Laves phases. The understanding of the kinetics of the phase transformation allows a systematic control of the microstructure and thus of material properties.

As model system for the investigation of the phase transformations in Laves phases the binary Ti-Cr system was chosen. In this system it is possible to investigate all common temperature-dependent phase transformations occurring in Laves phases. This thesis focuses on the reversible, equilibrium $C36 \rightleftarrows C14$ phase transformation in $TiCr_2$ Laves phases. This phase transformation is fast enough to trace the progress of the phase transformation in-situ as a function of time/temperature in adequate time spans. Furthermore this phase transformation does occur at a moderate temperature for temperature-dependent Laves phase transformations (approx. 1550 K). Moreover, the $C36 \rightleftarrows C14$ first-order phase transformation takes place upon heating and cooling and thus the forward $C36 \rightarrow C14$ transformation and the backward $C36 \rightarrow C14$ transformation could be investigated.

1.8 Methodology and evaluation strategies

In order to trace the progress of the phase transformations as a function of different heating-/cooling rates, differential thermal analysis (DTA) was performed. The method allows a determination of the heats of reaction/transformation.

For phase identification and for the determination of features like lattice parameters, microstrain and for quantitative analysis of stacking faults within the sample X-ray powder diffraction experiments (XRPD) were performed. The XRPD results on stacking fault analysis were complemented/confirmed by high resolution transmission electron microscopy (HRTEM).

Combined application of the above mentioned methods allows the development of a model which gives a complete quantitative description of the kinetics of the phase transformation.

To describe the phase transformation quantitatively, i.e. to extract kinetic parameters, a model description was developed based on *the modular approach* [48]. The modular approach describes the course of a phase transformation by three overlapping

mechanisms (nucleation, growth and impingement), where each of this sub steps can be modelled separately. For a detailed model description the reader is referred to Section 5.2 and Ref. [48].

1.9 Outline of the thesis

The thesis is divided into three parts: The first part deals with experimental progress in the field of differential thermal analysis DTA (see Chapter 2). This progress was necessary to enable the quantitative investigation of the $C36 \rightleftarrows C14$ phase transformation in $TiCr_2$ Laves phases. For quantitative analysis of reaction/transformation kinetics using DTA a calibration of the DTA apparatus in terms of temperature and heat capacity is inevitable. Moreover the measurement signal has to be desmeared, since the measurement signal is smeared due to thermal lag [49], which affects the peak position and the peak shape.

In the second part layer-stacking irregularities in C36-type Nb-Cr and Ti-Cr Laves were systematically studied by XRPD and HRTEM. The layer-stacking irregularities in both substances can be associated with a preceding $C14$ (2H)$\rightarrow$C36 (4H) phase transformation driven by synchro-Shockley dislocations dipoles, i.e. the synchro-Shockley dislocations dipoles leave behind a fingerprint in terms of certain layer stacking irregularities (see Chapter 3).

The third part of this thesis is about phase transformation kinetics (Chapter 4, 5 and 6). During the investigation of the equilibrium $C36 \rightleftarrows C14$ phase transformation in $TiCr_2$ occurring in the vicinity of the equilibrium phase-transformation temperature T_0, it was found that application of the so-called Kissinger method [50] in the case of such an equilibrium transformation will lead to erroneous activation energies, since the original assumptions made for derivation of the Kissinger method are not valid. This was shown by theory and experiment in Chapter 4.

Chapter 5 deals with the phase-transformation kinetics of the equilibrium $C36 \rightleftarrows C14$ phase transformations in $TiCr_2$ Laves phases, i.e. the modular phase-transformation model has been successfully applied to DTA data of both transformations (i.e. for the phase transformation occurring upon heating and upon cooling). The model reveals the mechanism and the kinetics of the phase transformations and furthermore explains the differences of the phase transformations as a function of Laves-phase composition.

The modular model presented in Chapter 5 was used in Chapter 6 to describe the influence of the plastic deformation on the phase-transformation kinetics in $TiCr_2$ Laves phases. It is shown that plastic deformation considerably affects the phase-transformation kinetics. This is ascribed to the presence of dislocations formed upon plastic deformation during pressing.

1.10 References

[1]   W.B. Pearson, The crystal chemistry and physics of metals and alloys, New York: Wiley, 1972.

[2]   J. Hafner, The structures of binary compounds. Amsterdam: Elsevier, 1989.

[3]   E.I. Gladyshevskii, O. Bodak, Intermetallic Compounds, Vol. 1, Principles, Chichester: Wiley, 1995, p.403.

[4]   P. Villars, Intermetallic Compounds, Vol. 1, Principles, Chichester: Wiley, 1995, p.227.

[5]   F. Stein, M. Palm, G. Sauthoff, Structure and stability of Laves phases. Part I. Critical assessment of factors controlling Laves phase stability, Intermetallics 12 (2004) 713.

[6]   G. Sauthoff, Intermetallics, Weinheim: VCH, 1995.

[7]   M.L. Kronberg, Plastic deformation of single crystals of sapphire: Basal slip and twinning, Acta Metall. 5 (1957) 507.

[8]   C.W. Allen, P. Delavignette, S. Amelinckx, Electron microscopic studies of the Laves phases $TiCr_2$ and $TiCo_2$, Phys. Status Solidi A 9 (1972) 237.

[9]   M.F. Chisholm, K.S. Kumar, P.M. Hazzledine, Dislocations in complex materials, Science 307 (2005) 701.

[10]   J.H. Zhu, C.T. Liu, L.M. Pike, P.K. Liaw, Enthalpies of formation of binary Laves phases, Intermetallics 10 (2002) 579.

[11]   J.H. Zhu, C.T. Liu, L.M. Pike, P.K. Liaw, A thermodynamic interpretation of the size-ratio limits for laves phase formation, Metall. Mater. Trans. A 30 (1999) 1449.

[12]   J.H. Zhu, P.K. Liaw, C.T. Liu. Proc. 13th Annual Conference on Fossil Energy Materials. Knoxville, 1999, p.4.7.1.

[13]   Y. Kubota, M. Takata, M. Sakata, T. Ohba, K. Kifune, T. Tadaki, A charge density study of the intermetallic compound $MgCu_2$ by the maximum entropy method, J. Phys.-Condens. Mat. 12 (2000) 1253.

[14]   Y. Kubota, M. Takata, M. Sakata, T. Ohba, K. Kifune, T. Tadaki, A charge density study of $MgCu_2$ and $MgZn_2$ by the maximum entropy method, Jpn. J. Appl. Phys. Part 1, 38 (1999) 456.

[15]   F. Laves, H. Witte, Die Kristallstruktur des $MgNi_2$ und seine Beziehungen zu den Typen des $MgCu_2$ und $MgZn_2$, Metallwirtschaft 14 (1936) 645.

[16]   F. Laves, Cristallography of alloy, Naturwissenschaften 27 (1939) 65.

[17]   G.E.R. Schulze, Zur Kristallchemie der intermetallischen AB_2-Verbindungen (Laves-Phasen), Z. Elektrochem. 45 (1939) 849.

[18]   F. Laves, Theory of alloy phases, Cleveland: ASM, 1956, p.124.

[19]   G. Leitner, G.E.R. Schulze, Crystal chemical stability conditions for intermetallic compounds. I. Frequency distributions of Laves-phases, Krist. Tech. 6 (1971) 449.

[20]   C.H. Li, J.L. Hoe, P. Wu, Empirical correlation between melting temperature and cohesive energy of binary Laves phases, J. Phys. Chem. Solids 64 (2003) 201.

[21]   A.E. Dwight, Factors controlling the occurrence of Laves phases and AB_5 compounds among transition elements, T. Am. Soc. Metal. 53 (1961) 479.

[22]   F. Laves, Vergleich von Volumen- und Abstandskontraktionen in metallischen Verbindungen, Metall-Wirtschaft, -Wissenschaft, -Technik 15 (1936) 631.

[23]   F. Laves, Twenty five years laue diagram. With a composition of todays information on atom spacing in crystals, Naturwissenschaften 25 (1937) 721.

[24]   U. Dehlinger, G.E.R. Schulze, Crystal chemistry of the compounds of type $MgCu_2$ and $MgZn_2$, Z. Kristallogr. 102 (1940) 377.

[25]   F. Laves, H. Witte, Der Einfluß von Valenzelektronen auf die Kristallstruktur ternärer Magnesiumlegierungen, Metall-Wirtschaft, -Wissenschaft, -Technik 15 (1936) 840.

[26]   F. Laves, Beziehungen zwischen Koordinationszahlen und Valenzelektronen in intermetallischen Verbindungen, Nachr. Ges. Wiss. Göttingen 30 (1932) 519.

[27]   C.T. Liu, J.H. Zhu, M.P. Brady, C.G. McKamey, L.M. Pike, Physical metallurgy and mechanical properties of transition-metal Laves phase alloys, Intermetallics 8 (2000) 1119.

[28]   J.H. Zhu, Liaw, P.K., Liu, C.T., Effect of electron concentration on the phase stability of $NbCr_2$-based Laves phase alloys, Mat. Sci. Eng. A 240 (1997) 260.

[29]   J.H. Zhu, C.T. Liu, P.K. Liaw, Phase stability and mechanical behavior of $NbCr_2$-based Laves phases, Intermetallics 7 (1999) 1011.

[30]   Y. Ohta, D.G. Pettifor, Size versus electronic factors in transition-metal Laves phase-stability, J. Phys.-Condens. Mat. 2 (1990) 8189.

[31]   P. Villars, K. Mathis, F. Hullinger. The structure of binary compounds, Amsterdam: Elsevier, 1989, p.1.

[32]   P. Villars, K. Brandenburg, M. Berndt, S. LeClair, A. Jackson, Y.H. Pao, B. Igelnik, M. Oxley, B. Bakshi, P. Chen, S. Iwata, Binary, ternary and quaternary compound former/nonformer prediction via Mendeleev number, J. Alloys Compd. 317 (2001) 26.

[33]   P. Villars, A 3-dimensional structural stability diagram for 998 binary AB intermetallic compounds, J. Less-Common Met. 92 (1983) 215.

[34]   P. Villars, A 3-dimensional structural stability diagram for 1011 binary AB_2 intermetallic compounds 2, J. Less-Common Met. 99 (1984) 33.

[35]   P. Villars, 3-dimensional structural stability diagrams for 648 binary AB_3 and 389 binary A_3B_5 intermetallic compounds 3, J. Less-Common Met. 102 (1984) 199.

[36]   D.G. Pettifor, Structure maps for pseudobinary and ternary phases, Mater. Sci. Technol. 4 (1988) 675.

[37]   D.G. Pettifor. Intermetallic Compounds, Vol. 1, Principles, Chichester: Wiley, 1995. p.419.

[38]   A. Von Keitz, G. Sauthoff, P. Neumann, Laves phases for high temperatures - structure, stability and constitution, Z. Metallkd. 89 (1998) 803.

[39]   D.G. Pettifor, Physical metallurgy, The Netherlands: North-Holland, 1983. p.73.

[40]   D.G. Pettifor, The structures of binary compounds 1. Phenomenological structure maps, J. Phys. C Solid State 19 (1986) 285.

[41]   F. Stein, M. Palm, G. Sauthoff, Structure and stability of Laves phases part II - structure type variations in binary and ternary systems, Intermetallics 13 (2005) 1056.

[42]   D.T. Peterson, P.F. Diljak, C.L. Vold, The structure of thorium-magnesium intermetallic compounds, Acta Crystallogr. 9 (1956) 1036.

[43]   F.J. Smith, O.N. Carlson, D.T. Peterson, T.E. Scott, Thorium: preparation and properties, Iowa: Iowa State University Press, 1975, p.303.

[44]   J.L. Murray, Phase diagrams of binary titanium alloys, Ohio: ASM, 1987.

[45]   Topas, General profile and structure analysis software for powder diffraction data, Version 3. Bruker AXS GmbH, Karlsruhe, 2003.

[46]   K.S. Kumar, L. Pang, C.T. Liu, J. Horton, E.A. Kenik, Structural stability of the Laves phase Cr_2Ta in a two-phase $Cr-Cr_2Ta$ alloy, Acta Metall. Mater. 48 (2000) 911.

[47]   K.S. Kumar, L. Pang, J.A. Horton, C.T. Liu, Structure and composition of Laves phases in binary Cr-Nb, Cr-Zr and ternary Cr-(Nb, Zr) alloys, Intermetallics 11 (2003) 677.

[48]   F. Liu, F. Sommer, C. Bos, E.J. Mittemeijer, Analysis of solid state phase transformation kinetics: models and recipes, Int. Mater. Rev. 52 (2007) 193.

[49]   A.T.W. Kempen, F. Sommer, E.J. Mittemeijer, Calibration and desmearing of a differential thermal analysis measurement signal upon heating and cooling, Thermochim. Acta 383 (2002) 21.

[50]   H.E. Kissinger, Reaction Kinetics in Differential Thermal Analysis, Anal. Chem. 29 (1957) 1702.

Chapter 2

Calibration and desmearing of a differential thermal analysis measurement signal - upon heating and cooling - in the high-temperature region

Wolfgang Baumann, Andreas Leineweber and Eric Jan Mittemeijer

Abstract

A previously reported calibration and desmearing method for a differential thermal analysis (DTA) apparatus applicable to heating and cooling was successfully modified to be used in the high-temperature region (up to 1570 K). The method requires knowledge of parameters, which have a physical meaning, of the heat-flux model appropriate for the DTA apparatus. Values for these physical parameters were determined by calibration. As calibration materials Mo (exhibiting a smooth variation of specific heat with temperature) and Co (non-monotonic change of specific heat upon the ferro- to paramagnetic transition and vice versa) were employed. Experimental measures to improve the reproducibility were presented.

2.1 Introduction

Differential thermal analyses (DTA) are often used to determine heats of reaction/transformation, and to investigate reaction/transformation kinetics quantitatively as function of the heating/cooling rate [1, 2]. To this end the DTA facility used first has to be calibrated with respect to the values of the heat capacity and the temperature. Moreover, and in particular for the analysis of reaction/transformation kinetics, the measurement signal has to be desmeared, since the measurement signal is smeared due to thermal lag [3], which affects the peak position and the peak shape.

Usually the heat-capacity calibration of isochronal (i.e. applying a constant heating/cooling rate) DTA is performed by calculating the apparent molar heat capacity of a sample, as follows. The temperature difference of a piece of calibration material with a well-known heat capacity and a reference cell is measured and it is assumed that this temperature difference is proportional to the heat capacity of the calibration specimen. In this method the smearing of the measurement signal over time is neglected [3]; because of this the determined heat capacity is an "apparent" heat capacity. The effect of smearing plays a significant role when the heat capacity changes drastically with temperature as for example around the Curie temperature.

Common practice for the temperature calibration upon heating involves the melting of pure materials [4-6]. The determined melting temperatures are equated to the literature values and thereby temperature calibration has been performed. Note that temperature calibration has to be performed for each heating rate [7].

A standard technique to desmear a DTA measurement signal is to use a temperature filter with parameters which have no physical meaning [8-10]. Desmearing procedures which consider the mode of operation and the experimental setup of the apparatus are typically very complex and in addition they are only suitable for isochronal *heating* modes [3, 11].

The present work is based on previous work by Kempen *et al.* [3], where a combined temperature and heat-capacity calibration and desmearing method was developed for DTA. The method is applicable to heating and cooling experiments. It is based on a heat-flux model of the DTA with parameters which are independent of the heating/cooling rate applied. This model was previously applied successfully up to maximally 1100 K [3] by employing, in particular, the ferro- to paramagnetic transition of iron for the determination of the model parameters. A ferro- to paramagnetic transition, occurring at the Curie temperature, T_C, is suitable for the combined calibra-

tion and desmearing method, because such a transition is non-monotonic (i.e. the heat capacity goes to infinity at the Curie temperature) and consequently strongly smeared. In the present work the model was further developed for application to higher temperatures of up to 1570 K, by using the ferro- to paramagnetic transition of cobalt (T_C^{Co} = 1396 K) instead of that of iron (T_C^{Fe} = 1043 K). Thereby, the quantitative investigation of reaction/transformation kinetics and the quantitative determination of heats of reaction/transformation have become possible in the high temperature region.

2.2 Basis of the method

2.2.1 Heat flux model

A DTA apparatus measures the temperature difference between a sample and reference cell upon heating/cooling. The experimental setup of the sample measurement cell is shown in Figure 2.1. The sample and the reference cells are identical and are placed symmetrically with respect to each other in the furnace; the reference cell is empty (see Figures 2.1 and 2.2). From the furnace wall the heat is transported to the components of the sample measurement cell and the reference cell, and, depending on the heat capacities and the thermal resistances of the single components, heat transport also occurs between neighbouring components.

All components of the measurement cell are metallic (i.e. they have a small thermal resistance) except for the inner sample pan. The inner sample pan normally consists of inert, ceramic material (here Y_2O_3) to avoid chemical reactions between the outer sample pan (here Pt) and the sample at elevated temperatures.

The heat-transport characteristics of the sample measurement cell and the reference cell can be described using a heat-flux model of the DTA apparatus which consists of a limited number of heat resistances and heat capacities (cf. Figure 2.2 and Equations 2.1 – 2.4) [3].
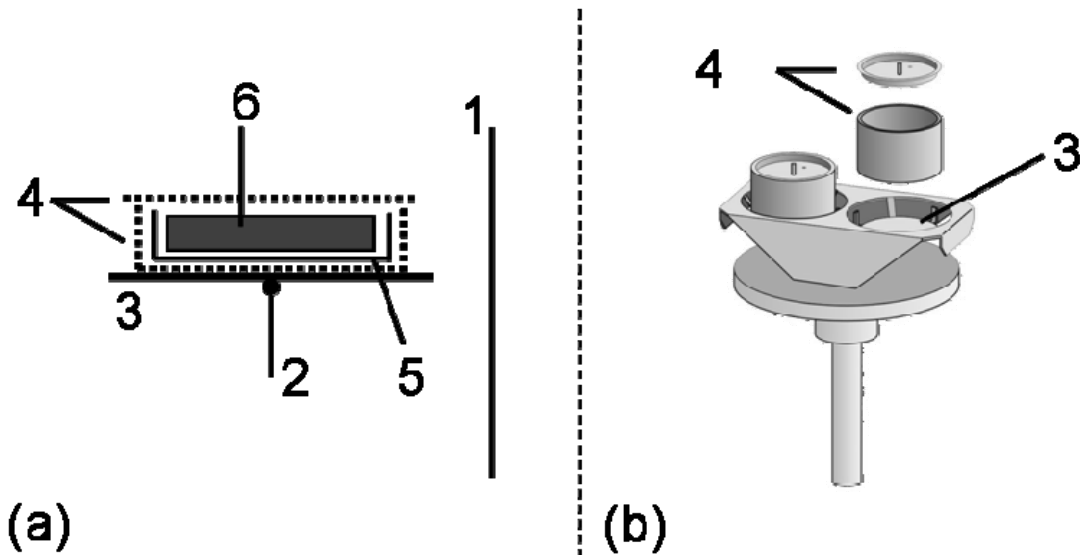
Figure 2.1: (a) Schematic illustration of the sample measurement cell and its components redrawn after [3]; (b) Schematic illustration of the measuring head [12]. (1) furnace; (2) thermocouple; (3) pan holder/ sample stage; (4) outer sample pan with lid; (5) inner sample pan; (6) sample.
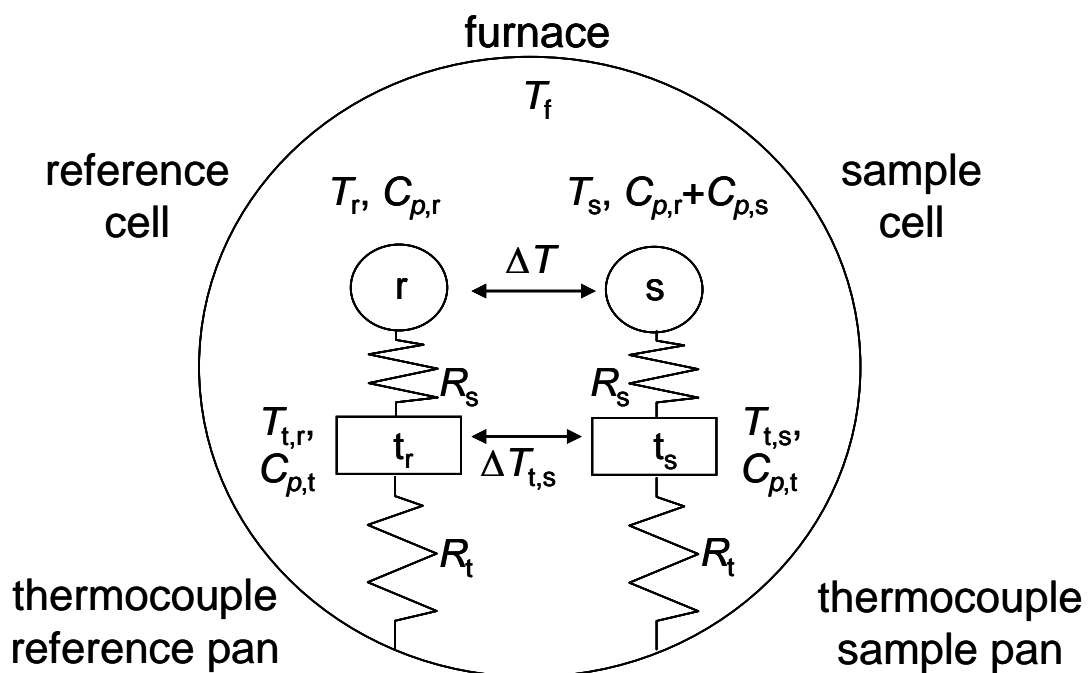
Figure 2.2: Schematic illustration of the heat-flux model of the DTA apparatus redrawn after [3]. The measured variables are the temperature of the thermocouple of the reference cell, $T_{t,r}$, and the temperature difference of the thermocouple of the reference cell and the sample cell, $\Delta T_{t,s}$, as function of time. The sample measurement and reference cells are connected to their thermocouples, t_s and t_r, via the thermal resistance, R_s. These thermocouples are connected to the furnace wall via the thermal resistance, R_t. The sample measurement cell is identical to the reference cell except for the presence of the sample.

The heat fluxes to the elements, t_r (thermocouple reference cell), r (reference cell), t_s (thermocouple sample cell) and s (sample measurement cell) (see Figure 2.2), can be described by the following equations [3]:

$$\frac{dq_{t,r}}{dt} = \frac{T_f - T_{t,r}}{R_t} - \frac{T_{t,r} - T_r}{R_s} = C_{p,t}\frac{dT_{t,r}}{dt}$$

(2.1)

$$\frac{dq_r}{dt} = \frac{T_{t,r} - T_r}{R_s} = C_{p,r}\frac{dT_r}{dt}$$

(2.2)

$$\frac{dq_{t,s}}{dt} = \frac{T_f - T_{t,s}}{R_t} - \frac{T_{t,s} - T_s}{R_s} = C_{p,t}\frac{dT_{t,s}}{dt}$$

(2.3)

$$\frac{dq_s}{dt} = \frac{T_{t,s} - T_s}{R_s} = \left(C_{p,s} + C_{p,r}\right)\frac{dT_s}{dt}$$

(2.4)

where T_f denotes the temperature of the furnace wall. T_s and T_r are the temperatures of the sample cell, s, and the reference cell, r (Figure 2.2), respectively. $T_{t,s}$ and $T_{t,r}$ denote the temperatures of the thermocouples of the sample cell, t_s, and reference cell, t_r, respectively. $C_{p,s}$, $C_{p,r}$ and $C_{p,t}$ are the heat capacities of the sample, of the reference cell and of the thermocouple and its direct surroundings; t is the time. The measured variables are the temperature of the thermocouple of the reference cell, $T_{t,r}$, and the temperature difference of the thermocouples of the reference cell and the sample cell: $\Delta T_{t,s}$ = $T_{t,s}$ - $T_{t,r}$. The identical thermocouples t_r and t_s are not calibrated for absolute temperature determination. Hence, a temperature deviation of the thermocouple t_r, ΔT_{tc}, which is taken temperature and heating rate independent, has to be incorporated in the analysis.

The DTA facility can thus be described by five heating-rate and cooling-rate independent physical parameters: (i) the heat resistance, R_t, between the furnace and the thermocouples; (ii) the heat capacity of the thermocouple and its direct surroundings, $C_{p,t}$; (iii) the heat capacity of the reference cell, $C_{p,r}$; (iv) the heat resistance between sample measurement/reference cell and thermocouple, R_s, and (v) the thermocouple temperature shift, ΔT_{tc}.

According to Kempen et al. [3] these five DTA parameters can be determined by measuring two calibration materials with known C_p: One material (a) should exhibit a heat capacity that varies smoothly with temperature, the other one (b) should show a strong, preferably non-monotonic, temperature dependence of the heat capacity. In

Ref. [3] for (a) sapphire and for (b) iron with its ferro- to paramagnetic transition at $T_C^{Fe} = 1043$ K were used.

On the basis of the DTA data recorded from the calibration materials for various heating/cooling rates, the above mentioned physical parameters describing the DTA apparatus can be determined. In order to extend the applicability of the method to high temperatures, in the present work molybdenum and cobalt were used as calibration materials (a) and (b), respectively. Cobalt has its ferro- to paramagnetic transition at $T_C^{Co} = 1396$ K, which is about 353 K higher than the Curie temperature of iron T_C^{Fe}. The ferro- to paramagnetic transitions of iron and cobalt show no temperature hysteresis [13, 14] (no mass transport involved), so that the Curie temperature is heating- and cooling-rate independent [15].

The determination of the instrumental DTA parameters was done on the basis of literature data for the temperature dependent molar heat capacity of molybdenum, $C_{p,Mo}$, (cf. Section 2.2.2) and for the Curie temperature of Co (cf. Section 2.2.3) as follows (for details of the fit procedure, see Ref. [3]). Using literature data for $C_{p,Mo}$ as well as the DTA data recorded from the Mo measurements, first the temperature dependent parameter R_t was calculated (for each heating and cooling rate). Next, applying Equations (2.3) and (2.4), the calculated (temperature dependent) parameter R_t (averaged over all heating/cooling rates) and the recorded DTA data from the Co measurements, the molar heat capacity of Co, $C_{p,Co}$, was calculated. This calculation of $C_{p,Co}$ is based on a complex fit procedure during which the fit parameters $C_{p,t}$, $C_{p,r}$ and R_s are varied according to a simplex procedure [16], such that the $C_{p,Co}$ curves for different heating/cooling rates coincide. Finally, ΔT_{tc} was calculated as the difference of the calculated value and the literature value of the Curie temperature of cobalt. The thus obtained model description of the DTA apparatus can be validated by comparing the desmeared molar heat capacity of cobalt, $C_{p,Co}$, as function of temperature with literature data (cf. Section 2.2.3).

2.2.2 C_p of molybdenum

Molybdenum has a molar heat capacity that changes smoothly, monotonically with temperature. Temperature dependent values for the molar heat capacity of molybdenum $C_{p,\text{Mo}}$ were adopted as given in Ref. [17]. The uncertainties in the heat-capacity values were estimated not to exceed ± 1.0 percent. The discrete values for $C_{p,\text{Mo}}$ from Ref. [17] can be described by a continuous fifth-order polynomial. The difference between the data points and the polynomial curve does not exceed ± 0.1 percent and consequently can be neglected. It thus was obtained:

$$C_{p,\text{Mo}} = A_0 + A_1 T + A_2 T^2 + A_3 T^3 + A_4 T^4 + A_5 T^5 \quad \text{for } 273.15\ \text{K} \leq T \leq 1750\ \text{K} \qquad (2.5)$$

with A_0 = 17.1694 Jmol-1K-1, A1 = 0.03515×Jmol-1K-2, A2 = -5.35826×10-5 Jmol-1K-3, A3 = 4.40757×10-8 Jmol^{-1}K^{-4}, A_4 = -1.70917×10^{-11} Jmol^{-1}K^{-5} and A_5 = 2.64523×10^{-15} Jmol^{-1}K^{-6}.

2.2.3 C_p of cobalt

A number of publications provide data for the molar heat capacity of Co, $C_{p,\text{Co}}$, and the Curie temperature of cobalt, T_C^{Co} [18-25]. The data for $C_{p,\text{Co}}$ adopted in this work correspond to those taken up in the SGTE database [18] and to those given by Guillermet [19] who made a critical evaluation of data for the thermodynamic properties of cobalt (cf. Section 2.4).

2.3 Experimental

As DTA apparatus a DSC 404C Pegasus from Netzsch (the same DTA as used in Ref. [3]) has been employed. The apparatus is equipped with a DSC C_p sensor (thermocouple type S) and a high temperature noble-metal furnace. The measurements were performed under a dynamic argon atmosphere (99.9999 %; flow rate 50 ml/min).

2.3.1 Improvement of the reproducibility of the DTA signal

First, a series of test measurements was conducted using the conventional experimental setup shown in Figure 2.1 (right). Here it is necessary to lift up both Pt pans from the sample stage after each measurement to avoid diffusion bonding with the sample stage (see Figure 2.1). This lift up and the following putting down influences the reproducibility of the measurements, since the (thermal) contact between the sample stage and the Pt pans is changed and because the Pt pans cannot be placed exactly at the same position as before (see Figure 2.3).
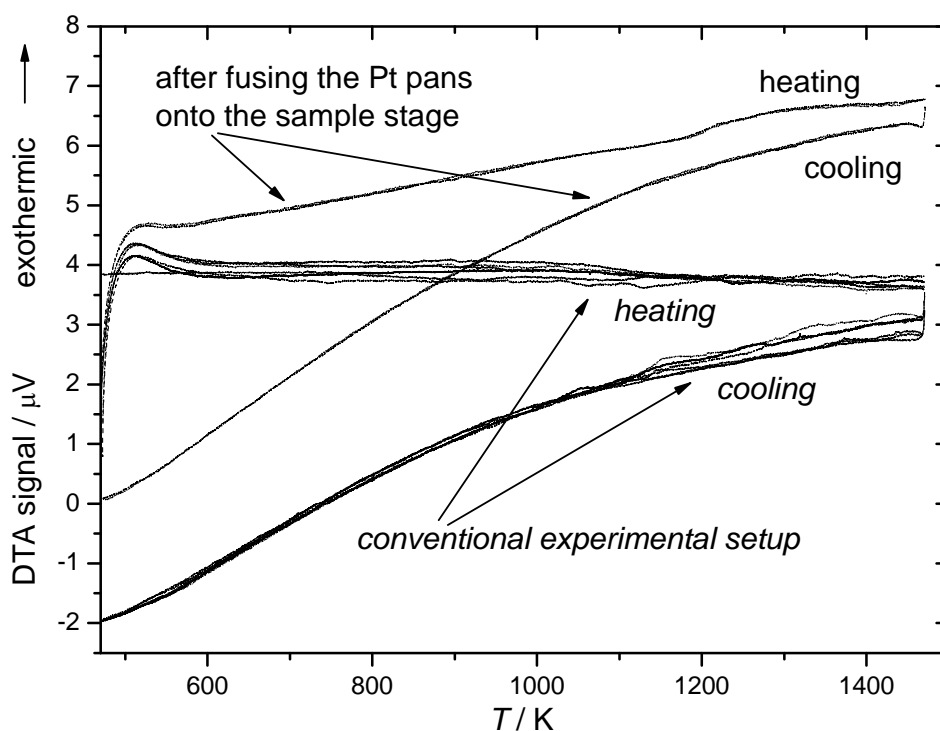
Figure 2.3: Consecutive runs with empty sample measurement cell, recorded (i) with the conventional experimental setup (6 runs) and (ii) after the Pt pans had been fused onto the sample stage (2 runs); heating/cooling rate 10 K/min.

Therefore the Pt pans were diffusion bonded on the sample stage so that position and contact area do not change in a series of consecutive measurements. Thus, only a transfer of the inner sample pan is necessary for the exchange of samples in a series of measurements (see Figure 2.1).

The fusing of the Pt pans with the sample stage was performed after placing the Pt pans exactly in the middle of the sample stage. Afterwards consecutive calibration DTA runs were performed with heating up to 1720 K; the calibration runs were repeated until the subsequent runs showed no deviations from the previous runs.

The improvement of the reproducibility of the measurements by diffusion bonding of the Pt pans is obvious from the results shown in Figure 2.3. Without this modification of the measurement setup (i.e. the fusing of the Pt pans) the required reproducibility of the measurements for the calibration and desmearing procedure in the high-temperature region would not have been achieved.

2.3.2 DTA runs

For the DTA measurements disc shaped Co (purity 99.998 %) and Mo (purity 99.95 %) samples with a diameter of approx. 5 mm and a thickness of about 1.4 mm were cut from rods of the respective pure metals. Subsequently the samples were ground and polished to clean the surface of the metal samples. For the last polishing step a 3 μm diamond paste was used.

Three subsequent runs were performed for each heating/cooling rate applied (here: 10, 15 and 20 K/min):

- empty measurement
- cobalt sample
- molybdenum sample

For every heating/cooling rate a new cobalt or molybdenum sample was used. During the measurement the samples were unavoidably slightly oxidised at the surface. To ensure that this oxidation does not affect the DTA measurement signal, second runs were carried out for the cobalt and molybdenum measurements and the results were identical to the results of the first run.

If the sample cell and the reference cell would exhibit the truly same setup, the empty run should cause a zero signal; i.e. there should be no temperature difference between the sample measurement cell and the reference cell. However, in reality a small difference in the setups for sample measurement cell and reference cell occurs, and therefore the measurement signal of the empty run was subtracted from the corresponding signals of the Co and Mo measurement runs.

For the inner sample pan (cf. no.5 in Figure 2.1) Y_2O_3 was selected because this material shows no reaction with the calibration materials. At the bottom the Y_2O_3 pans had a thickness of about 0.2 mm. Note that for all measurements the same pans were used.

2.4 Results and discussion

The apparent molar heat capacity of cobalt, $C_{p,\mathrm{Co}}^{\mathrm{app.}}$, as function of temperature can be calculated (cf. second paragraph of Section 2.1) on the basis of the DTA measurement signal recorded for Co, $\Delta T_{\mathrm{t,Co}}$, using the DTA measurement signal recorded for Mo (calibration material), $\Delta T_{\mathrm{t,Mo}}$, and the known heat capacity of Mo, $C_{p,\mathrm{Mo}}$ (cf. Section 2.2): $C_{p,\mathrm{Co}}^{\mathrm{app.}} = C_{p,\mathrm{Mo}}\left(\Delta T_{\mathrm{t,Co}}/\Delta T_{\mathrm{t,Mo}}\right)$. Results are shown in Figure 2.4.
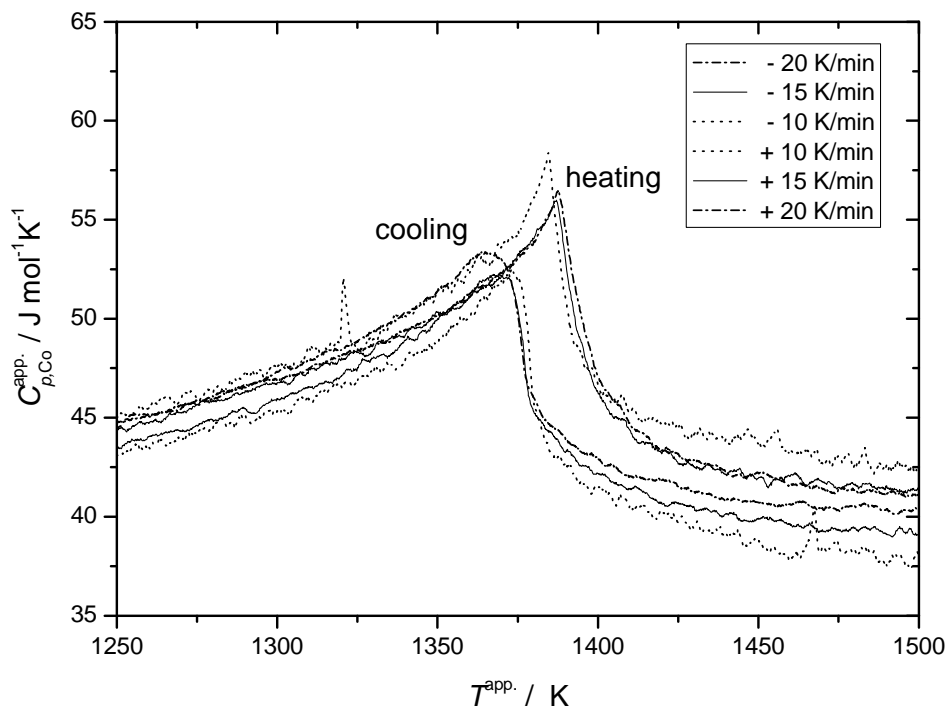
Figure 2.4: Apparent molar heat capacity of Co, $C_{p,\mathrm{Co}}^{\mathrm{app.}}$, for three different heating and cooling rates; calculated as described at the beginning of Section 2.4.

The true heat capacity is independent of heating and cooling rate. However, the apparent molar heat capacity of Co, determined as described above, strongly depends on the heating/cooling rate; also the ferro- to paramagnetic transition temperature shows a heating-/cooling-rate dependence (see Figure 2.4). These heating-rate and cooling-rate dependencies are caused by smearing due to thermal lag. The often used, simple calibration procedure, that provides the basis for the results shown in Figure 2.4, is inadequate.

Application of the present calibration and desmearing method based on the heat-flux model (Section 2.2.1) led to results for the molar heat capacity as function of temperature shown in Figure 2.5. Evidently, the desmearing procedure leads to coincidence of the curves pertaining to the different heating and cooling rates and thus an

apparent thermal hysteresis of the ferro- to paramagnetic transition does not occur, as it should be (see also Figure 2.6). The small remaining differences between the various molar heat capacity curves are within the experimental accuracy of the DTA measurements.
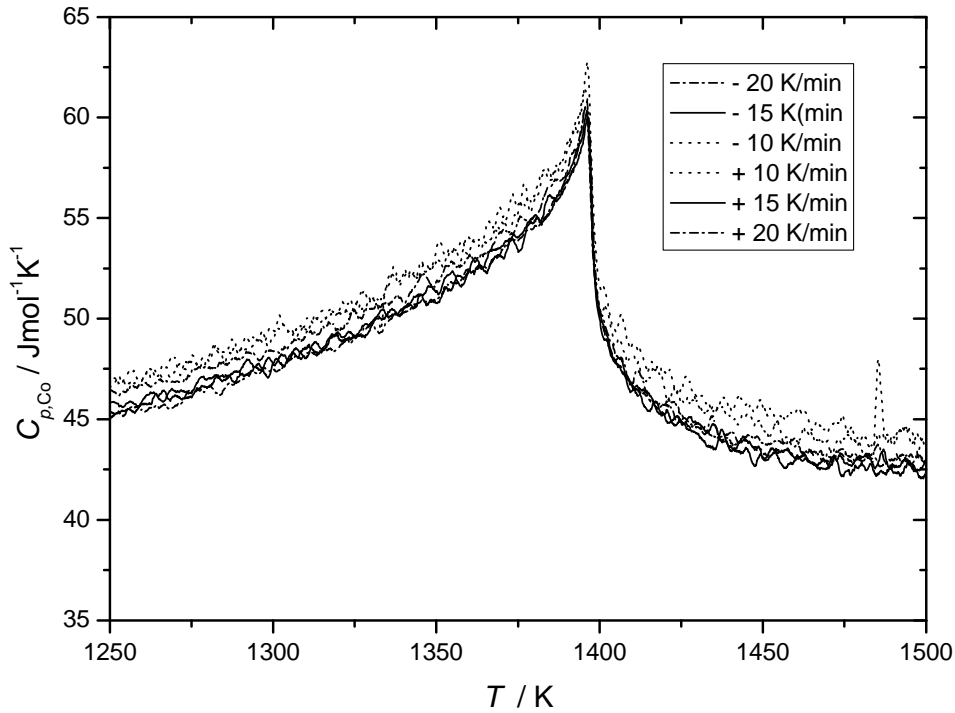
Figure 2.5: Molar heat capacity of Co, $C_{p,\mathrm{Co}}$, for different heating/cooling rates after correction for thermal smearing according to the heat flux model.

The average of the molar heat capacity curves of Co, $C_{p,\mathrm{Co}}$, (calculated from the plots in Figure 2.5) can be compared with corresponding literature data (cf. Section 2.2.3) in Figure 2.6. It follows that the molar heat capacity curve determined in this work agrees very well with the literature data.
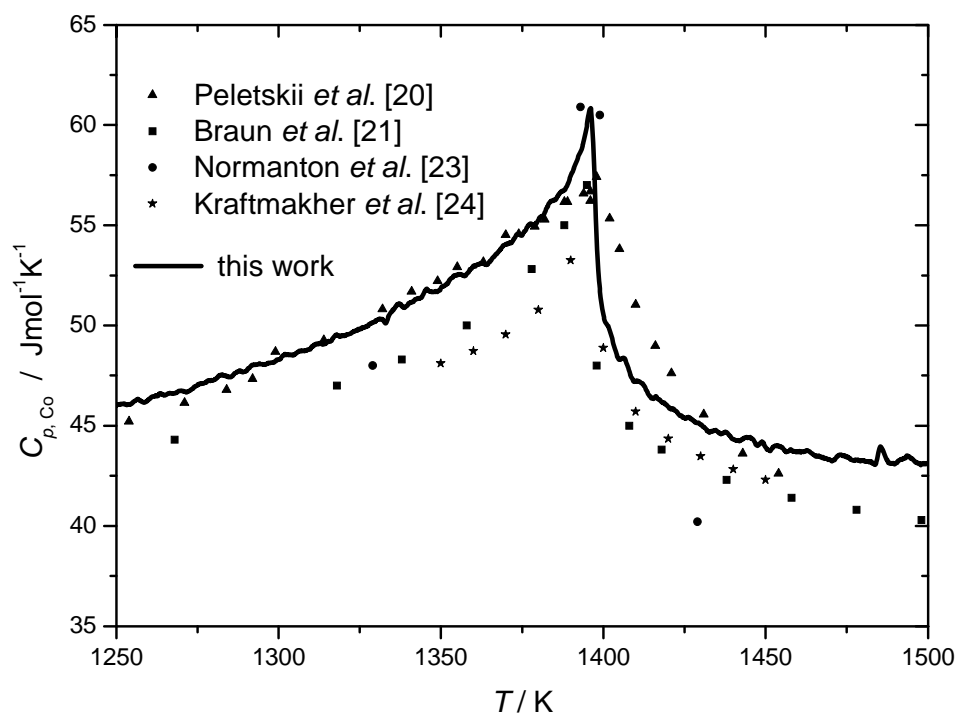
Figure 2.6: Molar heat capacity of Co, $C_{p,\text{Co}}$, (average calculated from the plots in Figure 2.5) in comparison with literature data [20, 21, 23, 24]. The literature data were shifted along the temperature axis such that the Curie temperatures coincide at T_{c}^{Co} = 1396 K [18, 19].

The values obtained for the instrumental DTA (fit) parameters $C_{p,\text{t}}$, $C_{p,\text{r}}$, R_{s} and ΔT_{tc} (as listed in Section 2.2.1 and determined as described immediately above) have been gathered in Table 2.1. The values determined for these physical parameters as determined by Kempen et al. [3], for the same DTA apparatus but using different calibration materials and pertaining to a different temperature range, have also been given in Table 2.1.

Table 2.1 Values for the instrumental DTA parameters as determined in this work in comparison with the values for these parameters determined in Ref. [3] for the same apparatus, but at a lower temperature range.

	T range / K	$C_{p,\text{t}}$ / JK^{-1}	$C_{p,\text{r}}$ / JK^{-1}	R_{s} / KsJ^{-1}	ΔT_{tc} / K
this work	1250 - 1570	0.0500	0.0429	38.4520	15.2
Kempen et al. [3]	930 - 1110	0.0676	0.0326	61.2359	7.1
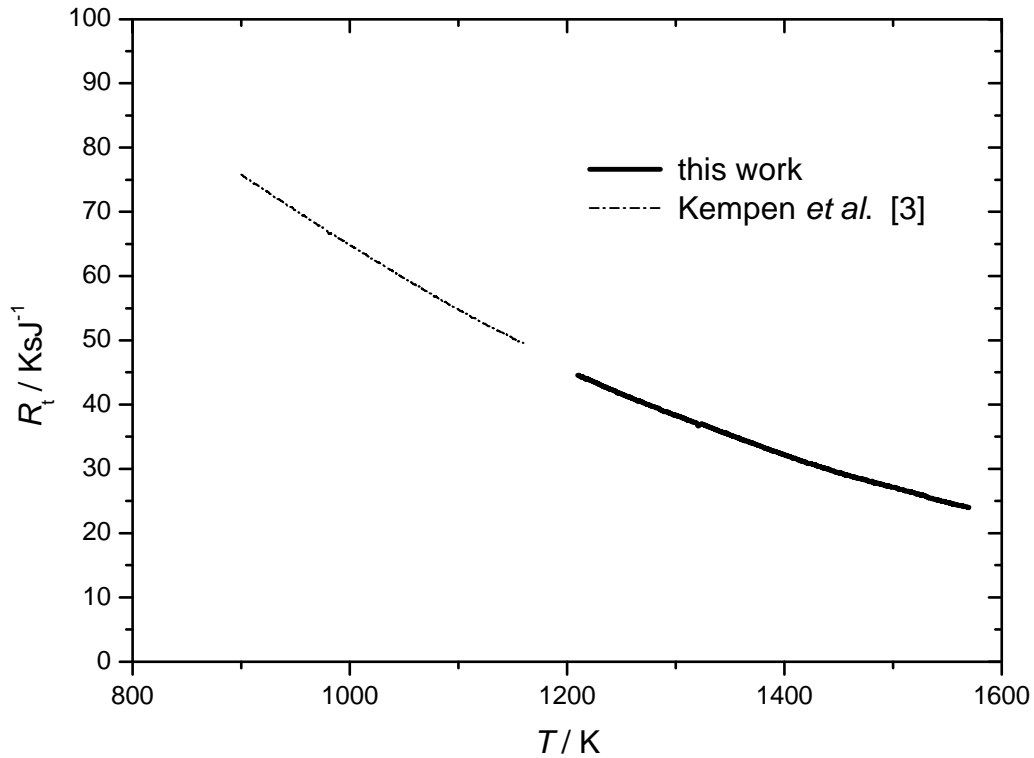
Figure 2.7: The heat resistance Rt between the furnace wall and the thermocouples as a function of temperature.

The values determined here for $C_{p,t}$ and $C_{p,r}$ are of the same order of magnitude as those determined in Ref. [3]. The value for the heat resistance R_s (between sample and thermocouple) is one third smaller than the value determined in Ref. [3]. This can be understood as a consequence of (i) the fusing of the Pt-pan on the sample stage in the current work (so the thermal contact gets better) and (ii) the increasing contribution of radiation to heat transport with increasing temperature.

The increasing contribution of radiation to heat transport with increasing temperature also explains the decrease of the heat resistance R_t (between the furnace wall and the thermocouples) with increasing temperature (see Figure 2.7). In particular, the dependence of R_t on temperature, for the temperature range investigated in Ref. [3] is, by extrapolation, very well compatible with the results obtained here at considerably higher temperatures.

2.5 Conclusions

- Calibration and desmearing of differential thermal analysis scans (temperature difference of sample and reference pans as function of temperature) - upon heating and cooling - is possible in the high temperature region (up to, at least, 1570 K).

- By fusing of the (Pt) sample and reference pans on the sample stage the reproducibility of the measurements is improved considerably. Without this modification of the measurement setup the required reproducibility for the calibration and desmearing procedure in the high-temperature region cannot be achieved.

- The heat flux model, originally derived in Ref. [3], can be applied in a temperature region much larger than in the original work, recognising temperature dependence of the instrumental DTA parameters. Thereby the physical basis of the (fit) parameters of the model is corroborated.

2.6 References

[1]   G. Höhne, W. Hemminger, H.-J. Flammersheim, Differential Scanning Calorimetry, Berlin: Springer-Verlag, 1996.

[2]   F. Liu, F. Sommer, C. Bos, E.J. Mittemeijer, Analysis of solid state phase transformation kinetics: models and recipes, Int. Mater. Rev. 52 (2007) 193.

[3]   A.T.W. Kempen, F. Sommer, E.J. Mittemeijer, Calibration and desmearing of a differential thermal analysis measurement signal upon heating and cooling, Thermochim. Acta 383 (2002) 21.

[4]   E. Gmelin, S.M. Sarge, Temperature, heat and heat flow rate calibration of differential scanning calorimeters, Thermochim. Acta 347 (2000) 9.

[5]   G.W.H. Hohne, H.K. Cammenga, W. Eysel, E. Gmelin, W. Hemminger, The temperature calibration of scanning calorimeters, Thermochim. Acta 160 (1990) 1.

[6]   H.K. Cammenga, W. Eysel, E. Gmelin, W. Hemminger, G.W.H. Hohne, S.M. Sarge, The temperature calibration of scanning calorimeters 2. Calibration substances, Thermochim. Acta 219 (1993) 333.

[7]   J.D. Menczel, Temperature calibration of heat flux DSC's on cooling, J. Therm. Anal. 49 (1997) 193.

[8]   H.J. Flammersheim, N. Eckardt, W. Kunze, The deconvolution of DSC-curves in the experimental time domain, Thermochim. Acta 187 (1991) 269.

[9]   S. Wiesner, E. Woldt, An algorithm for the reconstruction of the true specimen signal of a differential scanning calorimeter, Thermochim. Acta 187 (1991) 357.

[10]   G.P. Krielaart, S. van der Zwaag, Kinetics of gamma→alpha phase transformation in Fe-Mn alloys containing low manganese, Mater. Sci. Technol. 14 (1998) 10.

[11]   W. Poessnecker, Theoretical investigations of the heat transfer at quantitative DSC-measurements and its influence on the determination of the thermal and calorimetrical properties, Thermochim. Acta 187 (1991) 309.

[12]   Netzsch, Instrument Manual Netzsch DSC 404C Pegasus, 1998.

[13]   E. Kneller, Ferromagnetism, Berlin: Springer-Verlag, 1962.

[14]   R.M. Bozorth, Ferromagnetism, Toronto: D. van Nostrand Co., 1951.

[15]   Y.H. Jeong, D.J. Bae, T.W. Kwon, I.K. Moon, Dynamic specific-heat near the Curie-point of Gd, J. Appl. Phys. 70 (1991) 6166.

[16]   W.H. Press, S.A. Teukolsky, W.T. Vetterling, B.P. Flannery, Numerical recipes in C, New York: Cambridge University Press, 1997.

[17]   J.P. Cali, Molybdenum - Heat Capacity, NIST Database, Standard Reference Material 781, 1977.

[18]   A.T. Dinsdale, SGTE data for pure elements, Calphad 15 (1991) 317.

[19]   A.F. Guillermet, Critical evaluation of the thermodynamic properties of cobalt, Int. J. Thermophys. 8 (1987) 481.

[20]   V.E. Peletskii, E.B. Zaretskii, Investigation of the thermal transport properties and temperature anomalies near the Curie points of the classical ferromagnets cobalt and iron, High Temp. - High Press. 13 (1981) 661.

[21]   M. Braun, R. Kohlhaas, Die spezifische Wärme des Kobalts zwischen 50 und 1400 °C, Z. Naturforsch. A 19a (1964) 663.

[22]   M. Braun, R. Kohlhaas, Die spezifische Wärme von Eisen, Kobalt und Nickel im Bereich hoher Temperaturen, Phys. Status Solidi 12 (1965) 429.

[23]   A.S. Normanton, A calorimetric study of high-purity cobalt from 600 to 1600 K, Met. Sci. 9 (1975) 455.

[24]   Y.A. Kraftmakher, T.Y. Romashina, Heat capacity of cobalt in the vincinity of the Curie point, Sov. Phys.-Sol. State 8 (1966) 1562.

[25]   E.A. Owen, D. Madoc Jones, Effect of grain size on the crystal structure of cobalt, P. Phys. Soc. Lond. B 67 (1954) 456.

Chapter 3

Layer-stacking irregularities in C36-type Nb-Cr and Ti-Cr Laves phases and their relation with polytypic phase transformations

Jochen Aufrecht, Wolfgang Baumann, Andreas Leineweber, Viola Duppel

and Eric Jan Mittemeijer

Abstract

Specific layer-stacking irregularities have been identified in C36 (4H) Nb-Cr and Ti-Cr Laves-phases on the basis of X-ray diffraction line-profile analysis and high resolution transmission-electron microscopy. Domain boundaries and transformation errors within domains could be distinguished. The layer-stacking irregularities in both C36-$NbCr_2$ and C36-$TiCr_2$ can be associated with a preceding C14 (2H)$\rightarrow$C36 (4H) phase transformation carried out by glide of mobile synchro-Shockley partial dislocation dipoles in an ordered fashion. The stacking irregularities observed can be interpreted as deviations from such perfect "ordered glide". The interpretation is supported by the observation that in case of C36-$NbCo_2$, where no preceding C14$\rightarrow$C36 transformation occurs, different layer-stacking irregularities are observed.

3.1 Introduction

3.1.1 Laves phases; layer-stacking rules

In the last ten years the interest in Laves phases (general formula AB_2; A, B: metal atoms) has grown pronouncedly. From a practical point of view, Laves phases have been proposed as candidates for structural materials, but also for functional materials, like magnetic, superconducting materials and as hydrogen-storage materials [1]. From a scientific point of view, the Laves phases constitute the largest group of intermetallic phases occurring in a very large number of binary and ternary systems [2, 3], which makes it possible to study specific properties as function of the elemental constituents of the Laves phase. Such information allows tailoring the properties for specific applications.

Laves phases are characterised by their specific crystal structures, which are tetrahedrally close-packed structures and thus belong to the so-called Frank-Kasper phases [4, 5]. The different Laves-phase crystal-structure types can be conceived as polytypes generated by stacking several types of atomic layers subject to some particular stacking principles (Figure 3.1). These crystal structures imply that the atomic-radius ratio of the A and B atoms, r_A/r_B, equals $(3/2)^{1/2} \approx 1.225$, regarding the atoms as hard spheres.

Different descriptions of stacking rules leading to the Laves phases are available in the literature. For the current purposes it suffices to focus on the stacking of *layer-sandwich units*, each composed of a specific stack of three atomic layers, AB_3A (this notation refers to the composition of this stacking unit; called layer triplets in Ref. [6]; not identical with the triple layers considered in some other works [7, 8]). Between these layer-sandwich units additional *single-layer units,* B are located (see Figure 3.1). With respect to a given two-dimensional hexagonal unit mesh defined by the lattice-structure basis vectors **a** and **b** perpendicular to the stacking direction, the A atoms of the *layer-sandwich units* and the B atoms of the *single-layer units* can each assume three different relative positions, i.e. at fractional coordinates either (0, 0), or (1/3, 2/3) or (2/3, 1/3).[1] Representing the position of the layer-sandwich units by X, Y, and Z, and of the single-layer units by x, y, and z, depending on which of the former three positions is assumed by the layer concerned (i.e. (0, 0): X, x; (1/3, 2/3): Y, y; and

---

[1]Use of the symbols A, B, and C to indicate the relative layer positions is prevented to avoid confusion with the symbols A and B used for the two different metals constituting the Laves phase AB_2.

(2/3, 1/3): Z, z), the layer-stacking sequence of a Laves phase can be represented by an alternate sequence of these upper- and lower-case letters. The following rules apply additionally:

(i) Taking first only into account the upper-case letters, a given letter, say X, may only be followed by a different other upper-case letter, in this case Y or Z, i.e. an X cannot be followed by an X (Y not by Y; Z not by Z).

(ii) A *single-layer unit* located between two *layer-sandwich units* is represented by a lower-case letter different from the upper-case letters representing the adjacent *layer-sandwich units*. Consequently, a z-type single layer is located between X and Y, i.e. the corresponding part of the stacking sequence reads ...XzY... or ...YzX....
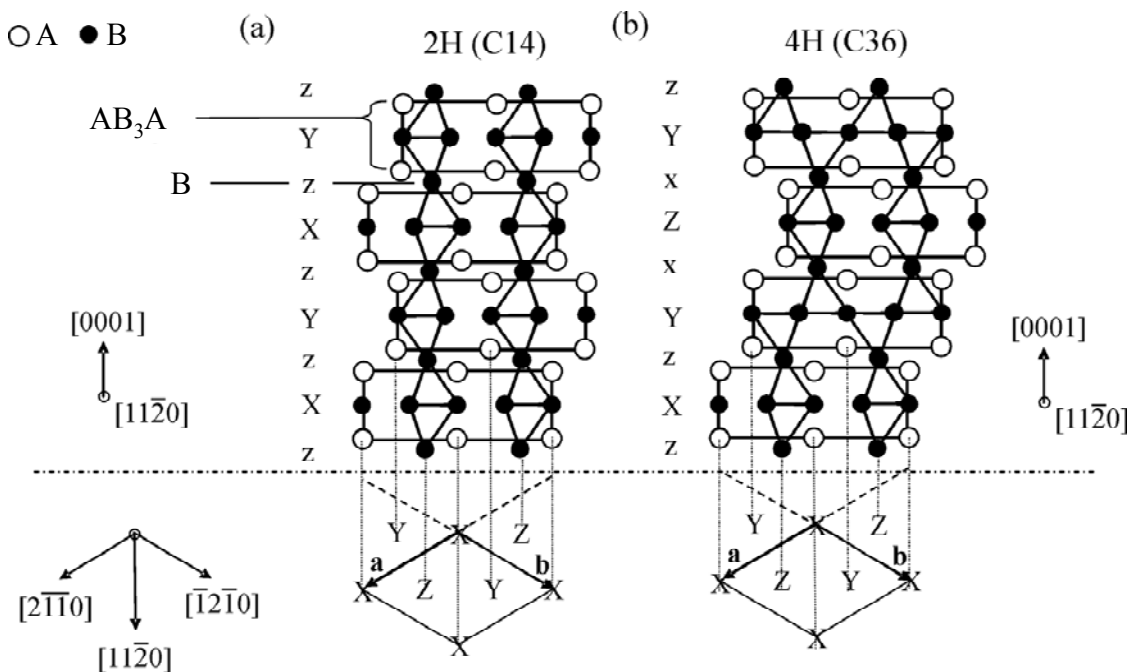
Figure 3.1: Schematic crystal structure of (a) C14 type Laves phase and (b) C36 type Laves phase, built up by alternate stacking of AB_3A *layer-sandwich units* and B *single-layer units*. In the upper part of the figure, the layer-stacking sequences have been displayed in a $\left[11\bar{2}0\right]$ projection, i.e. the $\left[11\bar{2}0\right]$ direction is perpendicular to the plane of drawing. In the lower part of the figure, the stacking positions have been indicated in $\left[0001\right]$ projection. The basis vectors **a** and **b**, perpendicular to the stacking [0001] direction, span a two-dimensional hexagonal unit mesh.

Since the positions of the single layer units are unambiguously prescribed by the positions of the adjacent layer-sandwich units (see above), it is sufficient for most purposes to consider only the upper-case letters to indicate the stacking sequence, as done at most places in the present paper. In terms of only the X, Y, and Z symbols describing the stacking sequences following the rules given above, the possible polytypes of Laves phases constitute one-to-one analogues of the polytypes possible for closed-

packed structures of pure elements, and also of the polytypes possible for SiC, CdI$_2$ etc. Against this background, see also Table 3.1 summarizing the most important Laves-phase polytypes.

Table 3.1 The most important Laves-phase stacking types described as polytypes (see text).

stacking sequence	stacking sequence, "reduced"	Jagodzinski symbol[a] [9]	Ramsdell symbol [10]	Struktur-bericht sym-bol [11]	proto-type	space group
XzYxZy	XYZ	c	3C	C15	MgCu$_2$	$Fd\bar{3}m$
XzYz	XY	h	2H	C14	MgZn$_2$	$P6_3/mmc$
XzYxZxYz	XYZY	ch	4H	C36	MgNi$_2$	$P6_3/mmc$
XzYxZy-XyZxYz	XYZXZY	cch	6H[b]	--	--	$P6_3/mmc$

[a] The Jagodzinkski symbol indicates the stacking transition associated with a certain layer-sandwich unit: "h", if the layer-sandwich units above and below the respective layer are both at the same position and "c" if they are at different positions. The respective crystal structures are built up by infinite repetition of the stacking transitions given by the Jagodzinski symbols. To obtain one single, complete unit cell in stacking direction of the respective crystal structure, the number of layers given by the Ramsdell symbol is necessary; i.e. …ccc… for 3C, …hh… for 2H, …chch… for 4H and …cchcch… for 6H.
[b] This 6H-type structure is often referred to as 6H$_1$. The 6H$_2$ structure with the Jagodzinski symbol hchhhc is not considered here.

3.1.2 Partial-dislocation dipole mechanism for polymorphic transformations in Laves phases

The phase diagrams of many binary and ternary systems comprise several Laves-phase polytypes. The stability of a particular polytype can vary as function of composition or temperature (at constant pressure). A transformation from one to another polytype is in principle possible without need of long-range diffusion. A number of works have been dedicated in the past to the problem how such a polymorphic transformation can occur [7, 8, 12-14]. One main idea is that the layer-stacking sequences, considering only the layer-sandwich units, are changed by glide of partial dislocations, with six different Burgers vectors $\pm\mathbf{b}_1 = \pm\frac{1}{3}\left[10\bar{1}0\right]$, $\pm\mathbf{b}_2 = \pm\frac{1}{3}\left[\bar{1}100\right]$, and $\pm\mathbf{b}_3 = \pm\frac{1}{3}\left[0\bar{1}10\right]$ (Figure 3.2; employing Miller-Bravais indices for hexagonal crystal structure lattices, where the basis vectors $\mathbf{a}$ and $\mathbf{b}$ correspond to those used for the unit mesh mentioned in Section 3.1.1; cf. Figure 3.1), along the basal (0001) plane between two (assumedly rigid) *layer-sandwich units*. Thereby the relative position of the layer-sandwich unit, say "above" the (0001) glide plane becomes changed with respect to that of the layer-

sandwich unit "below" the (0001) glide plane (Figure 3.3). Note that, as consequence of stacking rule (ii) indicated above, this glide process requires that the *single-layer unit* between the two *layer-sandwich units* has to move synchronously in another direction, but also within the glide plane. Thus the shear process associated with one of the above-mentioned Burgers vectors is actually a synchroshear process, which has been discussed in more detail elsewhere [7, 8, 15]. The corresponding *partial* dislocations are, therefore, called synchro-Shockley partial dislocations [15].
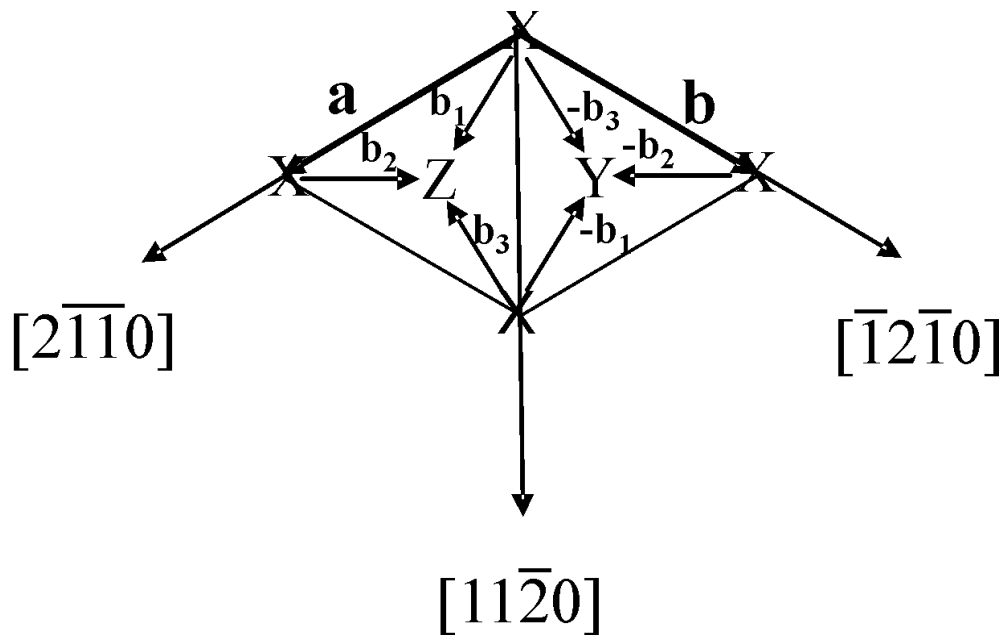
Figure 3.2: Stacking positions and Burgers vectors of partial dislocations in a (0001) plane of a Laves phase.
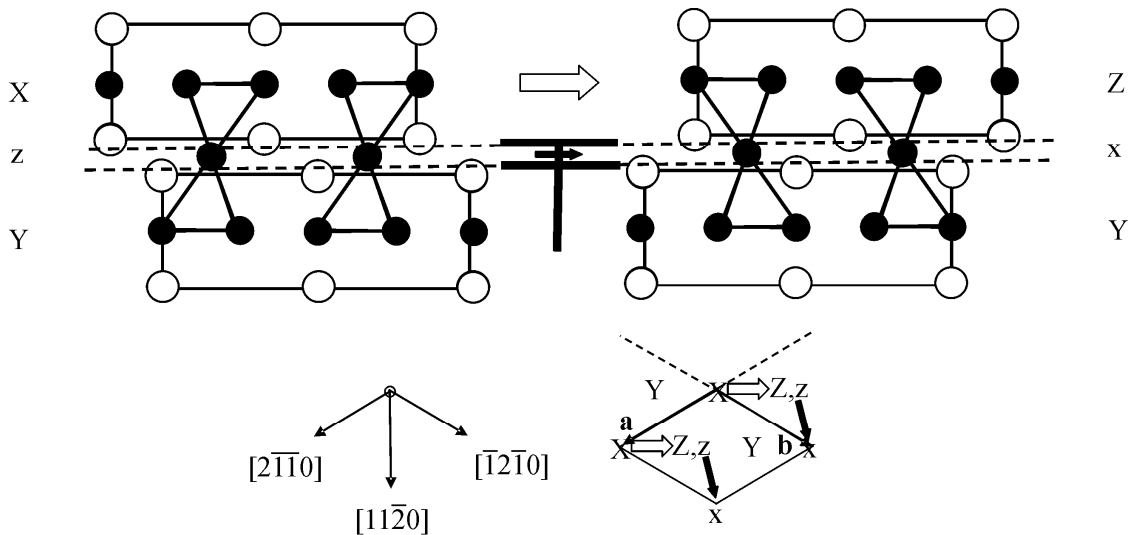
Figure 3.3: Change of layer-stacking sequence by glide of a single synchro-Shockley partial disloca-
tion. The layer-sandwich unit AB$_3$A, denoted by X in the left part of the figure, and the single-layer unit
B, denoted by z in the left part of the figure, are shifted along the (0001) glide plane according to differ-
ent Burgers vectors, as indicated in the [0001] projection in the bottom part of the figure: the white ar-
rows correspond to the Burgers vector associated with the shift of the layer-sandwich unit; the black
arrows correspond to the Burgers vector associated with the shift of the single-layer unit. The symbols ⊤
and ⊥ denote single synchro-Shockley partial dislocations with Burgers vectors of opposite sign. The
symbols ⊥ or ⊤ do not specify whether the dislocation is of edge-, screw- or mixed character.

It has been proposed [14, 15], supported by some experimental evidence (see
below) that, in case of a C14 (2H)→C36 (4H) transformation, such synchro-Shockley
partial dislocations as described above do not glide through the crystal independently.
Instead they glide as *dislocation dipoles,* where the two dislocations comprising the
dipole have Burgers vectors of opposite sign (e.g. $\mathbf{b}_1$ and $-\mathbf{b}_1$) and with one dislocation
travelling above and one dislocation travelling below a given *layer-sandwich unit.* As
net effect, only the middle layer-sandwich unit and the two adjacent single layer units
are shifted with respect to the initial stacking sequence, whereas the upper layer-
sandwich unit remains at its original position. Hence, glide of such dislocation dipoles
does not lead to a macroscopic shear of the crystal (see Figure 3.4) and thus can occur
under the constraint of conservation of shape of the crystal. Thus, simple, ordered
(i.e. periodic) sequences of such dislocation dipoles can bring about the 2H (C14)→4H
(C36) (Figure 3.5) and the 2H (C14)→6H transformation, which have been frequently
observed in real systems. Early high-resolution electron microscopy (HRTEM) studies
on TiCr$_2$, in which a C14→C36 transformation proceeds, revealed C36 domains grow-
ing parallel to the (0001) plane into the C14 matrix [13]. This observation is compati-
ble with the glide of synchro-Shockley partial dislocation dipoles as transformation
mechanism.
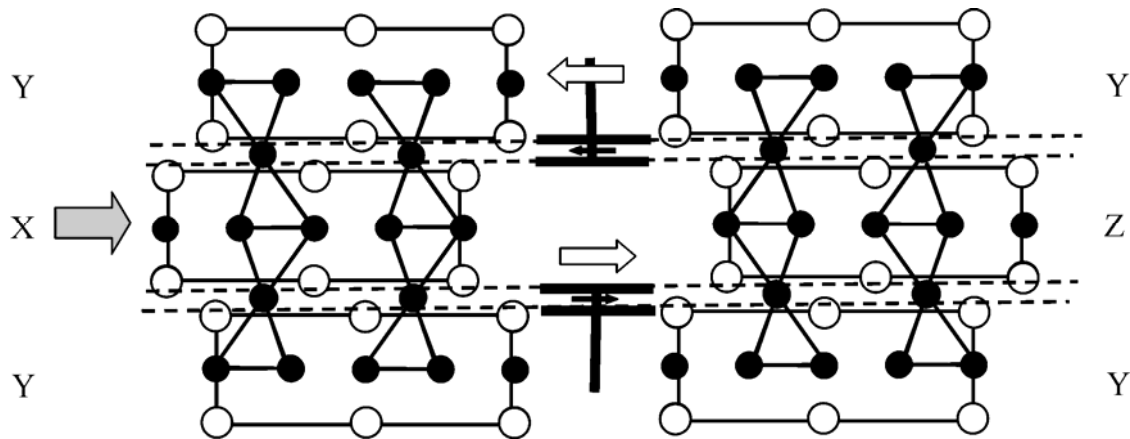
Figure 3.4: Change of stacking sequence in a Laves-phase crystal (as indicated by the layer-sandwich units) by passage of a synchro-Shockley partial dislocation dipole, in order to preserve the external shape of the crystal: note the absence of macroscopic shear for the crystal concerned, in contrast with the situation realized by passage of a single synchro-Shockley partial dislocation as sketched in Figure 3.3. For white and black arrows, see Figure 3.3. The grey arrow indicates the effective shift of the middle layer-sandwich upon passage of the dipole.

In the present publication layer faulting in three C36-type Laves phases ($NbCr_2$, $TiCr_2$, $NbCo_2$; see the phase diagrams provided by Figure 3.6) have been studied by transmission electron microscopy and X-ray powder diffraction. It was found that the investigated C36-$NbCr_2$ and C36-$TiCr_2$ Laves phases contain specific stacking irregularities. These are compatible with the occurrence of specific irregularities in the periodic passage of the synchro-Shockley partial dislocation dipoles in the course of the 2H (C14)→4H (C36) transformation, experienced by the $NbCr_2$ and $TiCr_2$ specimens. In contrast with these observations, the C36-$NbCo_2$ Laves phase does not contain such layer-stacking faults: a 2H (C14)→4H (C36) transformation does not occur during formation of C36-$NbCo_2$ (cf. Figure 3.6c).

2H (C14)   4H (C36)
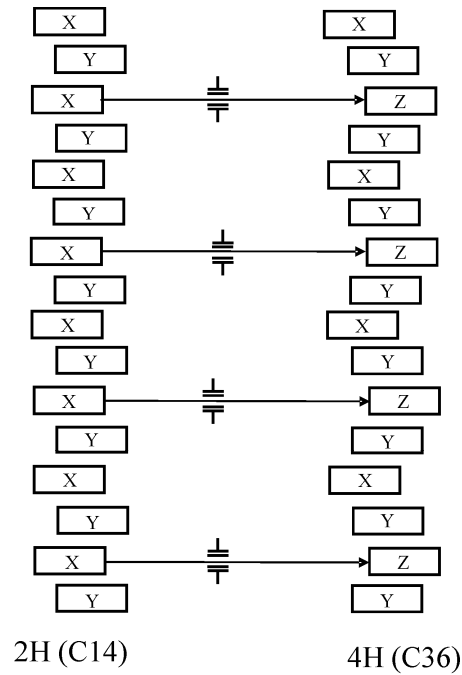
Figure 3.5: Formation of the 4H stacking sequence of C36 from the 2H stacking sequence of C14 by passage by glide of an ordered sequence of synchro-Shockley partial dislocation dipoles (the symbols ⊤ and ⊥ denote single synchro-Shockley partial dislocations with Burgers vectors of opposite sign).
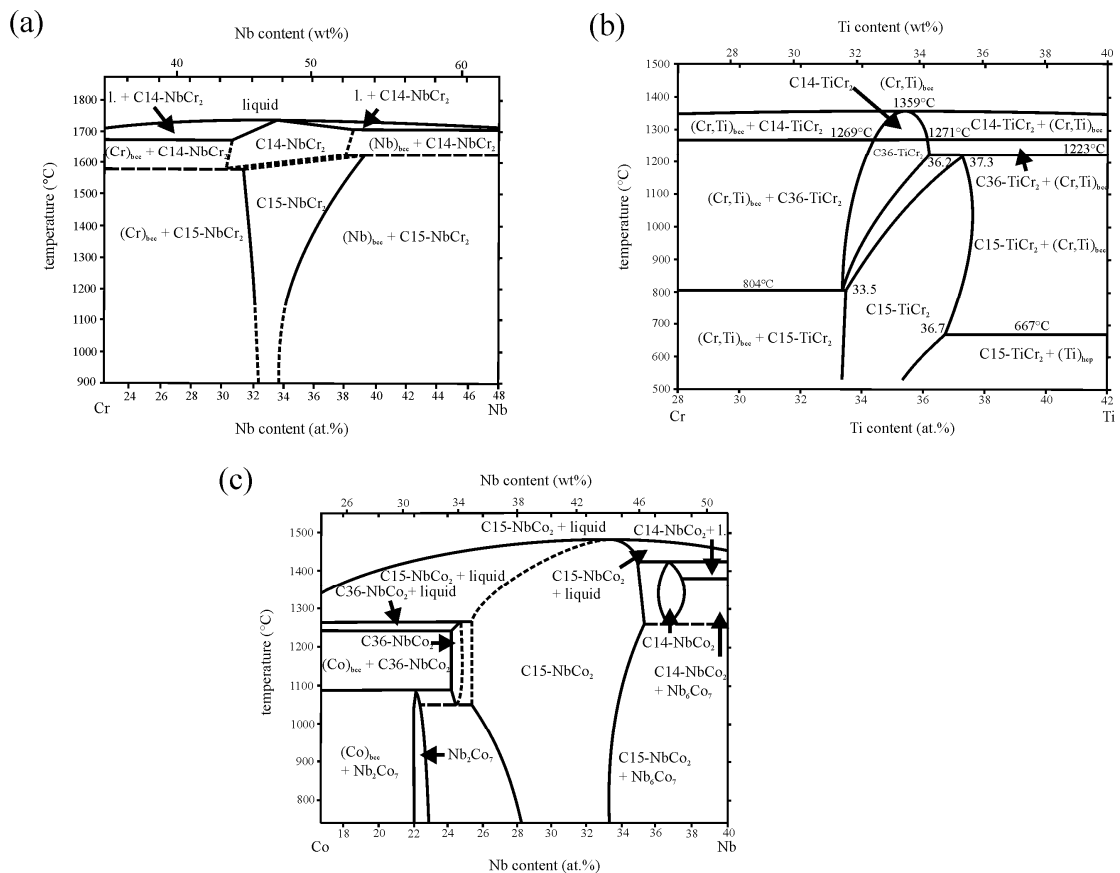
Figure 3.6: Laves-phase containing composition ranges of the phase diagrams of the systems (a) Nb-Cr [16], (b) Ti-Cr [17, 18] and (c) Nb-Co [19]. Note that in case of NbCr$_2$ the C14-NbCr$_2$ Laves phase (and also the C36-NbCr$_2$ Laves phase) is no equilibrium phase, as shown recently in Ref. [20].

3.1.3 Diffraction from layered hexagonal structures containing stacking irregularities

The effect of a stacking irregularity like a single stacking fault, and also of a combination of stacking faults, in a layered structure on its diffraction pattern can be understood as follows: a single stacking irregularity separates two halves of a crystal (Figure 3.7). Then the unit cells of the one half of the crystal with respect to the other half may be shifted by a *displacement vector* $\Delta\mathbf{r} = u'\mathbf{a} + v'\mathbf{b} + w'\mathbf{c}$ with, in general, real-valued *u'*, *v'*, and *w'*, and **a**, **b**, **c** as the basis vectors of the translation lattice. Non-integer *u'*, *v'* and *w'* imply that for certain (some, all or most) diffraction vectors $\mathbf{g} = h\mathbf{a}^* + k\mathbf{b}^* + l\mathbf{c}^*$, with *h*, *k* and *l* as integer-valued Miller (actually Laue) indices and **a***, **b*** and **c*** as the reciprocal basis vectors of the crystal, a phase shift occurs between the diffraction waves emanating from the two halves of the crystal. This phase shift can be shown to amount to $2\pi\mathbf{g}\cdot\Delta\mathbf{r} = 2\pi(u'h + v'k + w'l)$. No phase shift will occur for certain *hkl* if $\mathbf{g}\cdot\Delta\mathbf{r} = u'h + v'k + w'l$ assumes an integer value, and thus the reflections pertaining to these *hkl* do not broaden and do not shift (in reciprocal space). For a start, the absence of other line-broadening contributions is assumed. If $\mathbf{g}\cdot\Delta\mathbf{r}$ assumes an arbitrary, non-integer value, the otherwise delta-function shaped diffraction peak gets broadened and possibly shifted in reciprocal space into a direction perpendicular to the fault plane. For predicting how such broadening in reciprocal space will show up in an (X-ray) powder-diffraction pattern, it has to be considered that the line broadening in reciprocal space then gets projected onto the diffraction vector. For example, considering one crystal, if the stacking direction is parallel to **c*** and thus the fault plane is perpendicular to **c***, the line broadening in reciprocal space leads to a large line broadening in the X-ray diffractogram if $\mathbf{g} \parallel \mathbf{c}^*$. If $\mathbf{g} \perp \mathbf{c}^*$, no line broadening in the X-ray diffractogram results.

The actual line broadening in case of a polycrystal or powder containing many stacking faults will depend on the probability distribution of the different types of faults. Corresponding calculations have been performed for many types of layered structures, and computer programs are available to predict for general layered structures the layer-fault induced line broadening [21]. The line broadening (and the line shift) depends on the relative phases of the diffracted waves emanating from the two crystal parts separated by a stacking irregularity. Thus, for the Laves-phase crystal structures considered here, it suffices to refer to previously worked out predictions on line broadening in similar layered crystal structures in which same types of displace-

ment vectors occur upon varying the layer-stacking sequence. For 4H-type structures, as the C36-type Laves phase with its XYXZ stacking sequence, such results have been presented in Refs. [22, 23]. The different types of stacking faults considered in these works can be ascribed to only five types of displacement vector $\Delta\mathbf{r}$, which are indicated in the following by its coefficients (u',v',w'): $\pm(0,0,1/4)$, $(0,0,1/2)$, $\pm(1/3,2/3,0)$, $\pm(1/3,2/3,\pm1/4)$, $\pm(1/3,2/3,1/2)$; see Figure 3.7. Because of the translational symmetry of the crystals, all components u', v', w' of $\Delta\mathbf{r}$ are equivalent to u' mod 1, v' mod 1 and w' mod 1, respectively. The occurrence of one of these displacement vectors leads to a specific characteristic hkl dependence of the line broadening (and the line shift) in reciprocal space. The hkl dependence of the line broadening can be systematised by considering six classes of hkl reflections, depending on the values of $h - k$ and of l. Of these classes, one with $h - k = 3N$ and $l = 4M$ (with integer N, M) shows no line broadening for any of the five $\Delta\mathbf{r}$. Two further classes, with $h - k = 3N$ and $l = 4M \pm 1$, and with $h - k = 3N$ and $l = 4M + 2$, are irrelevant because their reflections have an integrated intensity of exactly or close to 0 (these classes were not considered explicitly in Refs. [22, 23]). Three further classes show line broadening characteristic for the corresponding type of $\Delta\mathbf{r}$, see Table 3.2. Note that the appearance of a "0" in a cell in Table 3.2 means that the reflections of that reflection class remain unbroadened for the type of displacement vector considered, which implies that $\mathbf{g}\cdot\Delta\mathbf{r} = u'h + v'k + w'l$ is an integer.
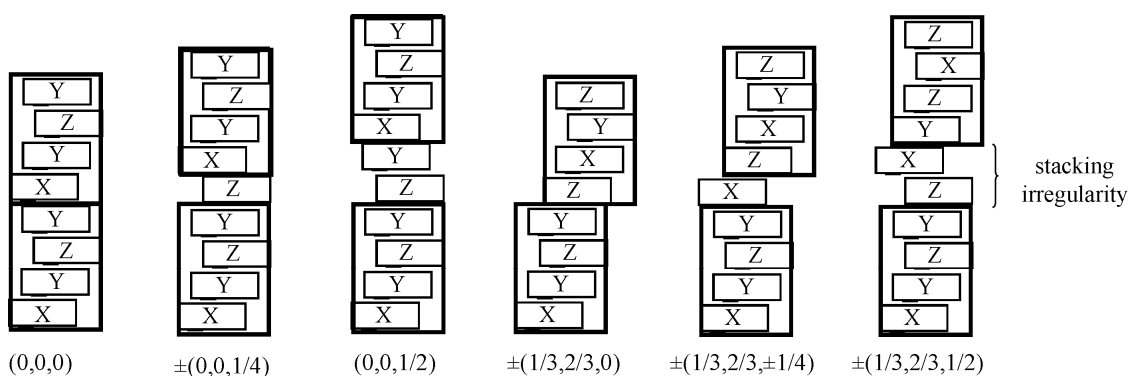
Figure 3.7: Graphical illustration of the five different stacking-fault displacement vectors between two halves of a C36 crystal separated by a stacking irregularity. The actual, here arbitrarily chosen atomistic structure of the irregularity itself has no or negligible influence on the line broadening in reciprocal space. Because of the periodicity of the crystal structure, the two displacement vectors $+(0,0,1/2)$ and $-(0,0,1/2)$ are identical, whereas displacements as $+(0,0,1/4)$ and $-(0,0,1/4)$ are not identical but equivalent with respect to the resulting line broadening.

Table 3.2 Extent of line broadening for a 4H-type crystal (as C36) along c* in reciprocal space as function of the displacement vector for four of the six reflection classes[a]. The width in reciprocal space units (here not specified) is proportional to the indicated numbers, as well as to the specimen-dependent probability for the occurrence of the corresponding displacement vectors. N and M are integers.

reflection-class; conditions for hkl	displacement vector, $\Delta\mathbf{r} = (u', v', w')$				
	$\pm(0,0,1/4)$	$(0,0,1/2)$	$\pm(1/3,2/3,0)$	$\pm(1/3,2/3,\pm1/4)$	$\pm(1/3,2/3,\pm1/2)$
$h-k=3N$ $l=4M$	0	0	0	0	0
$h-k\neq3N$ $l=4M$	0	0	3	3	3
$h-k\neq3N$ $l=4M\pm1$	2	4	3	2	1
$h-k\neq3N$ $l=4M+2$	4	0	3	1	3

[a] The two additional reflection classes indicated by $h-k=3N$ and $l=4M\pm1$, and $h-k=3N$ and $l=4M+2$ are irrelevant due to the zero or negligible integrated intensity of the corresponding hkl reflections.

3.2 Experimental

3.2.1 Preparation of alloys

The NbCr$_2$ (target composition 34.5 at.% Nb) and the TiCr$_2$ (target composition 35.8 at.% Ti) alloys were prepared by arc melting high-purity metals (niobium 99.99 wt%, titanium 99.999 wt%; chromium 99.999 wt%) under a titanium-gettered argon atmosphere. To ensure chemical homogeneity, the samples were flipped, remelted and subsequently cooled down on a water-cooled copper hearth for several times. Although samples of various compositions were prepared, the observations presented here were found to be composition-independent and can be discussed by considering, exemplarily, specimens of the two compositions indicated above.

The NbCr$_2$ ingot was used as obtained after arc-melting because C36 material can only be obtained in as-cast conditions [24]. The TiCr$_2$ ingot was subjected to further heat treatments. First, the sample was annealed for 50 h at 1395 °C (in the bcc-solid solution region; cf. Figure 3.6b) to ensure chemical homogeneity, i.e. to eliminate the chemical inhomogeneity inherent to the dendritic as-cast structure. Thereafter, the

specimen was annealed for 50 h at 1200 °C (in the C36 Laves-phase region; cf. Figure 3.6b). These heat treatments were carried out in an induction furnace under a high-purity argon atmosphere. To this end, the sample was placed into an Y_2O_3 crucible which was covered with three Ti-getter sheets. Before starting the annealing, the furnace was evacuated and back-filled with argon for several times. After the annealing, the specimens were rapidly cooled down by switching off the furnace.

Preparation of the C36-type Nb-Co Laves phase (25.0 at.% Nb) powder, has been described in Ref. [25]. Note that this material has been considered here on the sole basis of its X-ray powder diffraction pattern.

Both the as-cast $NbCr_2$ alloy and the as-cast and heat treated $TiCr_2$ alloy were characterised by optical microscopy, scanning electron microscopy (SEM), and energy/wavelength dispersive X-ray analysis (EDX/EPMA-WDX electron probe microanalysis), X-ray powder diffractometry (XRPD) and high resolution transmission-electron microscopy (HRTEM).

For the HRTEM and XRPD measurements powders of the $NbCr_2$ and $TiCr_2$ alloys were produced within a mortar. In case of $NbCr_2$ the material was taken from the top of the ingots containing predominantly C36 phase [24]. In case of $TiCr_2$, for the XRPD both a fine and a coarse powder batch were produced. For the SEM and EDX/EPMA-WDX analyses metallographic cross sections were prepared which were manually ground and polished. A Cameca SX100 microprobe was employed for the EPMA-WDX measurements, applying an acceleration voltage of 15 kV and a current of 40 nA. Elemental standards (Nb, Ti, Cr) were employed for quantification according to the $\Phi(\rho z)$ approach [26]. The electron backscattering diffraction (EBSD) measurements were conducted using a Zeiss LEO 438 VP scanning electron microscope equipped with an EBSD system (TSL, EDAX, Inc.) and the software OIM 4.5.

Chemical analysis by carrier-gas hot extraction (ELTRA ONH 2000), combustion technology (ELTRA CS-800) and Inductively Coupled Plasma Optical Emission (Spectro – CIROS CCD) showed that no uptake of metallic or non-metallic impurities had occurred during sample production and treatment.

3.2.2 High-resolution transmission-electron microscopy (HRTEM)

Due to the brittle nature of the investigated coarsely ground $NbCr_2$ and $TiCr_2$ powders, the edges of the powder particles were thin enough for electron transmission. The powder was suspended in n-butanole. Afterwards, a holey-carbon covered copper net was covered with that suspension leaving behind, after evaporation of the liquid, wedge-shaped crystallites in random orientation transparent for electrons. HRTEM was performed using a Philips CM 30 with an accelerating voltage of 300 kV.

3.2.3 X-ray powder diffraction (XRPD)

XRPD was performed using a "Philips X`Pert MPD" diffractometer equipped with a germanium-monochromator in the incident beam, selecting Cu-Kα_1 radiation.

In case of the $TiCr_2$ powder specimen, for correction of instrumental broadening, the instrumental line-profile contributions were determined using a LaB_6 powder sample (NIST standard reference material, SRM660a) using TOPAS [27]. These instrumental contributions were then convoluted with pseudo-Voigt functions which were fitted to the reflections of the experimental $TiCr_2$ diffraction patterns by least squares minimization. The fitting parameters were the reflection-maximum position, $2\theta_{max}$ and the full width at half maximum (FHWM) of the only structurally broadened line profiles; the line-shape parameter η was fixed to a value of 1.2 for all reflections[1]. Similar fits using pseudo-Voigt functions were conducted for $NbCr_2$, however, without separate consideration of the instrumental contribution (because of the considerably larger structural line broadening in case of $NbCr_2$) and with η as an additional fit parameter.

Diffraction patterns of the Nb-Co alloy powder specimen were recorded using a Huber G670 Guinier camera equipped with an incident-beam germanium monochromator, selecting Co-Kα_1 radiation. The powder was put as a thin layer on a Kapton foil. Like for $NbCr_2$, because of the relative large structural line broadening, without making separate consideration of the instrumental contribution, the reflection positions and widths were determined by fitting Lorentzian functions (corresponding to pseudo-Voigt functions with fixed $\eta = 1$; see also footnote) to each reflection.

---

[1] Fixing the peak-shape parameter η to a certain, reasonable value, removes the possible correlation of the FWHM and η in a fitting procedure and thereby the *hkl* dependency of the FWHM is more clearly exhibited. This procedure was necessary for the $TiCr_2$ powder specimen and for also the Nb-Co alloy powder specimen.

3.3 Results

3.3.1 Nb-Cr

3.3.1.1 Phase analysis and composition

For the as-cast $NbCr_2$ specimens, a majority of crystallites of the hexagonal C36 modification occur at the top of the arc-melted ingot, together with a minor amount of (retained; cf. Figure 3.6a) hexagonal C14-type crystallites (see Figure 3.10a) and cubic C15 type crystallites [24]. The bottom part of the ingot mainly consists of the C15 modification. Recent research performed in the present project has demonstrated that the C14 and C36 modifications are metastable at all temperatures and form only upon solidification from the melt at the top of the initially arc-melted ingots, with the C36 phase forming by solid state transformation from the initially crystallized C14 (see Refs. [20, 24]). The powder used for the present study was taken from the top of the arc-melted ingot (cf. Section 3.2.1). Because, in order to maintain the C36 modification, the sample could not be homogenized rigorously (this would have led to transformation of the C14/C36 crystallites to C15; cf. Figure 3.6a) compositional inhomogeneities as a result of the solidification process are possible. The average niobium content of the sample was determined by EPMA-WDX to be equal to 34.9 ± 0.2 at.%. A niobium content somewhat higher than the target composition (34.5 at.%) can be ascribed to chromium evaporation during arc-melting.

3.3.1.2 XRPD

Although the powder taken from the top part of the as-cast specimen contains C14- and C15-type crystallites additional to the C36 majority phase crystallites (cf. Section 3.3.1.1), separate reflections of these minority phases are not visible in the X-ray diffraction pattern (Figure 3.8a) because they are superimposed on the C36 reflections occurring at the same values of the diffraction vector Q. In view of the tiny amounts of C14 and C15 phase, for the current purpose the diffraction patterns can yet be conceived as characteristic for the C36 phase.
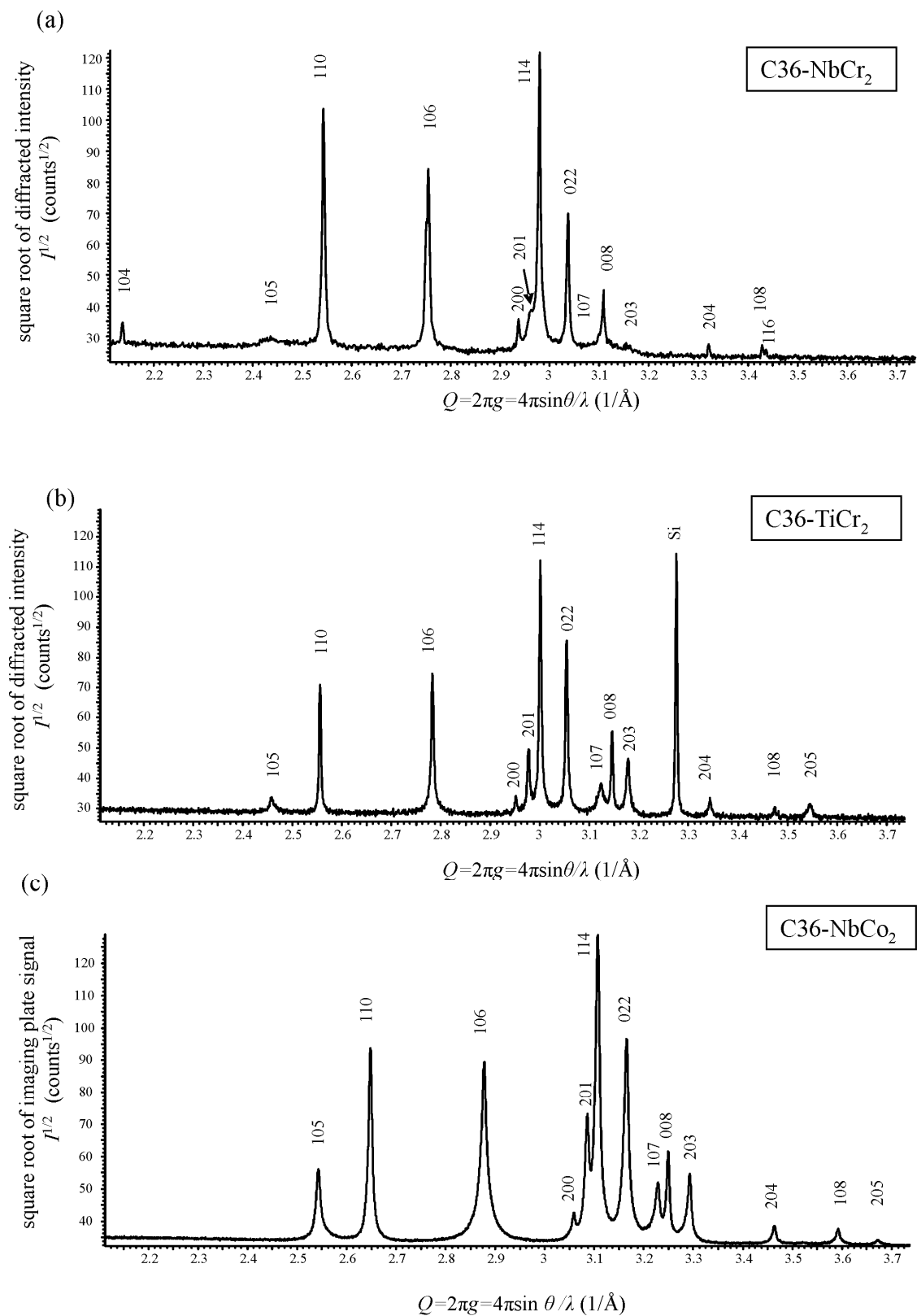
Figure 3.8: X-ray powder diffraction patterns: (a) C36-NbCr$_2$, powder as obtained from top of the arc-melted, solidified ingot (Cu- Kα1 radiation); (b) C36-TiCr$_2$ produced by solid-state annealing for 50 h at 1200 °C (coarse powder; Cu- Kα1 radiation); (c) C36-NbCo$_2$ (Co- Kα1 radiation). The Laue indices have been indicated.
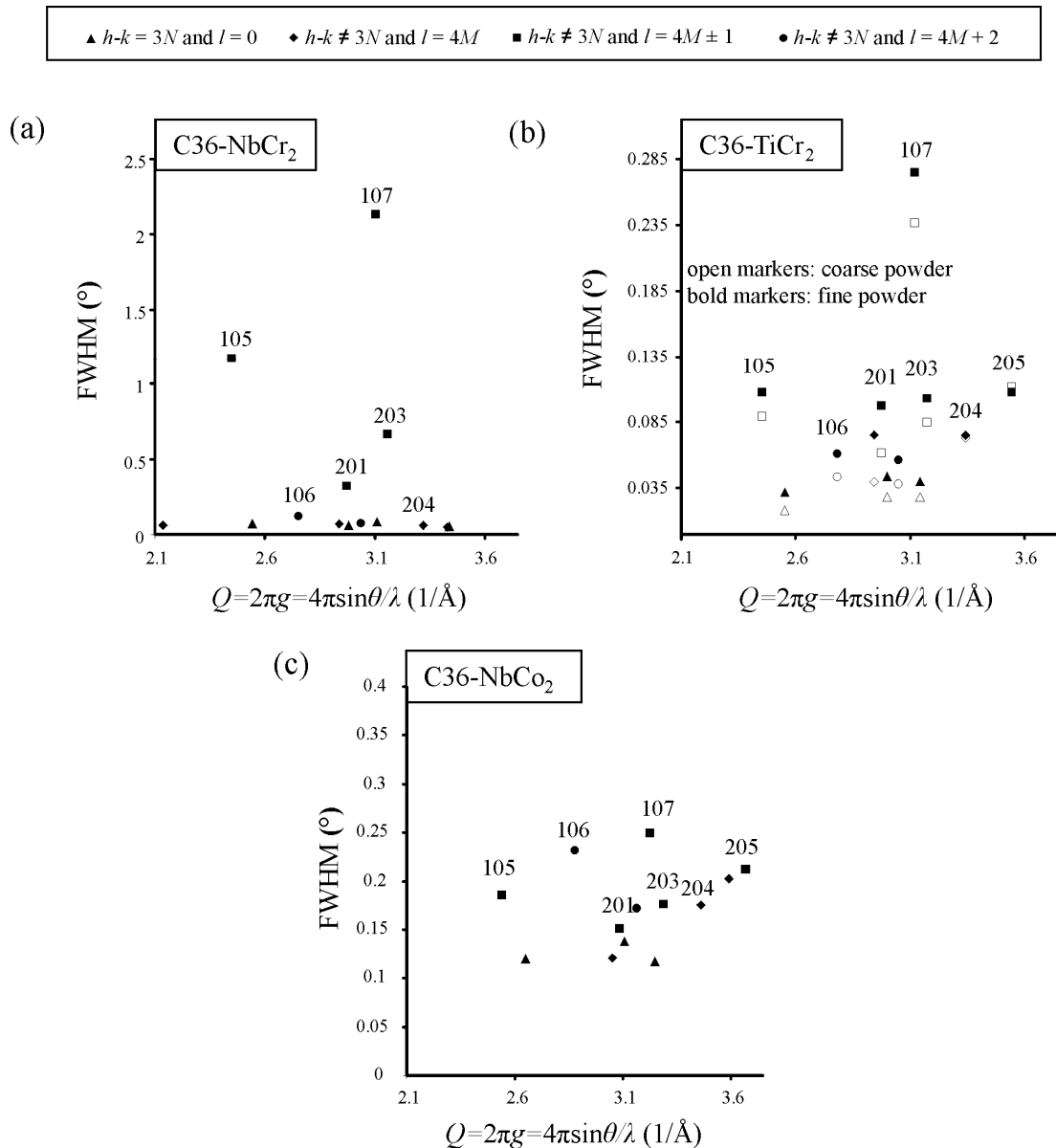
Figure 3.9: FHWM values of the reflections in the XRPD patterns of (a) C36-NbCr$_2$ as obtained from top of the arc-melted, solidified ingot (Cu-Kα1 radiation), (b) C36-TiCr$_2$ produced by solid-state annealing for 50 h at 1200 °C (coarse powder and fine powder, Cu-Kα1 radiation) and (c) C36-NbCo$_2$ (Co-Kα1 radiation).

The recorded diffraction pattern exhibits a distinct *hkl*-dependent broadening of reflections: The broadening occurs for (and is restricted to; see later) reflections with $h\text{-}k \neq 3N$ and $l = 4M \pm 1$ (see Figures 3.8a and 3.9a), as it is expected for layer-faulting induced line broadening for the C36 modification (cf. Table 3.2). The extent of the line broadening for these reflections increases with l (Figure 3.9a), leading to almost complete undetectability of reflections of high l values (see e.g. the 105 and 107 reflections in Figure 3.8a). All other reflections exhibit no appreciable broadening. Hence, (0,0,1/2) is the predominant displacement vector (cf. Table 3.2). This conclusion is supported by the observation that in particular the 106 reflection (belonging to the

$h - k \neq 3N$ and $l = 4M \pm 2$ reflection class) is narrow, whereas it would have broadened by the occurrence of all types of displacement vectors, in particular as promoted by its high l value, except for the occurrence of $(0,0,1/2)$ as displacement vector (Table 3.2).

3.3.1.3 HRTEM

A total of 15 crystallites from the $NbCr_2$ powder obtained from the top part of the as-cast ingot was examined by HRTEM. The C36 structure was found in 13 crystallites; in two cases together with some regions exhibiting the C14 modification and in two other cases together with some regions exhibiting the C15 modification. Only one crystallite was fully of the C14 modification, and one other crystallite was fully of the C15 modification. In many crystallites, a high density of layer-stacking irregularities was found, in association with streaks along the (hexagonal) $\langle 0001 \rangle$ direction in the selected area diffraction (SAD) patterns (Figure 3.10).
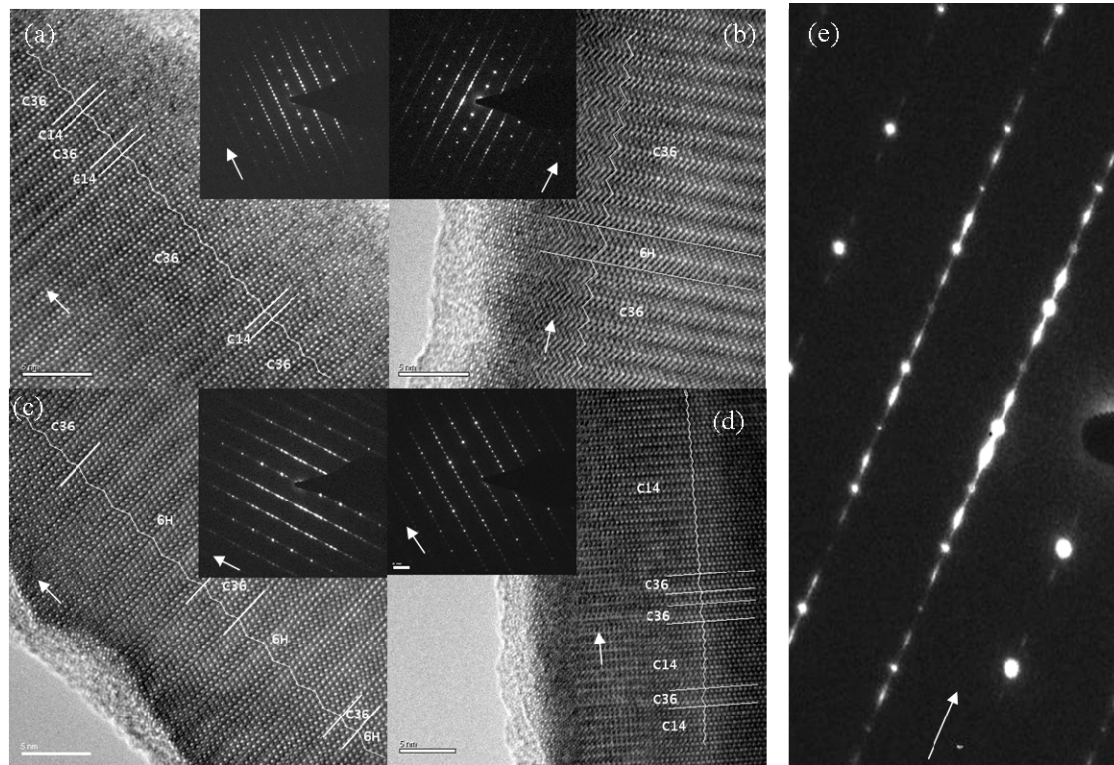
Figure 3.10: HRTEM images (C36 zone axis: $\langle 11\bar{2}0 \rangle$) of material taken from the top of an as-cast $NbCr_2$ specimen: (a-c) C36 crystallites with (a) 2H-type stacking irregularities; single (b) or an accumulation of (c) 6H-type stacking irregularities and (d) a retained C14 crystallite exhibiting 4H-type stacking irregularities; (e) enlargement of a part of the SAD pattern shown as insert in (b), revealing the streaking along the (hexagonal) $\langle 0001 \rangle$ direction. The arrows indicate the $\langle 0001 \rangle$ direction. The bars in (a-d) correspond to 5 nm.

Single faults (i.e. only one isolated "incorrect" *transition* between two layers (actually, two layer-sandwich units) with respect to the C36 layer-stacking sequence; cf. Figure 3.3)) were generally not found in the hexagonal C36 crystallites: instead, combinations of successive faults were observed which led to the emergence of inter-growth-type irregularities within the dominant C36 modification (Figures 3.10a-c). Similarly, intergrowth-type irregularities were observed within the minor retained C14 modification as well (Figure 3.10d).

With reference to Table 3.1, in case of the C36 modification (stacking sequence …chch…), one or multiple *2H-type* (C14-type) sequences (with stacking sequence -hh-) are observed (Figure 3.10a) and one or multiple *6H-type* sequences (with stacking sequence -cchcch-; Figures 3.10b,c).

In case of the C14 modification (stacking sequence …hh…), frequently one or multiple *4H-type* (C36-type) sequences (with stacking sequence –chch-) are found (Figure 3.10d). For distinction between the periodic Laves-phase crystal structure matrices and the local stacking irregularities, the Ramsdell notation is used for the stacking irregularities and the Strukturbericht designation for the matrices. Further, the periodic stacking sequences of the crystal structures will be enframed by the symbol "…", whereas the local stacking irregularities will be enframed by the symbol "-" to distinguish between the periodic stacking sequences of the matrices and the local layer configuration at the layer-stacking irregularities.

3.3.2 TiCr$_2$

3.3.2.1 Phase analysis and composition

The as-cast and heat treated (cf. Section 3.2.1) specimen consisted fully of C36-Laves phase (as determined by X-ray diffraction). According to wavelength dispersive X-ray analysis (EPMA-WDX) the composition of the Laves phase obeys (35.6 ± 0.3) at.% Ti and (64.4 ± 0.3) at.% Cr in agreement with the target composition (Section 3.2.1).

By optical microscopy and SEM the presence of a minority phase was detected (volume fraction approx. 1 % as determined by area analysis). The phase was identified by EBSD as a bcc phase. Standardless EDX analysis revealed that the minority phase is a Ti-rich phase. In view of the Ti-Cr phase diagram this suggests that this phase is the β-Ti solid solution.

3.3.2.2 XRPD

The diffraction pattern of the coarse powder (cf. Section 3.2.1) of the C36 phase is shown in Figure 3.8b. The FWHM of the reflections (shown in Figure 3.8b), after correction for instrumental broadening (see Section 3.2.3), has been plotted as function of the diffraction vector Q in Figure 3.9b.

The 110 reflection belongs to the class of reflections with $h - k = 3N$ and $l = 4M$. These reflections show no peak broadening due to layer-stacking irregularities (see Table 3.2), so that only broadening due to finite crystallite size and due to microstrains, caused by defects or composition variations, is possibly exhibited by these reflections. Assuming that the whole broadening of the 110 reflection is due to microstrain-like broadening caused by composition variations, an upper boundary for the width of the composition distribution equal to $B_\xi = 0.56$ at.% was calculated from the FWHM of the 110 reflection according to the method given in Ref. [28]. This B_ξ is the FWHM of a super-Lorentzian ($\eta = 1.2$, see Section 3.2.3) probability density function of the composition on the at.%-scale. Thus the maximum compositional variation was determined to be ± 0.28 at.%. This value is within the standard deviation of the WDX-EPMA analysis (cf. Section 3.3.2.1): such compositional variation cannot be exposed by EPMA-WDX analysis.

The peak broadening is affected by the grinding procedure: the peaks of the fine powder (more severely ground) are somewhat broader than the peaks of the coarse powder (less severely ground; see Figure 3.9b). This includes the reflection class with $h - k = 3N$ and $l = 4M$, as well. Since the $h - k \neq 3N$ reflections (which should show peak broadening due to (also) the layer-stacking irregularities, in addition to microstrains, as discussed above (cf. Table 3.2)) of the fine powder, as compared to the coarse powder, reveal extra broadening to about the same extent as reflections of the reflection class with $h - k = 3N$ and $l = 4M$, it can be concluded that the grinding procedure does not influence the layer-stacking irregularity density.

The powder-diffraction pattern of the C36 phase exhibits a distinctly hkl-dependent broadening of reflections, which is of the same type as observed for C36-$NbCr_2$ (see Section 3.3.1.2): The reflections with $h - k \neq 3N$ and $l = 4M \pm 1$ show a considerable peak broadening. This means that in the case of $TiCr_2$ also (0,0,1/2) is the predominant displacement vector. However, in contrast to C36-$NbCr_2$, the reflections with $h - k \neq 3N$ and $l = 4M$ (e.g. 204) and those with $h - k \neq 3N$ and $l = 4M + 2$ (e.g. 106) show a slightly larger peak broadening than the reflections with $h - k = 3N$

and $l = 4M$. This indicates that in case of TiCr$_2$ also layer-stacking irregularities with displacement vectors different from (0,0,1/2) occur.

3.3.2.3 HRTEM

A total of eight crystallites were investigated by HRTEM. All crystallites are dominantly composed of the C36 modification. In one crystallite within the C36 phase a *2H-type* (C14-type) stacking irregularity was found and in another a *6H-type* stacking irregularity was found. Furthermore in one crystallite both an accumulation of three consecutive *2H-type* (-hh-) and a *6H-type* (-cchcch-) stacking irregularities was found (see Figure 3.11a). In addition one crystallite contained a "split" *6H-type* stacking sequence (i.e. two -cch- stacking sequences separated by a larger C36 block; see Figure 3.11b). In general, in the investigated C36-TiCr$_2$ specimen much fewer stacking irregularities occur than in the investigated C36-NbCr$_2$ specimen.
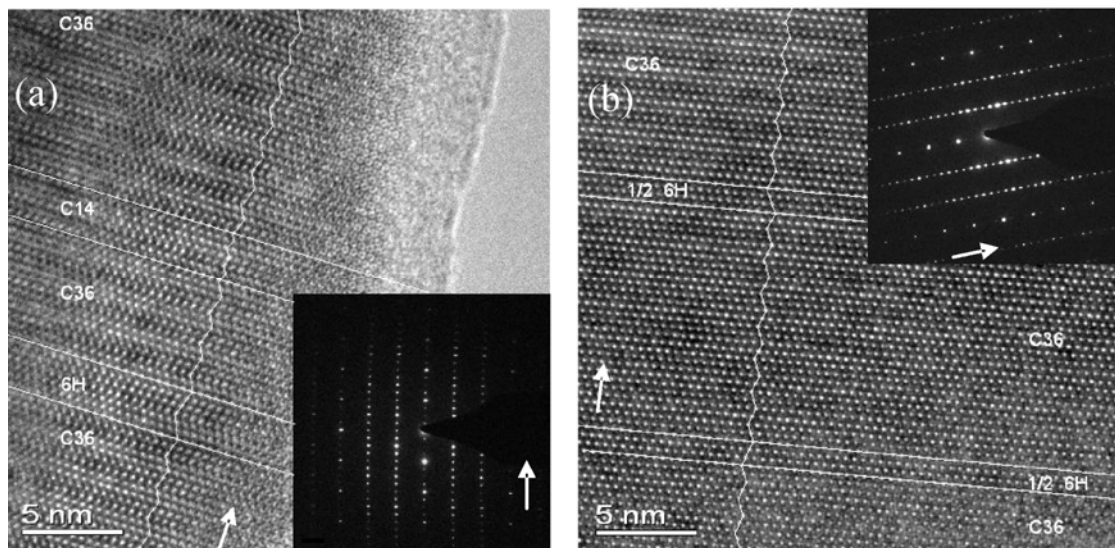
Figure 3.11: HRTEM images (C36 zone axis: $\langle 11\bar{2}0 \rangle$) of annealed C36-TiCr$_2$ specimens containing stacking irregularities. (a) A *2H-type* (C14-type) and a *6H-type* stacking irregularity, (b) a "split" *6H*-type stacking irregularity. The arrows indicate the 0 $\langle 0001 \rangle$ direction.

3.3.3 NbCo$_2$

The line broadening visible in the XRPD data of C36-NbCo$_2$ differs distinctly from that observed for the NbCr$_2$ and TiCr$_2$ analogues (Figures 3.8a,b vs. Figure 3.8c). The reflections pertaining to all reflection classes with $h - k \neq 3N$ experience considerable line broadening (Figure 3.9c), in particular the prominent 106 reflection (belonging to the $h - k \neq 3N$ and $l = 4M + 2$ class of reflections) which is only marginally broadened in the case of the C36-TiCr$_2$ specimens (Figure 3.9b) and not broadened at all for the

C36-NbCr$_2$ specimen (Figure 3.9a). Moreover, distinctly asymmetric diffraction-line broadening occurs for the $h - k \neq 3N$ and $l = 4M + 1$ class of reflections, which has been reported in Ref. [23] as representative for stacking-layer faulting not characterized by the (0,0,1/2) displacement vector.

3.4 Discussion

3.4.1 Stacking irregularities and associated displacement vectors

Two predominant types of stacking irregularities are found in the equilibrated C36-TiCr$_2$ specimen and in the as-cast C36-NbCr$_2$ specimen by HRTEM: *single* and/or *multiple 2H-type* and *6H-type* (intergrowth-type) stacking irregularitie*s*. Insertion of a *2H-type* irregularity in a perfect C36 (4H) crystal leads to a displacement vector of (0,0,1/2) (cf. Section 3.1.2); insertion of a *6H type* irregularity requires a displacement vector of (0,0,3/2), which is equivalent to the displacement vector (0,0,1/2) due to the translational symmetry of the C36 (4H) crystal structure, comprising four layer-sandwich units (cf. Table 3.1). Further, because of this translational symmetry, accumulations of multiple *2H-type* or *6H-type* stacking irregularities, as frequently observed in the HRTEM images (e.g. Figures 3.10c and 3.11a), can only add up to a displacement vector equivalent to (0,0,0), which causes no peak broadening, or (0,0,1/2) which leads to broadening of reflections of the class with $h - k \neq 3N$ and $l = 4M \pm 1$. Then also reflections of the class with $h - k \neq 3N$ and $l = 4M + 2$ remain narrow, which would be not the case for (all) other possible displacement vectors (cf. Table 3.2).

Exactly these above-indicated broadening characteristics are observed in the XRPD patterns of C36-NbCr$_2$ and in those of C36-TiCr$_2$ (where the broadening was less pronounced).

A special case is the "split" *6H-type* irregularity observed in TiCr$_2$ (cf. Figure 3.11b). The displacement between the middle 4H (C36) part, which is bounded by the two -cch- stacking irregularities, which can be regarded as a split-up 6H (-cchcch-) stacking sequence, and the two adjacent parts of the 4H crystal is of type $\pm$(1/3,2/3,+1/4); the displacement vector between the two adjacent parts of the 4H crystal separated by the whole "split" *6H-type* irregularity is again of type (0,0,1/2).

HRTEM and XRPD line-profile analysis give complementary results: HRTEM reveals the detailed structure of individual stacking irregularities, whereas XRPD provides data pertaining to the average microstructure. It thus follows that the *2H-type* and *6H-type* stacking irregularities are the dominating layer-stacking defects in C36-type NbCr$_2$ and TiCr$_2$ Laves phases.

3.4.2 Relation with phase-transformation mechanism

3.4.2.1 General remarks

The similarity of the stacking irregularities occurring in C36-TiCr$_2$ and C36-NbCr$_2$ (i.e. the occurrence of the same type of displacement vector; cf. Section 3.4.1) suggests that the origin of these stacking irregularities is the same for both Laves phases. A very remarkable feature of the stacking irregularities with a displacement vector of (0,0,1/2), is that no shear displacement of the part of the crystal above the irregularity occurs with respect to the part of the crystal below the irregularity: i.e. $u' = v' = 0$ (see Figure 3.7). It can thus be concluded that these stacking irregularities are not induced by plastic deformation processes possibly occurring during sample preparation, e.g. by thermal stresses. Indeed, as demonstrated in Section 3.3.1.3, the grinding procedure has no influence on the density of the stacking irregularities.

It is supposed that both C36 Laves phases, NbCr$_2$ and TiCr$_2$, have been formed from a C14-type structure, which evolves in case of NbCr$_2$ as a metastable state (cf. Section 3.3.1.1) during solidification at certain locations in the ingot [20, 24] and in case of TiCr$_2$ as a stable state during the decrease of annealing temperature from 1395 °C (bcc-solid solution) to 1200 °C (cf. phase diagram, Figure 3.6b); in this temperature range, the C14 phase field of TiCr$_2$ is passed. In Section 3.1.2 it has been discussed how a C14 crystal can transform into C36 by passage of a periodic series of synchro-Shockley partial dislocation dipoles ("ordered glide", Figures 3.4 and 3.5). The passage of one synchro-Shockley partial dislocation dipole within a C14 structure (as shown in Figure 3.4), generates a layer-stacking irregularity of 4H-type (C36-type) –YZYX- (-chch-) into the …XYXY… (…hh…) stacking sequence of C14. Due to the opposite sign of the Burgers vectors of the partial dislocations forming the dipole, the overall Burgers vector associated with this defect is zero, and thus no macroscopic displacement will be induced between the parts of the C14 crystal adjacent to such a defect (see Figure 3.4). Such 4H-type layer stacking irregularities are experimentally

observed in the retained $NbCr_2$-C14 crystallites (Figure 3.10d). Only "ordered glide", i.e. glide of a synchro-Shockley partial dislocation dipole on (i.e. above and below) every fourth layer-sandwich unit over a certain range of the C14 crystal, generates the C36 modification. This "ordered glide" requires coordination of the gliding partial-dislocation dipoles in order to produce C36. If this order is kept perfectly over the whole crystal, a defect-free, perfect C36 crystal would result, and hence no layer-stacking irregularities (with respect to the C36 layer stacking) and no corresponding reflection broadening would occur.
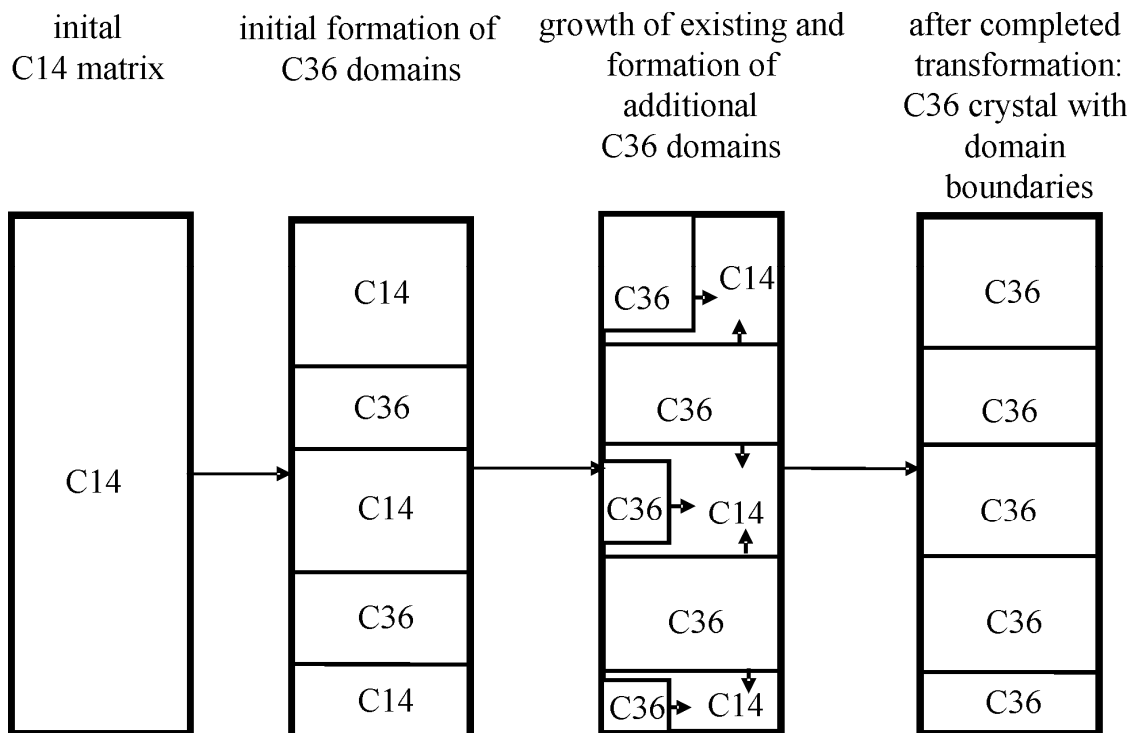
Figure 3.12: Formation of a C36 crystal by formation, growth and impingement of C36 domains.

Irregularities in the passage of the synchro-Shockley partial dislocation dipoles (i.e. deviations from "ordered glide") can be the origin of the layer-stacking irregularities in the C36-Laves phases as observed by HRTEM and XRPD in this work. Two mechanisms, which can occur simultaneously, are proposed in the following to explain the observed deviations. The first mechanism (Section 3.4.2.2) derives from the recognition that four different but energetically equivalent modes for formation of C36 are possible, depending on which of the four possible layers within two consecutive C14 unit cells (i.e. XYXY) is shifted to produce C36 (cf. Figure 3.4). If more than one of these modes is operative within one parent C14 crystal, initiating from different locations within the crystal, different C36 *domains* form, and layer-stacking irregularities

occur upon impingement of these domains (Figure 3.12). Yet, this first mechanism involves perfect, "ordered glide" within each domain. The second mechanism (Section 3.4.2.3) involves the occurrence of local deviation from "ordered glide", i.e. within a domain, leading to breaking up of the domain into *regimes*.

3.4.2.2 Domain formation

The requirement that every fourth layer-sandwich unit has to be displaced for the formation of C36 from C14 necessitates to distinguish between every two adjacent layer-sandwich units in C14, which is done here by introducing Roman numerals as subscript (see Figure 3.13); the stacking sequence of a C14 crystallite would thus be …$X_I Y_I X_{II} Y_{II}$…. A C36 stacking can then be formed by shifting either all X_I to Z or all X_{II} to Z or all Y_I to Z or all Y_{II} to Z (cf. also Figure 3.13). Taking the initial C14 structure as reference, four different C36 product domains can thus be formed (similar to the domains found e.g. in ordered substitutional intermetallics/phases). In the first two cases, the shift is realized by a dipole consisting of the synchro-Shockley partial-dislocation pair $\mathbf{b}_i$/-$\mathbf{b}_i$, while in the last two cases, the pair of synchro-Shockley partial dislocations is -$\mathbf{b}_i$/$\mathbf{b}_i$ (cf. Figure 3.2). Note that the first Burgers vector of the pair indicates the shift of the layer-sandwich unit with respect to the, say, bottom part of the crystal concerned, while the second Burgers vector is necessary to shift (reversely) the, say, top part of the crystal back to its original position, thereby avoiding macroscopic shear of the crystal (see Figure 3.4). The four possible C36 structures formed by the four layer-shift options are not identical, but displaced with respect to each other by the displacement vectors indicated in Figure 3.13 and provided by Table 3.3[1]. The C36 domains thus formed either grow in **c** (stacking) direction by "ordered glide" of more synchro-Shockley partial-dislocation dipoles shifting the same type of layer-sandwich unit, or new domains form between the existing ones, which is shown schematically in Figure 3.12. Growth of existing domains and formation of new domains may also occur simultaneously. The crystal can be regarded as completely transformed from C14 to C36 after impingement of these domains.

A perfect (i.e. stacking-fault or layer-stacking irregularity free) C36 crystal can only result from a parent C14 crystal if *only one* of the above four layer-sandwich unit shift options is adopted throughout the crystal. In this case, for transitional stages as

---

[1] The layer-stacking irregularity occurring between a pair of such domains can be conceived as an anti-phase boundary.

well as for the end stage of the transformation, the displacement vectors between the various C36 domains would always be (0,0,0), and thus no phase shift of diffracted waves and hence no reflection broadening of reflections originating from the C36 domains in the XRPD pattern can occur. In this case, after impingement of the growing domains, a perfect C36 stacking sequence over the whole initial C14 crystallite results.
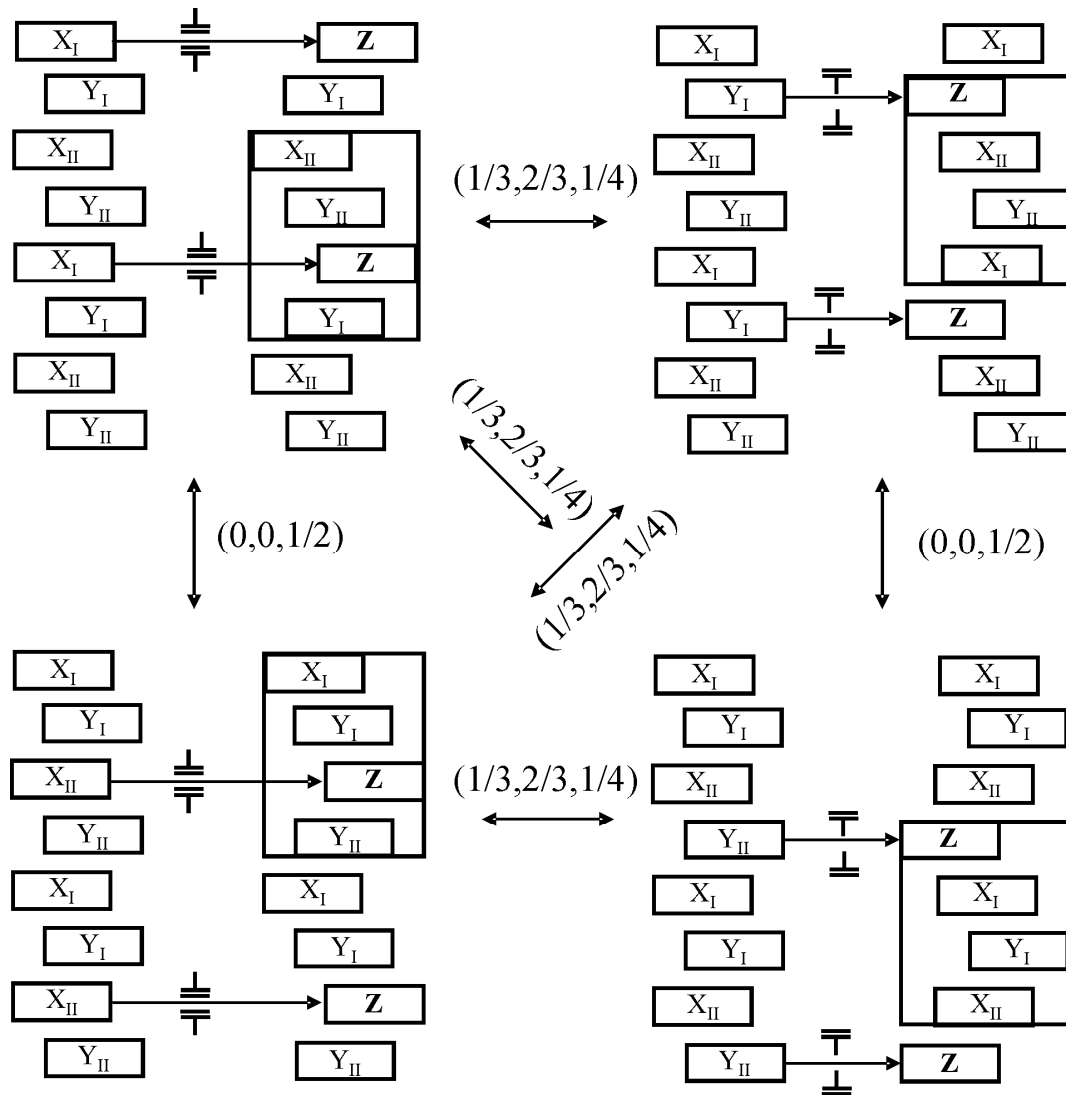
Figure 3.13: The four different C36 domains which can evolve from the same C14 crystal by shifting layer-sandwich units and the single (B atom) layer in-between by the ordered passage (glide) of synchro-Shockley partial dislocation dipoles (see Figures 3.4 and 3.5). The difference in Burgers vectors for the dipole pairs ($\mathbf{b}_i$/-$\mathbf{b}_i$ if X is shifted to Z and -$\mathbf{b}_i$/$\mathbf{b}_i$ if Y is shifted to Z) has been indicated by using the symbols ⊥̅, and ⊥̅) The corresponding displacement vectors between the resulting C36 domains have been indicated too. Note that for random occurrence of all four types of displacements (i.e. all four types of domains), the vector (1/3,2/3,1/4) occurs twice as frequently as the vector (0,0,1/2). The latter displacement occurs exclusively, if within a transformed crystal, only X layers or only Y layers have been displaced, i.e. either only the two domains shown on the left or only the two domains shown on the right, occur.

If the four types of domains shown in Figure 3.13 would occur randomly within a parent C14 crystal, the impingement (of the domains growing in the **c**-direction) be-

tween different domains, will lead to "anti-phase boundaries" (see footnote 3 of Chapter 3) because of the displacement between two impinging C36 structures: stacking irregularities occur associated with corresponding broadening of XRPD reflections according to the theoretical considerations in Section 3.1.3. Two types of displacement vectors can be indicated: (1/3,2/3,1/4) and (0,0,1/2), with the first ones occurring statistically twice as frequently as the latter one if all four types of domains occur randomly (see Figure 3.13). This last phenomenon is not compatible with the present observations for the C36-NbCr$_2$ and C36-TiCr$_2$ specimens, revealing a predominant broadening of the reflections of the class with $h - k \neq 3N$ and $l = 4M \pm 1$, which implies that the (0,0,1/2) displacement vector is dominant, i.e. only X or only Y layer-sandwich units have been displaced within a parent C14 crystal (cf. Figure 3.13). In the case of TiCr$_2$, also $h - k \neq 3N$ reflections not pertaining to $l = 4M \pm 1$ are slightly broadened suggesting a minor mixed occurrence (i.e. both X and Y) of layer-sandwich unit displacements within a parent C14 crystal. The "split" *6H-type* irregularity (Figure 3.11b; see Section 3.3.2.3) can thus be conceived as the outcome of impingement of three C36 domains. The upper and lower one are formed by e.g. shifts of X layers (e.g. X_I in the lower and X_{II} in the upper domain), whereas the middle domain is formed by e.g. shifting Y_{II} layers.

Table 3.3 Displacement vectors between C36 domains, produced in a parent C14 crystal by the synchro-Shockley partial dislocation dipole mechanism, by shifting for each domain one of the four different layer-sandwich units of the …$X_IY_IX_{II}Y_{II}$… sequence in the parent C14 structure to Z position (see Figure 3.13).

	X_I to Z	X_{II} to Z	Y_I to Z	Y_{II} to Z
X_I to Z	(0,0,0)	(0,0,1/2)	(1/3,2/3,1/4)	(1/3,2/3,1/4)
X_{II} to Z	(0,0,1/2)	(0,0,0)	(1/3,2/3,1/4)	(1/3,2/3,1/4)
Y_I to Z	(1/3,2/3,1/4)	(1/3,2/3,1/4)	(0,0,0)	(0,0,1/2)
Y_{II} to Z	(1/3,2/3,1/4)	(1/3,2/3,1/4)	(0,0,1/2)	(0,0,0)

3.4.2.3 Transformation errors

The "ordered glide" of synchro-Shockley partial dislocation dipoles is induced and controlled by the associated decrease in Gibbs energy of the transforming Laves phase (cf. Section 3.4.2.1). The "ordered glide" and thus the stacking sequence of the resulting C36 crystal will be practically perfect, if the energy "penalty" for deviations from this perfectly ordered glide is high compared to the decrease of Gibbs energy achieved by the transformation from C14 to C36. In case of Laves phases, the Gibbs energies of the different layer-sandwich unit stacking modifications differ only slightly (e.g. [29]) and hence the stacking fault energy is also low. Thus, deviations from perfect "ordered glide" are likely.

Irrespective of the precise origin of deviations from perfect "ordered glide", the most likely deviations are those which correspond most closely to the state of perfect order. Such most likely deviations are those which, nevertheless, satisfy the following characteristics of the *perfect* phase transformation:

- Glide of only synchro-Shockley partial dislocation *dipoles* is required to realize the irregularity
- Within one transforming domain, either only X or only Y layers are shifted to Z.

The last point involves that glide is realized by either only dipoles with the Burgers vectors $\mathbf{b}_i/\text{-}\mathbf{b}_i$ or only dipoles with the Burgers vectors $\text{-}\mathbf{b}_i/\mathbf{b}_i$.

Under these constraints, disorder in the passage of synchro-Shockley partial dislocation dipoles during the transformation occurs by a change of either X_I to X_{II} or Y_I to Y_{II} for the shifting layer-sandwich unit (Figure 3.14). Such changes can occur if either of the following scenarios takes place:

(i)   One (say, either X_I or Y_I) layer, which should have shifted according to perfect "ordered glide", remains immobile and "ordered glide", supposed to proceed in the c-direction, is continued by shifting the other representatives of the layers of the same stacking position (i.e. either X_{II} or Y_{II}, Figure 3.14a).

(ii)   A change of shifting layer (from either X_I to X_{II} or Y_I to Y_{II}) occurs without such preceding immobilisation, i.e. the distance between two shifted layers is two instead of four layers (Figure 3.14b).

Both such local deviations from perfect "ordered glide" are accompanied by the introduction of 2H-type layer-stacking irregularities; the displacement vector between the different 4H (C36) regimes is (0,0,1/2).
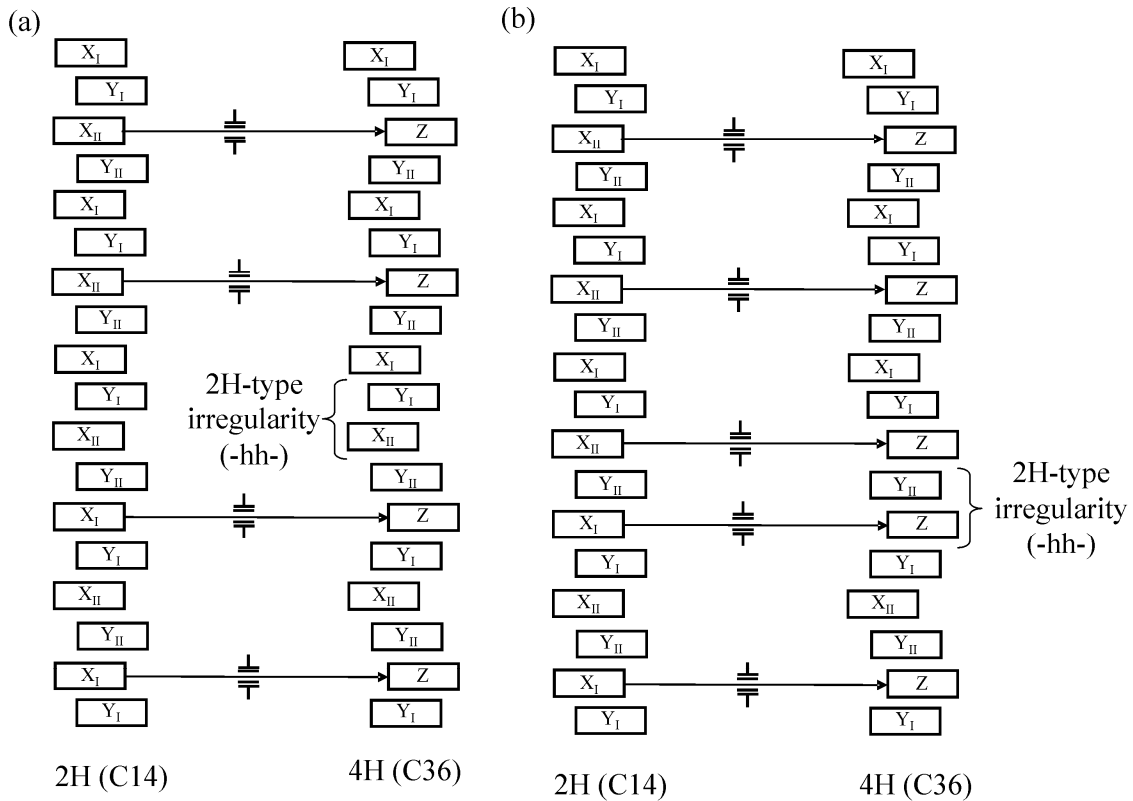
Figure 3.14: Possible deviations from perfect "ordered glide" of synchro-Shockley partial dislocation dipoles during a C14→C36 transformation, subject to the constraint that only one type of synchro-Shockley partial dislocation dipoles is involved in the phase transformations, i.e. either only X or only Y layers are shifted to Z positions (cf. Figure 3.13). For both cases shown in the figure, the layer shift switches from X_I to X_{II}. Contrarily to the occurrence of perfect "ordered glide" in the parent C14 crystal, where every second X layer is shifted to Z, either one X layer to be shifted becomes immobilized (a), or two adjacent X layers (i.e. an X_I layer *and* an X_{II} layer) are shifted to Z (b). In both cases, a *2H-type* stacking irregularity occurs.

Another possibility to introduce stacking irregularities in the product C36 crystal is that some of the synchro-Shockley partial dislocation dipoles are not separated by only one (cf. Figure 3.4) but by three layer-sandwich units (see Figure 3.15a). Such deviations also bring about a change of shifted layer type from either X_I to X_{II} or Y_I to Y_{II}, or vice-versa. The local stacking irregularity formed by such an "expanded" dipole is of *6H type*, the corresponding displacement vector between the adjacent 4H (C36) regimes is (0,0,1/2).

Formation of *6H-type* layer-stacking irregularities (Figure 3.15) may be a way to lower the energy increase associated with the introduction of the *2H-type* layer-stacking irregularities described above (Figure 3.14). This could occur upon further cooling (i.e. after completion of the C14→C36 transformation, assuming that (for

some temperatures range) below the C14→C36 transformation temperature, a 6H stacking sequence has a lower Gibbs energy than a 2H stacking sequence. This process is shown in Figure 3.15b. It requires (with respect to Burgers vector pair) passage of the type of synchro-Shockley partial dislocation dipole with Burgers vectors of opposite signs as compared to those operating upon formation of the C36 structure from the parent C14 structure.
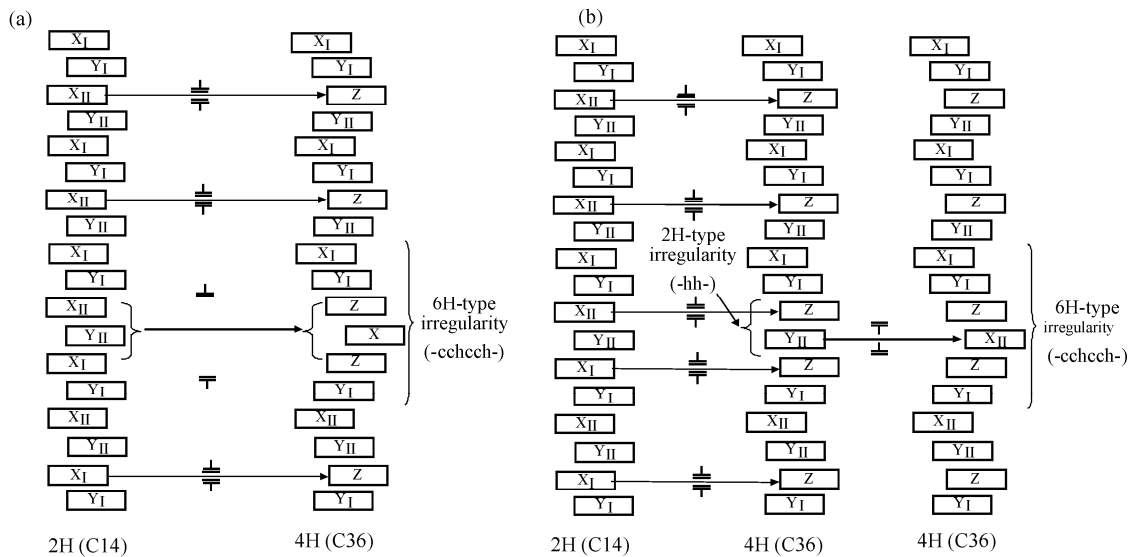
Figure 3.15: Formation of 6H-type stacking irregularities (a) during or (b) subsequent to a C14→C36 phase transformation: (a) glide of a synchro-Shockley partial dislocation dipole with a three-layer spacing between the two partials (instead of the regular single-layer spacing; cf. Figure 3.4) and (b) transition of a *2H-type* layer-stacking irregularity, to a *6H-type* layer-stacking irregularity within the defective C36 structure after the C14→C36 transformation (cf. Figure 3.14b); formation of the *6H-type* irregularity requires glide of a synchro-Shockley partial dislocation dipole with Burgers vectors of sign opposite from those of the synchro-Shockley partial dislocation dipoles which have formed the C36 structure to the C14 structure.

3.4.2.4 Overall discussion

In the two preceding sections, two mechanisms have been presented which induce stacking irregularities into a C36 product structure formed from a C14 parent structure by otherwise perfect "ordered glide" of synchro-Shockley partial dislocation dipoles. According to the first mechanism (Section 3.4.2.1) four different types of domains can be formed, which are not "in phase" with respect to each other, causing layer-stacking irregularities upon impingement of the domains. Within each domain perfect "ordered glide" of synchro-Shockley partial dislocation dipoles takes place and thus no layer-stacking irregularities occur within the domains. Two different displacement vectors occur between the different domains in this model: (1/3,2/3,1/4) and (0,0,1/2). In case of random occurrence of all four domain types the first displacement vector

(1/3,2/3,1/4) occurs statistically twice as often as the displacement vector (0,0,1/2). The experimentally observed dominance of the (0,0,1/2) displacement vector thus is ascribed to the presence of *2H-* and *6H-type* irregularities, induced by the second mechanism to generate stacking irregularities, i.e. by deviations from perfect "ordered glide" of synchro-Shockley partial dislocation dipoles during the transformation in a single domain (Section 3.4.2.2), leading to regime formation within the domains. It is shown that the smallest possible and simplest deviations lead to the *2H-* and *6H-type* layer-stacking irregularities as observed by HRTEM, associated with a displacement vector between the adjacent C36 crystal regimes of (0,0,1/2), as deduced from XRPD-line profile analysis.

The two mechanisms for generating stacking irregularities can operate jointly. Domain formation and impingement can occur *together* with flawed "ordered glide" during the transformation *within* the forming domains (transformation errors). The case that regime boundaries occur more frequently than domain boundaries has been schematically illustrated in Figure 3.16. In this case, using HRTEM, the probability of finding a 2H-type or 6H-type layer-stacking irregularity would be much higher than finding a domain boundary. Also the line broadening in XRPD patterns originating from such C36 structures would be dominated by the displacement vector (0,0,1/2), inducing pronounced broadening of reflections of the class with $h\text{-}k \neq 3N$ and $l = 4M \pm 1$. These predictions regarding the HRTEM and XRPD data agree fully with the corresponding observations made on C36-NbCr$_2$. Domain boundaries associated with a displacement vector of (1/3,2/3,1/4) would also induce some minor broadening of reflections of the classes $h\text{-}k \neq 3N$ with $l = 4M$ and $h\text{-}k \neq 3N$ with $l = 4M + 2$, in addition to broadening of reflections of the class $h\text{-}k \neq 3N$ and $l = 4M \pm 1$. This is in agreement with the experimental observations made on C36-TiCr$_2$.

The C36-NbCo$_2$ structure does not form by a C14→C36 transformation. Although a C14-NbCo$_2$ Laves phase exists at high Nb content, it is separated from the C36-phase field in the Nb-Co phase diagram by a C15-NbCo$_2$ phase [21] (see Figure 3.6c). Thus, the preferential formation of stacking irregularities with a (0,0,1/2) displacement vector, based on formation of C36 from (fault-free) C14, cannot pertain to C36-NbCo$_2$. The discussion of possible origins for the stacking-layer irregularities in C36-NbCo$_2$ (associated with only a minor occurrence of the displacement vector (0,0,1/2), but with major occurrence of other displacement vectors as listed in Table 3.2; see results reported in Section 3.3.1) is beyond the scope of the present paper.

C36-crystal formed
from C14

grain (crystallite) -
boundary

domain boundary   displacement vector:

(0,0,1/2) (33 %) or
(1/3,2/3,1/4) (67 %)

regime boundary   displacement vector:

= C14 or 6H-type   (0,0,1/2)
irregularity

stacking direction, c-axis
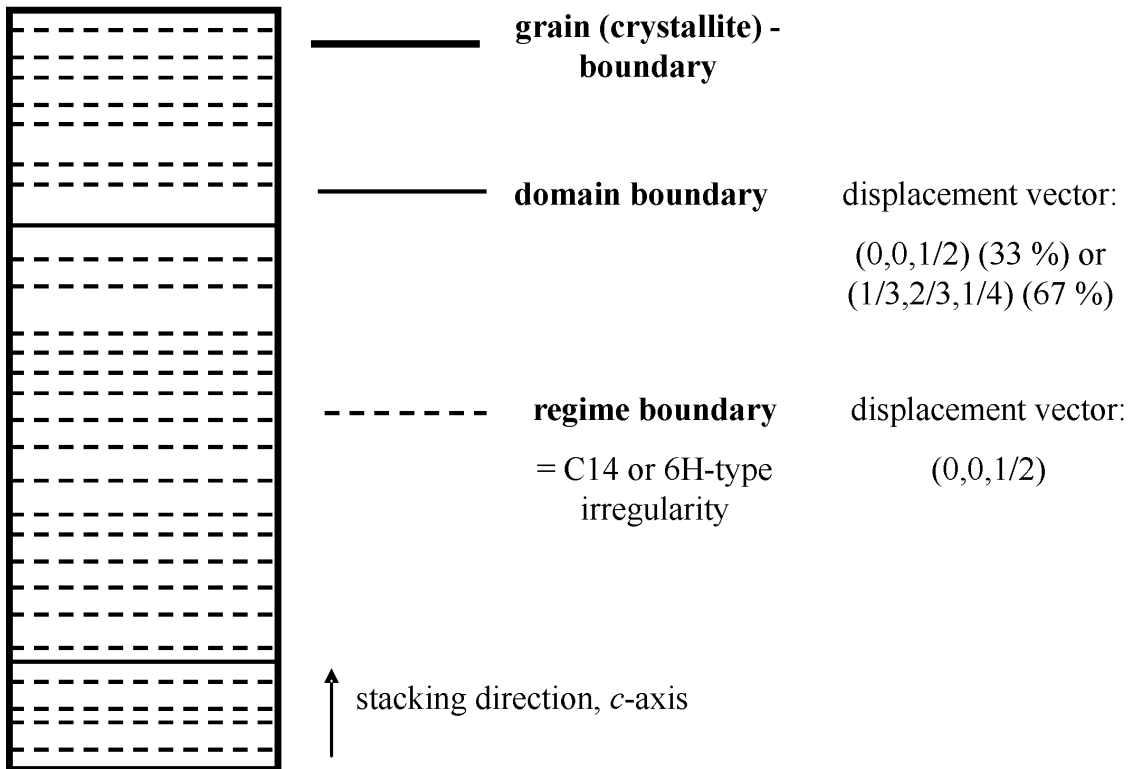
Figure 3.16: Hierarchy of stacking irregularities in a C36 crystal, as deduced from the results of the present XRPD and HRTEM investigations. The C36 crystallite has formed from a C14 crystal by glide of synchro-Shockley partial dislocation dipoles. The displacement vectors between the crystal parts adjacent to the various irregularities have been indicated, including the probabilities for the displacement vectors associated with the domain boundaries for the case that the four layer-sandwich unit shift possibilities (X_I, X_{II}, Y_I, Y_{II}) contribute equally.

3.5 Conclusions

- Irregularities in the layer-sandwich unit stacking sequences of C36 Laves phases (TiCr$_2$ and NbCr$_2$), which form from C14-type precursors, have been exhibited by HRTEM and XRPD-line profile analysis. The occurrence of such faulting provides validation of the proposed mechanism for the C14→C36 phase transformation by glide of a series of ordered synchro-Shockley partial dislocation dipoles ("ordered glide").

- Two mechanisms bringing about the (layer-sandwich unit) stacking irregularities have been identified:

(i)   Domain formation: Four different types of perfect C36 domains, which are displaced with respect to each other, occur simultaneously within one parent C14 crystal, leading to layer-stacking irregularities upon impingement of the growing domains.

(ii)   Transformation errors: Deviations occur from perfect "ordered glide" during the transformation within a domain.

- The predominant layer-stacking irregularities are *2H-* and *6H-type* stacking sequences within a domain, as evidenced by HRTEM and XRPD (selective broadening of the class of XRPD reflections with $h - k \neq 3N$ and $l = 4M \pm 1$ implying that stacking faults with a displacement vector of (0,0,1/2) are dominant): The transformation errors are the dominating layer-sandwich unit stacking irregularities for the investigated $C36\text{-}NbCr_2$ and $C36\text{-}TiCr_2$ Laves phases. The contribution of domain boundaries is negligible compared to that of the regime boundaries in case of $C36\text{-}NbCr_2$, but less so in case of $C36\text{-}TiCr_2$.

- $C36\text{-}NbCo_2$, which is not formed from a C14 precursor, (indeed) shows faulting distinctly different from $C36\text{-}TiCr_2$ and $C36\text{-}NbCr_2$.

3.6 Acknowledgement

3.7 References

[1]   G. Sauthoff, Intermetallics, Weinheim: VCH, 1995.

[2]   F. Stein, M. Palm, G. Sauthoff, Structure and stability of Laves phases. Part I. Critical assessment of factors controlling Laves phase stability, Intermetallics 12 (2004) 713.

[3]   F. Stein, M. Palm, G. Sauthoff, Structure and stability of Laves phases part II - structure type variations in binary and ternary systems, Intermetallics 13 (2005) 1056.

[4]   F.C. Frank, J.S. Kasper, Complex alloy structures regarded as sphere packings 1. Definitions and basic principles., Acta Crystallogr. 11 (1958) 184.

[5]   F.C. Frank, J.S. Kasper, Complex alloy structures regarded as sphere packings 2. Analysis and classification of representative structures, Acta Crystallogr. 12 (1959) 483.

[6]   C.W. Allen, P. Delavignette, S. Amelinckx, Electron microscopic studies of the Laves phases $TiCr_2$ and $TiCo_2$, Phys. Status Solidi A 9 (1972) 237.

[7]   P.M. Hazzledine, P. Pirouz, Synchroshear transformations in Laves phases, Scr. Metall. Mater. 28 (1993) 1277.

[8]   K.S. Kumar, P.M. Hazzledine, Polytypic transformations in Laves phases, Intermetallics 12 (2004) 763.

[9]   H. Jagodzinski, Eindimonsionale Fehlordnung in Kristallen und ihr Einfluss auf die Röntgeninterferenzen 1. Berechnung des Fehlordnungsgrades aus den Röntgenintensitäten, Acta Crystallogr. 2 (1949) 201.

[10]   L.S. Ramsdell, Studies on silicon carbide, Am. Mineral. 32 (1947) 64.

[11]   M.A. Barrett, T.B. Massalski, The structure of metals, New York: McGraw-Hill, 1966.

[12]   C.W. Allen, K.C. Liao. Shear transformations in the Laves phase $TiCr_2$. Proceedings -ICOMAT. Boston, 1979. p.124-129.

[13]   K.C. Liao, C.W. Allen. Shear transformation in the $TiCr_2$ Laves phase. International Conference of Solid-Solid Phase Transformations. Pittsburgh 1981. p.1493-1497.

[14]   C.W. Allen, K.C. Liao, Dislocation models for shear transformations, Phys. Status Solidi A 74 (1982) 673.

[15]   M.F. Chisholm, K.S. Kumar, P.M. Hazzledine, Dislocations in complex materials, Science 307 (2005) 701.

[16]   D.J. Thoma, J.H. Perepezko, An experimental evaluation of the phase relationships and solubilities in the Nb-Cr system, Mater. Sci. Eng., A 156 (1992) 97.

[17]   Z. Zhuang, J. Shen, Y. Liu, L. Ling, S. Shang, Y. Du, J.C. Schuster, Thermodynamic optimization of the Cr-Ti system, Z. Metallkd. 91 (2000) 121.

[18]   H. Okamoto, Chromium-titanium, Journal of Phase Equilibria 23 (2002) 382.

[19]   F. Stein, D. Jiang, M. Palm, G. Sauthoff, D. Gruner, G. Kreiner, Experimental reinvestigation of the Co-Nb phase diagram, Intermetallics 16 (2008) 785.

[20]   J. Aufrecht, A. Leineweber, A. Senyshyn, E.J. Mittemeijer, The absence of a stable hexagonal Laves phase modification ($NbCr_2$) in the Nb-Cr system, Scripta Mater. 62 (2010) 227.

[21]   M. Leoni, Diffraction analysis of layer disorder, Z. Kristallogr. 223 (2008) 561.

[22]   B. Prasad, S. Lele, X-ray diffraction from double hexagonal close-packed crystals with stacking faults, Acta Crystallogr., Sect. A: Found. Crystallogr. 27 (1971) 54.

[23]   E. Michalski, S. Kaczmarek, M. Demianiuk, The diffraction of X-rays by close-packed polytypic crystals containing single stacking-faults 2. Theory for hexagonal and rhombohedral structures, Acta Crystallogr. A 44 (1988) 650.

[24]   J. Aufrecht, A. Leineweber, E.J. Mittemeijer, Metastable hexagonal modifications of the $NbCr_2$ Laves phase as function of cooling rate, Advanced Intermetallic-Based Alloys for Extreme Environment and Energy Applications (2009) 481.

[25]   D. Gruner, F. Stein, M. Palm, J. Konrad, A. Ormeci, W. Schnelle, Y. Grin, G. Kreiner, Preparation, phase stability and structure of the C36 Laves phase $Nb_{1-x}Co_{2+x}$, Z. Kristallogr. 221 (2006) 319.

[26]   J.L. Pouchou, F. Pichoir, A new model for quantitative X-ray-microanalysis 1. Application to the analysis of homogeneous samples, Recherche Aerospatiale (1984) 167.

[27]   Topas, General Profile and Structure Analysis Software for Powder Diffraction Data, Version 3, Bruker AXS GmbH, Karlsruhe, 2003.

[28]   A. Leineweber, E.J. Mittemeijer, Diffraction line broadening due to lattice parameter variations caused by a spatially varying scalar variable: its orientation dependence caused by locally varying nitrogen content in ε-$FeN_{0.433}$, J. Appl. Crystallogr. 37 (2004) 123.

[29]   O. Vedmedenko, F. Rösch, C. Elsässer, First-principles density functional theory study of phase transformations in $NbCr_2$ $TaCr_2$, Acta Mater. 56 (2008) 4984.

Chapter 4

Failure of Kissinger(-like) methods for determination of the activation energy of phase transformations in the vicinity of the equilibrium phase-transformation temperature

Wolfgang Baumann, Andreas Leineweber and Eric Jan Mittemeijer

Abstract

The activation energies of heterogeneous equilibrium phase transformations have been frequently determined by Kissinger(-like) analysis. This work demonstrates that the applicability of Kissinger(-like) method(s) to determine activation energies of heterogeneous phase transformations is justified if the phase transformation occurs far away from the equilibrium phase-transformation temperature but not if the phase transformation is investigated in the vicinity of the equilibrium phase-transformation temperature. Experimental results on the kinetics of the order-disorder transformation in Ni_3Sn_2 obtained both near the equilibrium phase transformation temperature and considerably below it (using quenched samples) expose the non-validity and confirm the validity, respectively, of activation-energy values obtained by Kissinger(-like) analyses applied in the corresponding temperature ranges. Application of the Kissinger(-like) analysis in a temperature range close to the equilibrium phase-transformation temperature leads to erroneous, abnormally high values for the activation energy.

4.1 Introduction

Nowadays, the so-called Kissinger method [1, 2] (and its derivatives; see a listing of these in Ref. [3]) is used extremely often to obtain values of (effective) activation energies of thermally activated reactions/transformations: For example the number of references to just the original works by Kissinger [1, 2], in the years 2006, 2007, 2008 and 2009 amounts to 290, 352, 409 and 418, respectively.

The method, as originally proposed, is based on the analysis of the maximum reaction/transformation rate as a function of (constant) heating rate (isochronal anneals). It was originally developed, using n^{th} order reaction kinetics ($n = 0, 1, 2...$), for homogeneous reactions (as occurring in liquids or gases) [1, 2]. Later it was shown [4] that a Kissinger-like method is also possible for heterogeneous (solid state) reactions/transformations. Usually one is not aware of this distinction and applies the Kissinger method to heterogeneous solid state transformations without recognising that the original Kissinger method cannot be applied without more ado to these cases. In the following we will therefore speak of Kissinger-like methods.

Kissinger-like methods are in particular popular for evaluation of heating-rate dependent differential thermal analysis (DTA) or differential scanning calorimetry (DSC) data, recorded for tracing e.g. precipitation reactions [5-7] and crystallization of metallic glasses [8-11].

Occasionally, the Kissinger-like method has been used to determine activation energies of equilibrium phase transformations $A \rightleftharpoons B$ occurring at the equilibrium phase-transformation temperature T_0, with A being stable below and B above T_0, (i.e. at T_0 both phases constitute a two-phase equilibrium). Strikingly, such kinetic analyses led to abnormally high values for the activation energy that appear to have no physical meaning [12-14]: For example, thus determined "activation-energy" values of 8500 kJ/mol, 1765 kJ/mol, 1860 kJ/mol and 963 kJ/mol were reported for an equilibrium phase transformation (i.e. occurring in the vicinity of T_0) between two polymorphs of $Ba_2In_2O_5$ [12], of potassium nitrate ($\alpha = A \rightarrow \beta = B$) [13], for hexamethylbenzene (triclinic $= A \rightarrow$ orthorhombic $= B$) [13], and for the melting of ice (H_2O (solid) $= A \rightarrow H_2O$ (liquid) $= B$) [14], respectively.

In the present paper it will be shown that such unreasonably high activation-energy values are a consequence of non-validity of (one of) the cardinal assumption(s)

made in the derivation of the Kissinger-like method and its variants. The discussion is presented by a consideration of the application of the Kissinger-like analysis to DSC data of the well-known order $\leftrightarrow$ disorder transformation LT $\rightarrow$ HT and HT $\rightarrow$ LT (LT = low-temperature phase, A); HT = high-temperature phase, B) of Ni_3Sn_2 ($Ni_{1.50}Sn$) [15, 16], in the vicinity of the equilibrium phase-transformation temperature $T_0 \approx 750 - 780$ K [17, 18] ($T_0 \approx 780$ K will be used in the following [18]) and considerably below it. It will be demonstrated that application of the Kissinger-like method(s) is only permitted in the second case.

4.2 Theoretical background

4.2.1 Kissinger-like method

The progress of a phase transformation[1] can be determined by measuring a macroscopic physical property of the transforming material (as length, hardness, resistivity, etc.). From such measurements the degree of transformation f can be calculated ($0 \leq f \leq 1$) as function of the temperature–time program ($T = T(t)$), to which the sample is subjected. The transformed fraction f of the sample is determined by the thermal history of the sample, i.e. for non-isothermal analysis t and T are not state variables for the degree of transformation f. Then, for isokinetic transformations (i.e. transformations following the same mechanism in the time-temperature window investigated) the transformation rate $\mathrm{d}f / \mathrm{d}t$ can be written as a product [4, 19-21]:

$$\frac{\mathrm{d}f}{\mathrm{d}t} = g(f)k(T), \qquad (4.1)$$

where $g(f)$ is a purely fraction-transformed f-dependent function and $k(T)$ is a purely temperature T-dependent function, which is commonly referred to as the rate constant[2]. For the rate constant an Arrhenius-type temperature dependence is adopted:

$$k(T) = k_0 \exp\left(-\frac{Q}{RT}\right), \qquad (4.2)$$

---

[1] Here the phase transformation A $\rightarrow$ B is focus of the attention. However, the considerations of Section 4.2.1 also pertain to other transformations, e.g. of the type A$\rightarrow$B + C, as long as start state and end state are identical for the range of temperatures for which the Arrhenius-type temperature dependence of the reaction rate (cf. Eq. (4.2)) is adopted.

[2] Note that without recourse to a specific rate law in practice explicit values for k are not determinable because g/A together with kA, with A being a f and T independent constant, gives the same transformation rate.

with Q as the activation energy, R as the gas constant and k_0 as the pre-exponential factor.

On this basis it has been shown in Ref. [4] that, independent of the nature of the transformation being homogeneous or heterogeneous, the temperature $T_{f'}$ corresponding to a fixed stage of transformation f' depends systematically on the heating rate $\Phi = \mathrm{d}T/\mathrm{d}t$ and it follows:

$$-\ln\frac{\Phi}{T_{f'}^2} = -c + \frac{Q}{RT_{f'}} \tag{4.3}$$

with c as a constant. This implies that from the values of the temperatures $T_{f'}$, determined for a number of constant heating rates Φ, a value for the activation energy can be obtained from the slope of the straight line fitted to the experimental data in a plot of $-\ln\dfrac{\Phi}{T_{f'}^2}$ vs. $\dfrac{1}{RT_{f'}}$ (cf. Equation (4.3)).

It has also been shown in Ref. [4] that the temperature of maximal transformation rate, T_M, always occurs at *about* the same value of f. Thus, the temperature $T_{f'}$ in Equation (4.3) can be replaced by the temperature of maximum transformation/reaction rate T_M (e.g. for differential scanning calorimetry measurements the temperature of maximum transformation/reaction rate is given by the peak temperature). This last much more restricted form of Equation (4.3) (i.e. with T_M instead of $T_{f'}$) is the original equation as derived by Kissinger [1, 2] for simple "n^{th} order reaction kinetics" occurring for homogeneous transformations. Hence, as long as the assumption of an Arrhenius-type temperature dependence for $k(T)$ is justified, a replacement of $T_{f'}$ by T_M is justified, and for both homogeneous and heterogeneous transformations.

The derivation of the Kissinger(-like) equation (Equation (4.3)) relies on the assumed Arrhenius-type temperature dependence for the rate constant (cf. Equation (4.2)). Then, for (solid state) heterogeneous transformations, governed by separate nucleation and growth (and impingement) modes, the assumption of an Arrhenius-type temperature dependence for $k(T)$ (see Equation (4.2)) requires that the temperature dependent sub-steps of the transformations, as nucleation and growth modes, are thermally activated according to an Arrhenius-type relationship. This needs not generally be the case, which is discussed next.

4.2.2 Nucleation

The classical theory of nucleation provides the following general expression for the nucleation rate per unit volume $\dot{N}(T(t))$ [22, 23]:

$$\dot{N}(T(t)) = C\omega \exp\left(-\frac{\Delta G^*(T(t)) + Q_N}{RT(t)}\right), \tag{4.4}$$

with C as the number density of nucleation sites, ω is a complex function that depends on the vibration frequency of the atoms, Q_N as the activation energy for atoms jumping through the interface and $\Delta G^*(T(t))$ as the critical Gibbs energy for nucleus formation (= formation of a particle of critical size).

Evidently, $\dot{N}(T(t))$ as given by Equation (4.4) does not obey an Arrhenius-type temperature dependence[1]. However, with increasing overheating or undercooling $\Delta G^*(T(t))$ decreases (e.g. for spherical nuclei $\Delta G^*(T(t))$ is approximately proportional to $\frac{1}{\Delta T^2}$ [24]) and becomes small as compared to RT. Then Equation (4.4) reduces to:

$$\dot{N}(T(t)) = N_0 \exp\left(-\frac{Q_N}{RT(t)}\right), \tag{4.5}$$

where N_0 denotes the temperature independent nucleation rate which contains $C\omega$. In this case the nucleation rate exhibits an Arrhenius-type temperature dependence.

4.2.3 Kinetics of growth

Two extreme cases of growth kinetics can be considered: Diffusion-controlled and interface-controlled growth [22, 23]. If long-range compositional changes are necessary for the phase transformation, diffusion plays a role, but needs not be dominating. Atomic-jump processes in the direct vicinity of (across) the interface may generally effect the growth rate and they dominate the growth rate (interface control) if the compositions of the parent phase and (the single) product phase are equal.

---

[1] For the extreme case of athermal nucleation, as possibly pertaining to martensitic transformations, the nucleation rate only depends on the undercooling/overheating $\Delta T(t)$.

4.2.3.1 Interface controlled growth

The growth velocity v in the case of interface-controlled growth is in general given by [22, 23]:

$$v(T(t)) = v_0 \exp\left(-\frac{Q_G}{RT(t)}\right)\left(1 - \exp\left(\frac{\Delta G}{RT(t)}\right)\right), \qquad (4.6)$$

with v_0 as a pre-exponential factor, Q_G as the activation energy of growth and ΔG as the Gibbs energy difference between the new phase and the parent phase.

Evidently, $v(T(t))$ as given by Equation (4.6) does not obey an Arrhenius-type temperature dependence. However, for large undercooling or overheating the absolute value of ΔG is large as compared to RT. Then Equation (4.6) reduces to:

$$v(T(t)) = v_0 \exp\left(-\frac{Q_G}{RT(t)}\right). \qquad (4.7)$$

In this case the growth velocity exhibits an Arrhenius-type temperature dependence.

In the vicinity of the equilibrium phase-transformation temperature T_0 (i.e. for small undercooling or overheating) the driving force $|\Delta G|$ is small as compared to RT and Equation (4.6) becomes

$$v(T(t)) = M_0 \exp\left(-\frac{Q_G}{RT(t)}\right)(-\Delta G(T(t))), \qquad (4.8)$$

with the mobility $M_0 = v_0/RT$.

4.2.3.2 Diffusion controlled growth

Also for the case of "diffusion controlled" growth a simple Arrhenius-type temperature dependence of the growth velocity does not generally hold, as can be demonstrated for precipitate-phase growth near the equilibrium phase transformation temperature T_0, as follows.

The growth velocity v of a precipitate $B(X_B)$ (with X_B as the molar fraction of solute in the precipitate) precipitating from the supersaturated solid solution $A(X_0)$ ($X_0 = $ (initial) molar fraction of solute in the bulk) according to

$$A(X_0) \rightarrow A'(X_e) + B(X_B), \qquad (4.9)$$
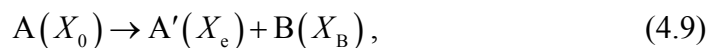
(X_e is the molar fraction of solute in the matrix adjacent to the $B(X_B)$-precipitate which can be taken equal to the equilibrium value [24]), can be given according to a simplified approach [25], for isothermal growth as:

$$v(T,t) = \frac{\Delta X_0}{2(X_B - X_e)} \sqrt{\frac{D}{t}}.$$
(4.10)

where $\Delta X_0 = X_0 - X_e$ denotes the "supersaturation" before the precipitation starts and D represents, the diffusion coefficient obeying an Arrhenius-type temperature dependence. X_e and X_B depend on temperature and X_0 depends on time. Evidently, $v(T,t)$ as given by Equation (4.10) does not obey an Arrhenius-type temperature dependence. At large undercooling the growth velocity is low since the diffusion is slow; i.e. then the growth velocity is dominated by the diffusion process (i.e. truly diffusion controlled) and obeys an Arrhenius-type temperature dependence. At small undercooling, i.e. in the vicinity of the equilibrium phase transformation temperature T_0 (near the solvus line), the growth velocity is low since the supersaturation ΔX_0 is small, i.e. then the temperature dependence of the growth velocity can be governed by the temperature dependence of the solvus lines (for A and B) in the phase diagram. Similar considerations can be applied to the case of ("diffusion controlled") dissolution [26].

4.2.3.3 Effective nature of the activation energy

Kissinger-like methods yield values for *effective* activation energies for (solid state) heterogeneous transformations. These effective activation energies can be conceived as some (see below) combination of the separate activation energies for nucleation, Q_N, and growth, Q_G, provided that the nucleation and growth modes comply with Arrhenius-type temperature dependencies. Then, for a range of nucleation and growth modes, the effective activation energy Q is given by [22]:

$$Q = \frac{(d/m)Q_G + (n - d/m)Q_N}{n}$$
(4.11)

where d is the dimensionality of growth and m is the growth mode parameter [22] ($m = 1$ for interface controlled growth; $m = 2$ for diffusion controlled growth). Whereas the growth exponent n depends on temperature and time (and thus on the transformed fraction f) the activation energies Q_N and Q_G are genuine constants.

Hence, the effective activation energy depends on time (and thus on f) even if iso-kinetics hold. Even recognising that Q is not constant during a phase transformation, Kissinger-like methods can be proposed which allow straightforward determination of kinetic parameters like the growth exponent n, the activation energy for nucleation Q_N and the activation energy for growth Q_G [22, 27].

4.3 Experimental

4.3.1 Specimen preparation

A Ni_3Sn_2 rod (40 at.% Sn, "$Ni_{1.50}Sn$") was prepared by induction heating of high purity Ni sheets (99.98 wt%, Goodfellow) and Sn bars (99.999 wt%, Heraeus) and subsequent casting into a water-cooled copper mould. The alloy was homogenised at 1023 K. Upon water quenching from this temperature the hexagonal high-temperature phase HT-$Ni_{1.50}Sn$ can be preserved. Upon subsequent annealing at 673 K for 120 h the orthorhombic low-temperature phase LT-$Ni_{1.50}Sn$ is produced (for details concerning alloy preparation and heat treatment see [28, 29]). Both modifications differ by the ordering of one type of Ni atoms in the crystal structure [29]: Whereas these Ni atoms are disordered (i.e. do not show long-range ordering) in the HT phase, they are long-range ordered in the LT phase. The equilibrium phase-transformation temperature of the LT $\rightleftarrows$ HT 1st-order transformation is $T_0 \approx 780\,K$.

4.3.2 Differential scanning calorimetry (DSC) measurements

DSC measurements were performed using a Pyris 1 apparatus (Perkin Elmer). The measurements were performed under a protective argon atmosphere (99.99 %; flow rate 30 ml/min). The DSC apparatus was calibrated with respect to temperature and heat flow by measuring the heats of fusion and the melting temperatures of pure In, Pb and Zn. For the DSC measurements the Ni_3Sn_2 rod was crushed into small pieces. For both the sample pan and the reference pan aluminium pans were used. The sample pan was filled with pieces of the crushed rod (sample weight: approx. 40-60 mg). Both the sample pan and the reference pan were sealed with an aluminium lid.

Isochronal DSC anneals up to 873 K were preformed with both the LT and the (quenched) HT specimen, allowing investigation of, respectively, the LT $\rightarrow$ HT trans-

formation close to T_0 and the HT$\rightarrow$LT transformation in the temperature range of 600 K to 645 K, i.e. considerably below T_0. Four different heating rates (5, 10, 20 and 40 K/min) were applied. The temperatures at the transformation-peak maxima, T_M, were determined for the various heating rates.

4.4 Results

4.4.1 The LT$\rightarrow$HT phase transformation, near the LT$\rightleftarrows$HT equilibrium phase-transformation temperature T_0

The isochronal DSC runs of the LT-phase specimens exhibit occurrence of the LT$\rightarrow$HT phase transformation in the vicinity of the equilibrium phase-transformation temperature $T_0 \approx 780\,\mathrm{K}$, in association with an endothermic heat effect (see Figure 4.1). The values of the heating-rate dependent peak maxima T_M have been gathered in Table 4.1.

Table 4.1 The endothermic peak maxima T_M of the LT$\rightarrow$HT equilibrium phase transformation for various heating rates Φ.

heating rate Φ / Kmin^{-1}	5	10	20	40
peak maximum* T_M / K	781.40	781.65	781.90	782.25

* Note that the evaluation by Kissinger(-like) method relies (much more) on the variation of T_M with heating rate than on the absolute values of T_M.

The corresponding "Kissinger plot" exhibits linear behaviour as prescribed by Equation (4.3) (see Figure 4.2). From the straight line fitted to the data shown in Figure 4.2 an activation-energy value was determined (cf. Equation (4.3)): $Q_{\mathrm{LT}\rightarrow\mathrm{HT}} = (12600 \pm 800)$ kJ/mol.

From the area of the peaks the enthalpy difference $\Delta H_{\mathrm{LT}\rightarrow\mathrm{HT}}$ between the LT- and the HT-phase was determined. It was found to be heating-rate independent and its value (referring to one formula unit Ni$_{1.5}$Sn) is $\Delta H_{\mathrm{LT}\rightarrow\mathrm{HT}} = H_{\mathrm{end}} - H_{\mathrm{begin}} = H_{\mathrm{HT}} - H_{\mathrm{LT}}$ $= (2.2 \pm 0.2)\,\mathrm{kJ/mol}$.
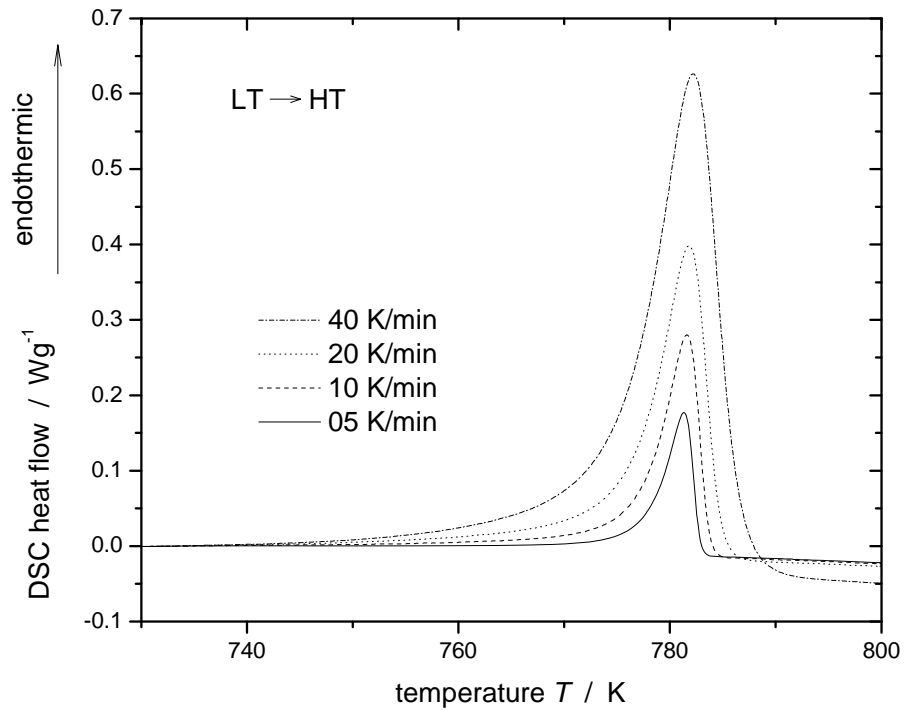
Figure 4.1: Isochronal DSC runs showing the LT→HT phase transformation for the heating rates indicated.
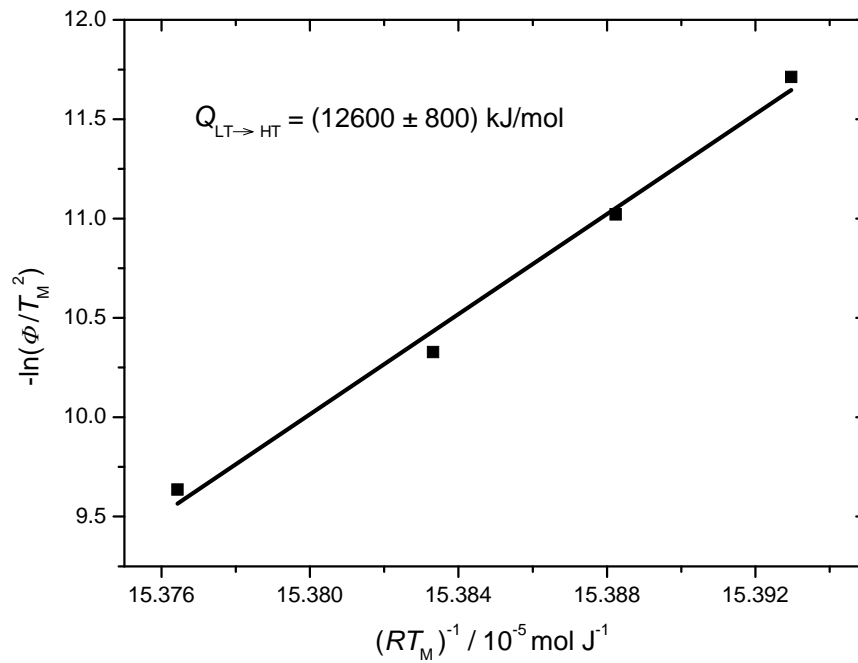
Figure 4.2: "Kissinger plot" for the LT→HT transformation (see data in Table 4.1).

4.4.2 The HT→LT phase transformation, considerably below the LT⇌HT equilibrium phase-transformation temperature T_0

The isochronal DSC runs of the quenched HT-phase specimens show occurrence of the HT→LT phase transformation in the temperature range of 600 K to 645 K ($T_0 \approx 780$ K), in association with an exothermic heat effect (see Figure 4.3).

The peak-maximum temperature T_M shows distinct heating-rate dependence (see Table 4.2). The corresponding "Kissinger plot" exhibits linear behaviour as prescribed by Equation (4.3) (see Figure 4.4). From the straight line fitted to the data shown in Figure 4.4 an activation-energy value was determined (cf. Equation (4.3)):

$Q_{HT \rightarrow LT} = (161 \pm 5)$ kJ/mol.

Table 4.2 The endothermic peak maxima T_M of the LT→HT equilibrium phase transformation for various heating rates Φ.

heating rate Φ / Kmin^{-1}	5	10	20	40
peak maximum* T_M / K	606.65	617.85	630.75	645.25

* Note that the evaluation by Kissinger(-like) method relies (much more) on the variation of T_M with heating rate than on the absolute values of T_M.
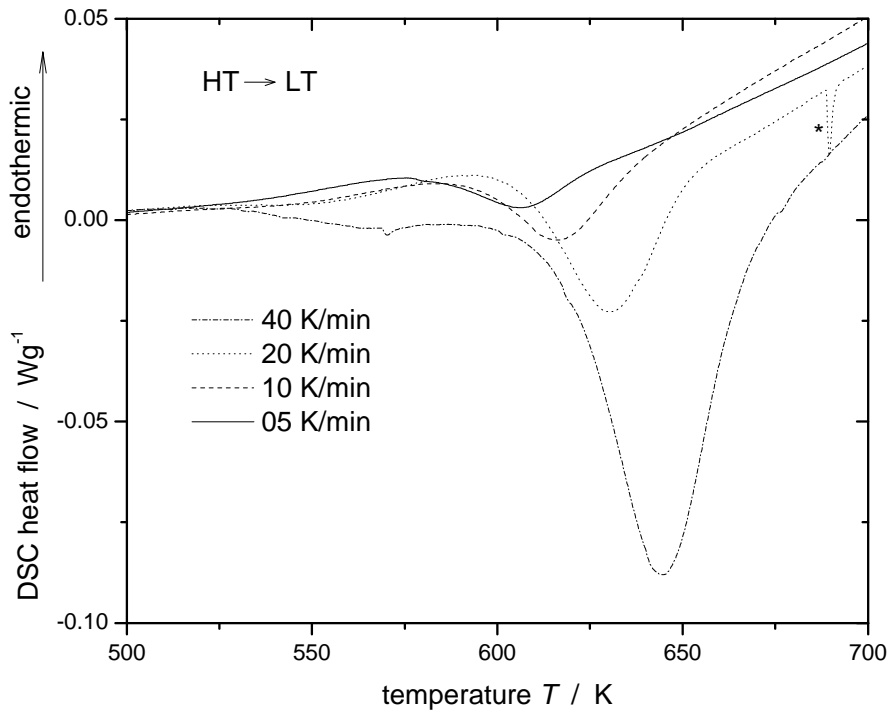
Figure 4.3: Isochronal DSC runs showing the HT $\rightarrow$ LT phase transformation for the heating rates indicated (The asterisk indicates a measurement artefact).
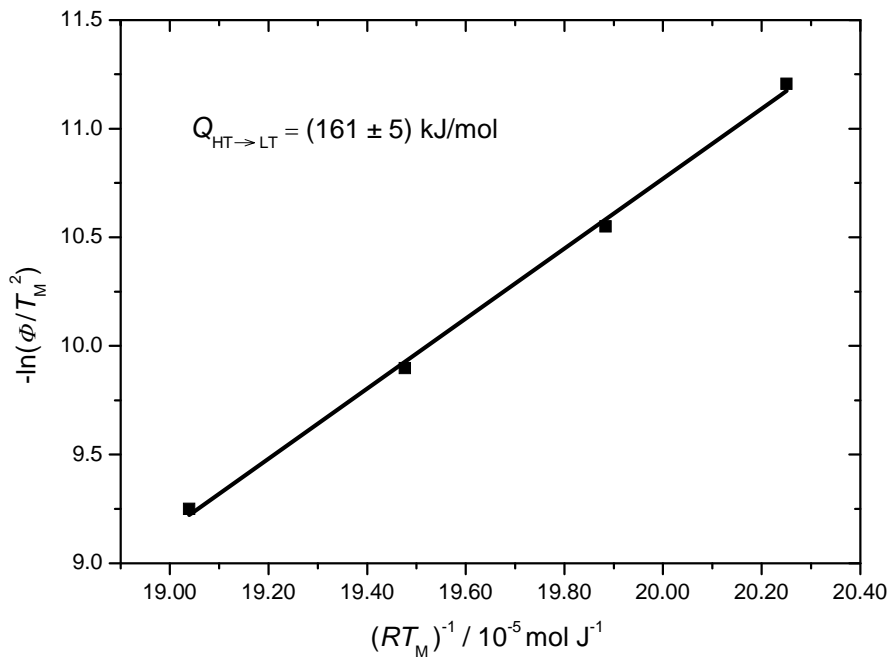
Figure 4.4: Kissinger plot for the HT $\rightarrow$ LT transformation (see data in Table 4.2).

4.5 Discussion

The value obtained in this work for the activation energy of the HT→LT transformation, 161 kJ/mol (see Section 4.2.2), by application of the Kissinger-like method agrees very well with values of 165-170 kJ/mol found for the 1st stage of the HT→LT transformation as obtained from transformation induced lattice-parameter changes as measured in X-ray powder-diffraction patterns [15, 16][1]. As discussed in Refs. [16] and [30], this 1st stage of the HT→LT transformation corresponds to spinodal ordering of the Ni atoms whereas in a 2nd stage coarsening of ordered twin domains occurs; the 2nd stage obviously is associated with a relatively minor heat effect. Thus the DSC signal is predominantly due to the 1st stage of the HT→LT transformation.

The formation of the stable LT phase from the quenched HT phase (i.e. the ordering of (one type of) the Ni atoms) becomes significant for the applied heating rates at about 600 K (see Figure 4.3). This implies that the HT→LT transformation occurs at large undercooling $\Delta T = T_0 - T$. This assures Arrhenius-type temperature dependencies for the phase-transformation kinetics as the thermodynamical driving force generally disappears from (becomes negligible in) the rate expressions (e.g. for nucleation and growth processes, see Section 4.2). Hence application of a Kissinger-like analysis is validated.

The value obtained in this work by application of the Kissinger-like method for the activation energy of the LT→HT phase transformation, $Q_{\mathrm{LT \to HT}} = 12600$ kJ/mol (see Section 4.2.1), is physically unrealistic (i.e. unreasonably high). The activation energy of the LT→HT transformation should be similar to that of the HT→LT transformation, i.e. of the same order of magnitude.

Obviously, at $T < T_0$ the thermodynamic driving force for the LT→HT transformation, $-\Delta G_{\mathrm{LT \to HT}} = -\left(G_{\mathrm{end}} - G_{\mathrm{begin}}\right) = -\left(G_{\mathrm{HT}} - G_{\mathrm{LT}}\right)$, is negative. The activation energy for a (hypothetical) LT→HT transformation equals the activation energy $Q_{\mathrm{HT \to LT}}$ as determined for the HT→LT transformation at $T < T_0$ (cf. Section 4.2.2) *plus* $\Delta H_{\mathrm{LT \to HT}}$ (cf. Section 4.2.1). Thus, the activation energy for the LT→HT transformation should amount $Q_{\mathrm{LT \to HT}} = Q_{\mathrm{HT \to LT}} + \Delta H_{\mathrm{LT \to HT}} \approx 161.0\,\mathrm{kJ/mol} + 2.2\,\mathrm{kJ/mol} \approx 163.2\,\mathrm{kJ/mol}$, i.e. the activation energies for the LT→HT and the HT→LT transformations are similar indeed.

---

[1] The XRPD analyses pertain to *isothermal* treatments of the alloys at various temperatures.

Upon increasing temperature the driving force for the LT→HT transformation becomes less negative and equals zero at $T = T_0$. At this temperature the LT and HT phases coexist and the transformation LT→HT can occur at $T \geq T_0$ with an activation energy similar to that of the HT→LT transformation at $T < T_0$. Evidently, $-\Delta G_{HT \to LT}$ at T well below T_0 is large, whereas $-\Delta G_{LT \to HT}$ above but close to T_0 is small.

The above discussion implies that occurrence of Arrhenius-type temperature dependencies for the transformation kinetics are violated for the LT→HT transformation. Hence, in this case application of the Kissinger-like analysis is not allowed.

For the LT→HT transformation growth of the HT domains in the LT matrix will be interface controlled. For small values of $\Delta G_{LT \to HT}$ it holds $\Delta G_{LT \to HT} = \dfrac{\Delta H_{LT \to HT}}{T_0}(T_0 - T)$ (assuming that $\Delta H_{LT \to HT}$ and $\Delta S_{LT \to HT}$ are practically temperature independent in a (restricted) temperature range around T_0) and it follows from Equation (4.8):

$$v = M_0 \exp\left(-\frac{Q_G}{RT(t)}\right)\left(-\frac{\Delta H}{T_0}(T_0 - T)\right). \qquad (4.12)$$

This result indicates a linear increase of v with T for small $T_0 - T$ and hence no Arrhenius-type temperature dependence (see Figure 4.5). This less distinct, i.e. non-exponential, dependence on temperature for the transformation velocity v also explains the only slight dependence of T_M on Φ (cf. Table 4.1), which facilitates a (seemingly) successful fitting of a straight line in a Kissinger-plot (Figure 4.2). This may have misled previous authors and provides an explanation of very unrealistic activation-energy values published in the corresponding papers [12-14].
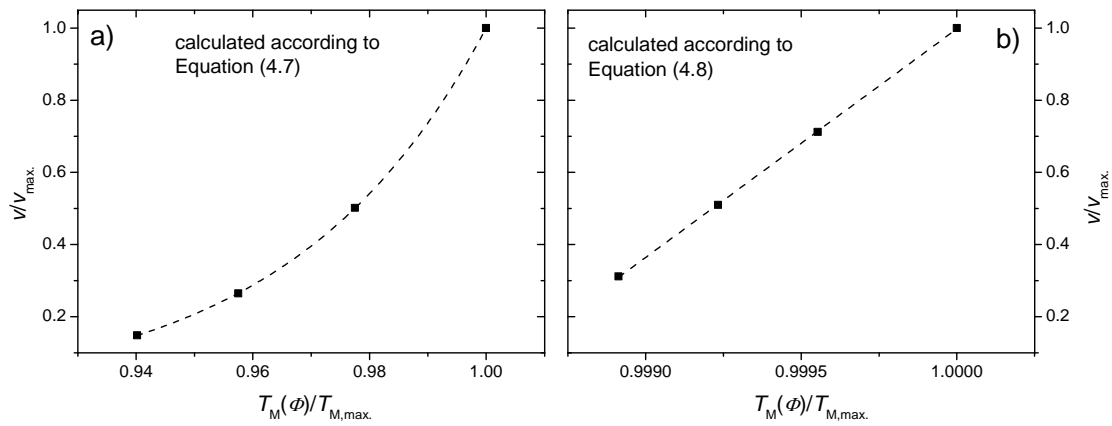
Figure 4.5: Comparison of a) the (normalised) growth velocity according to Equation (4.7) and the data of Table 4.2 (HT→LT phase transformation well below T_0; Arrhenius-type temperature dependence) and (b) the (normalised) growth velocity according to Equation (4.8)/(4.12) and the data of Table 4.1 (LT→HT phase transformation close to T_0; linear temperature dependence). For calculation of the growth velocity the value of the activation energy for the phase transformation of Ni_3Sn_2 was adopted according to Section 4.2.2 and the value of the enthalpy difference ΔH was taken as given in Section 4.2.1.

Yet, a quantitative description of the LT→HT phase-transformation kinetics close to T_0 is still possible, recognising the role of the (temperature dependent) thermodynamic driving force and using a modular model [22] which includes specific prescriptions for the nucleation, growth and impingement modes. One first such modelling was performed by Kempen *et al.* [31] and by Liu *et al.* [32] for the γ (austenite)→α (ferrite) transformation. Such an approach was also possible for the C36⇌C14 phase transformation in the $TiCr_2$ Laves phase [33].

4.6 Conclusions

- Application of Kissinger(-like) methods to determine the activation energy of phase transformations relies on Arrhenius-type temperature dependences for the transformation kinetics (which, for example, incorporate nucleation and growth rates). This implies that the thermodynamic driving force plays a negligible role in the rate expressions. This is generally only the case for phase transformations taking place in temperature ranges remote from the equilibrium phase-transformation temperature T_0.

- Application of Kissinger(-like) methods to phase transformations occurring close to the equilibrium phase-transformation temperature T_0 can lead to (seemingly) linear behaviour in so-called "Kissinger-plots", in association with

slight to moderate dependence of the peak-maximum temperature T_M on heating rate Φ. The values of the "activation energies" thus determined are physically nonsense. On this basis unusual values of "activation energies" thus determined and reported in the literature can be understood.

- Quantitative modelling of phase-transformation kinetics close to the equilibrium phase-transformation temperature T_0 is possible incorporating the thermodynamic driving force in the rate expressions. Full fitting of such models to the experimental kinetic data leads to (also) a value for the activation energy.

4.7 References

[1]   H.E. Kissinger, Variation of peak temperature with heating rate in differential thermal analysis, J. Res. Natl. Bur. Stand. 57 (1956) 217.

[2]   H.E. Kissinger, Reaction kinetics in differential thermal analysis, Anal. Chem. 29 (1957) 1702.

[3]   M.J. Starink, Analysis of aluminium based alloys by catorimetry: quantitative analysis of reactions and reaction kinetics, Int. Mater. Rev. 49 (2004) 191.

[4]   E.J. Mittemeijer, Analysis of the kinetics of phase transformations, J. Mater. Sci. 27 (1992) 3977.

[5]   G.W. Smith, Precipitation kinetics in an air-cooled aluminum alloy: A comparison of scanning and isothermal calorimetry measurement methods, Thermochim. Acta 313 (1998) 27.

[6]   E.J. Mittemeijer, L. Cheng, P.J. van der Schaaf, C.M. Brakman, B.M. Korevaar, Analysis of non-isothermal transformation kinetics-tempering of iron-carbon and iron-nitrogen martensites, Metall. Trans. A 19 (1988) 925.

[7]   P.V. Morra, A.J. Bottger, E.J. Mittemeijer, Decomposition of iron-based martensite. A kinetic analysis by means of differential scanning calorimetry and dilatometry, J. Therm. Anal. Cal. 64 (2001) 905.

[8]   B. Gun, K.J. Laws, M. Ferry, Static and dynamic crystallization in Mg-Cu-Y bulk metallic glass, J. Non-Cryst. Solids 352 (2006) 3887.

[9]   K. Joseph, R.V. Krishnan, K.V.G. Kutty, P.R.V. Rao, Crystallisation kinetics of a cesium iron phosphate glass, Thermochim. Acta 494 (2009) 110.

[10]   W.K. An, A.H. Cai, J.H. Li, Y. Luo, T.L. Li, X. Xiong, Y. Liu, Y. Pan, Glass formation and non-isothermal crystallization of $Zr_{62.5}Al_{12.1}Cu_{7.95}Ni_{17.45}$ bulk metallic glass, J. Non-Cryst. Solids 355 (2009) 1703.

[11]   H. Nitsche, F. Sommer, E.J. Mittemeijer, The Al nano-crystallization process in amorphous $Al_{85}Ni_8Y_5Co_2$, J. Non-Cryst. Solids 351 (2005) 3760.

[12]   T. Hashimoto, Y. Ueda, M. Yoshinaga, K. Komazaki, K. Asaoka, S.R. Wang, Observation of two kinds of structural phase transitions in the $Ba_2In_2O_5$ system, J. Electrochem. Soc. 149 (2002) 1381.

[13]   A.A. van Dooren, B.W. Müller, Effects of experimental variables on the determination of kinetic parameters with differential scanning calorimetry I. Calculation procedures of Ozawa and Kissinger, Thermochim. Acta 65 (1983) 257.

[14]   V.T. Popa, Apparent kinetics of ice melting revealed by DSC endotherms, Rev. Roum. Chim. 48 (2003) 987.

[15]   A. Leineweber, E.J. Mittemeijer, M. Knapp, C. Baehtz, Kinetics of ordering in $Ni_{1.50}Sn$ (Ni_3Sn_2) as revealed by the variation of the lattice parameters upon annealing, Phil. Mag. 87 (2007) 1821.

[16]   A. Leineweber, E.J. Mittemeijer, The use of lattice-parameter changes to trace the kinetics of phase transformations; powder-diffraction analysis of disorder-order transformations in $Ni_{1+\delta}Sn$, Z. Kristallogr. 222 (2007) 150.

[17]   H. Fjellvag, A. Kjekshus, Structural-properties of Co_3Sn_2, Ni_3Sn_2 and some ternary derivatives, Acta Chem. Scand. A 40 (1986) 23.

[18]   C. Schmetterer, H. Flandorfer, K.W. Richter, U. Saeed, M. Kauffman, P. Roussel, H. Ipser, A new investigation of the system Ni-Sn, Intermetallics 15 (2007) 869.

[19]   S. Vyazovkin, D. Dollimore, Linear and nonlinear procedures in isoconversional computations of the activation energy of nonisothermal reactions in solids, J. Chem. Inf. Comput. Sci. 36 (1996) 42.

[20]   M.J. Starink, The determination of activation energy from linear heating rate experiments: a comparison of the accuracy of isoconversion methods, Thermochim. Acta 404 (2003) 163.

[21]   M.J. Starink, Activation energy determination for linear heating experiments: Deviations due to neglecting the low temperature end of the temperature integral, J. Mater. Sci. 42 (2007) 483.

[22]   F. Liu, F. Sommer, C. Bos, E.J. Mittemeijer, Analysis of solid state phase transformation kinetics: Models and recipes, Int. Mater. Rev. 52 (2007) 193.

[23]   J.W. Christian, The theory of transformations in metals and alloys, Oxford: Pergamon Press, 1965.

[24]   D.A. Porter, K.E. Easterling, Phase transformations in metals and alloys, New York: Van Nostrand Reinhold Company, 1981.

[25]   C. Zener, Theory of growth of spherical precipitates from solid solution, J. Appl. Phys. 20 (1949) 950.

[26]   H.B. Aaron, Fainstei.D, G.R. Kotler, Difussion-limited phase transformations - a comparison and critical evaluation of mathematical approximations, J. Appl. Phys. 41 (1970) 4404.

[27]   F. Liu, S.J. Song, F. Sommer, E.J. Mittemeijer, Evaluation of the maximum transformation rate for analyzing solid-state phase transformation kinetics, Acta Mater. 57 (2009) 6176.

[28]   A. Leineweber, M. Ellner, E.J. Mittemeijer, A NiAs/Ni_2In-type phase Ni_{1+x}Sn (x = 0.35<x<0.45) with incommensurate occupational ordering of Ni, J. Solid State Chem. 159 (2001) 191.

[29]   A. Leineweber, Variation of the crystal structures of incommensurate LT´-$Ni_{1+\delta}$Sn (δ = 0.35, 0.38, 0.41) and commensurate LT-Ni1+dSn (δ = 0.47, 0.50) with composition and annealing temperature, J. Solid State Chem. 177 (2004) 1197.

[30]   A. Leineweber, E.J. Mittemeijer, The evaluation of the kinetics of ordering processes in $Ni_{1+\delta}$Sn (δ = 0.35, 0.50) by X-ray powder diffraction, Z. Kristallogr. Suppl. 23 (2006) 351.

[31]   A.T.W. Kempen, F. Sommer, E.J. Mittemeijer, The kinetics of the austenite-ferrite phase transformation of Fe-Mn: differential thermal analysis during cooling, Acta Mater. 50 (2002) 3545.

[32]   Y.C. Liu, F. Sommer, E.J. Mittemeijer, Abnormal austenite-ferrite transformation behaviour of pure iron, Phil. Mag. 84 (2004) 1853.

[33]   W. Baumann, A. Leineweber, E.J. Mittemeijer, The kinetics of a polytypic Laves phase-transformation in $TiCr_2$, as submitted for publication (2010).

Chapter 5

The kinetics of a polytypic Laves-phase transformation in TiCr$_2$

Wolfgang Baumann, Andreas Leineweber and Eric Jan Mittemeijer

Abstract

A systematic investigation of the kinetics of the polytypic C36 $\rightleftarrows$ C14 equilibrium phase (shear) transformation occurring at about 1545 K was performed. A recently developed calibration and desmearing procedure for a differential thermal analysis (DTA) apparatus [Baumann *et al*. Thermochim. Acta 472 (2008) 50] enabled the investigation of the progress of this solid-solid phase transformation in the high-temperature region by isochronal DTA measurements, both upon heating and cooling. A kinetic model was developed on basis of *the modular approach*, which considers three overlapping mechanisms (nucleation, growth and impingement). It was shown that athermal nucleation prevailed, i.e. pre-existing nuclei (here: arrays of dislocations) become activated as function of undercooling/overheating. The model fitting led to values for the equilibrium phase-transformation temperature, the C36/C14 interface energy and the activation energy for growth. Moreover, a quantitative explanation was given of the composition-dependent thermal hysteresis of the phase transformation.

5.1 Introduction

Laves phases constitute the largest group of intermetallic compounds [1, 2]. Especially in the last decades the scientific interest in Laves phases has strongly increased in view of their possible application as high-temperature/high-strength or functional (super-conducting, magnetic and hydrogen-storage) materials [3, 4]. Accordingly, knowledge on polytypic Laves phase transformations is desired as a means for tuning such proper-ties.

5.1.1 Crystal structure of Laves phases

Laves phases have the general formula AB_2, with the metallic A atom being (ideally) $(3/2)^{1/2} \approx 1.225$ times larger than the metallic B atom. For the purpose of this work it is convenient to describe the structure of the different Laves-phase modifications in terms of stacking sequences of alternate layer-sandwich units AB_3A (this notation re-fers to the composition of this stacking unit; see Figure 5.1) and single-layers consist-ing of B atoms (see Figure 5.1). These layers can be placed in three different lateral positions. These positions for the single-layers (of B atoms) are denoted by the lower-case letters x, y and z and for the layer-sandwich units, AB_3A, the upper-case letters X, Y and Z are used (see Figure 5.1).

The central layer of the layer-sandwich unit is shown in Figure 5.1 (left side); it forms a Kagomé net consisting of B atoms at the position, say, X (given by the posi-tion of the holes/compare Figure 5.1). The bigger A atoms are placed just above and below the Kagomé net on the holes (position X) to build up the layer-sandwich unit (see Figure 5.1/right side). A single-layer of B atoms could now be placed in two dif-ferent ways onto the layer-sandwich unit; i.e. a triangular net of B atoms can be placed either on the z or y positions of the layer-sandwich unit at position X (see Figure 5.1). The layer-stacking sequence of a Laves phase can then be represented by an alternate sequence of these upper- and lower-case letters (see Figure 5.2 top left). The following rules apply:

(i) Taking first only into account the upper-case letters, a given letter, say X, may only be followed by a different other upper-case letter, in this case Y or Z, i.e. an X cannot be followed by an X (Y not by Y; Z not by Z).

(ii) A single-layer unit located between two layer-sandwich units is represented by a lower-case letter different from the upper-case letters representing the adjacent layer-sandwich units. Consequently, a z-type single layer is located between X and Y, i.e. the corresponding part of the stacking sequence reads ...XzY... or ...YzX....
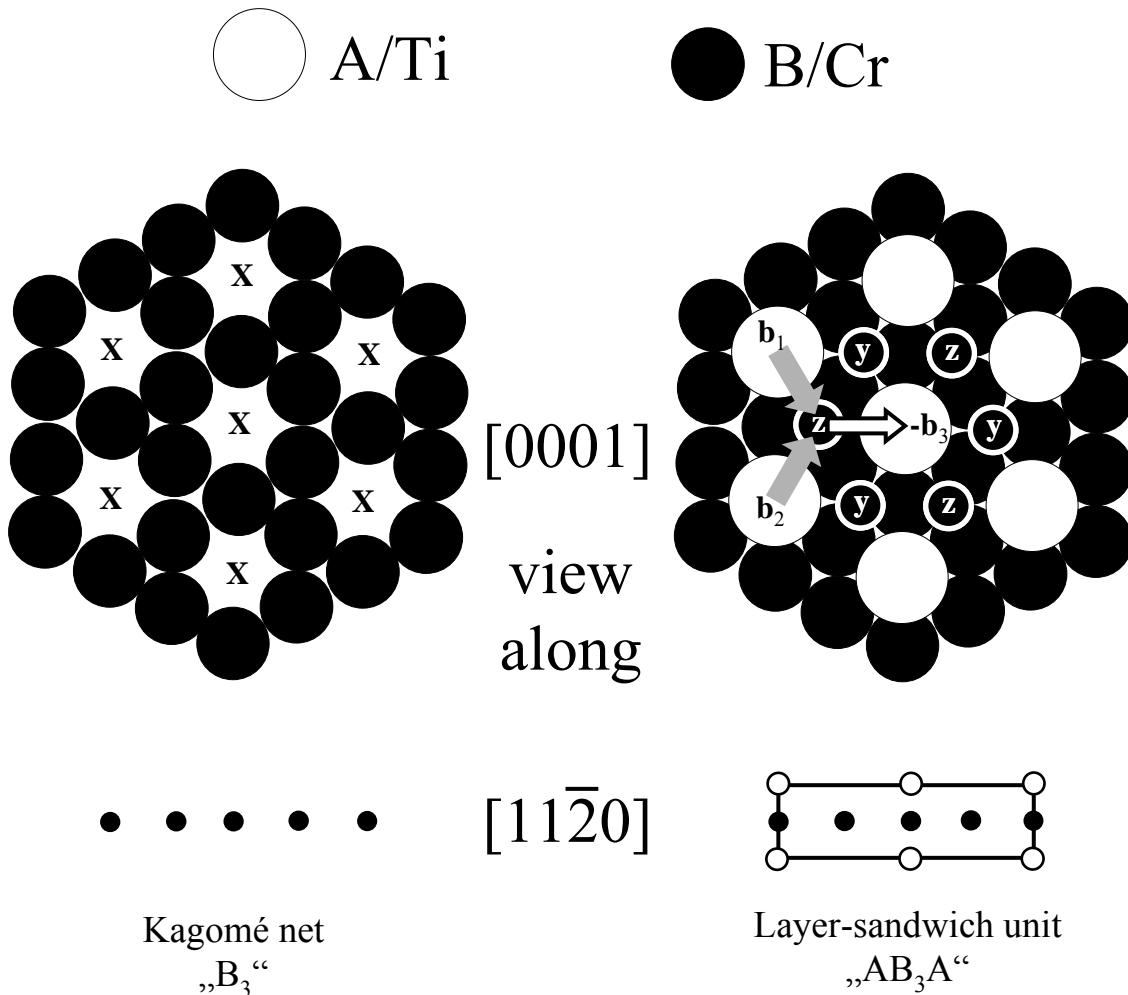
Figure 5.1: Construction of the layer-sandwich unit. Left: Kagomé net consisting of B atoms. Right: Layer-sandwich unit. The viewing directions along different crystallographic directions have been indicated. The grey arrows indicate possible Burgers vectors ($\mathbf{b}_1$ and $\mathbf{b}_2$) of two Shockley-partial dislocations which comprise one synchro-Shockley partial dislocation with the overall Burgers vector $-\mathbf{b}_3 = \mathbf{b}_1 + \mathbf{b}_2$ [5].

Since the position of the single-layer units is defined/prescribed by the lateral positions of the adjacent layer-sandwich unit layers it suffices to use only the upper-case letters to describe the different stacking sequences. The three most prominent Laves-phase polytypes are: the cubic MgCu$_2$ type (C15; stacking sequence XYZ), the dihexagonal MgNi$_2$ type (C36; stacking sequence XYXZ) and the hexagonal MgZn$_2$ type (C14;

stacking sequence XY). The stacking sequences of the Laves phases considered in this work (C36 and C14) are shown in Figure 5.2.
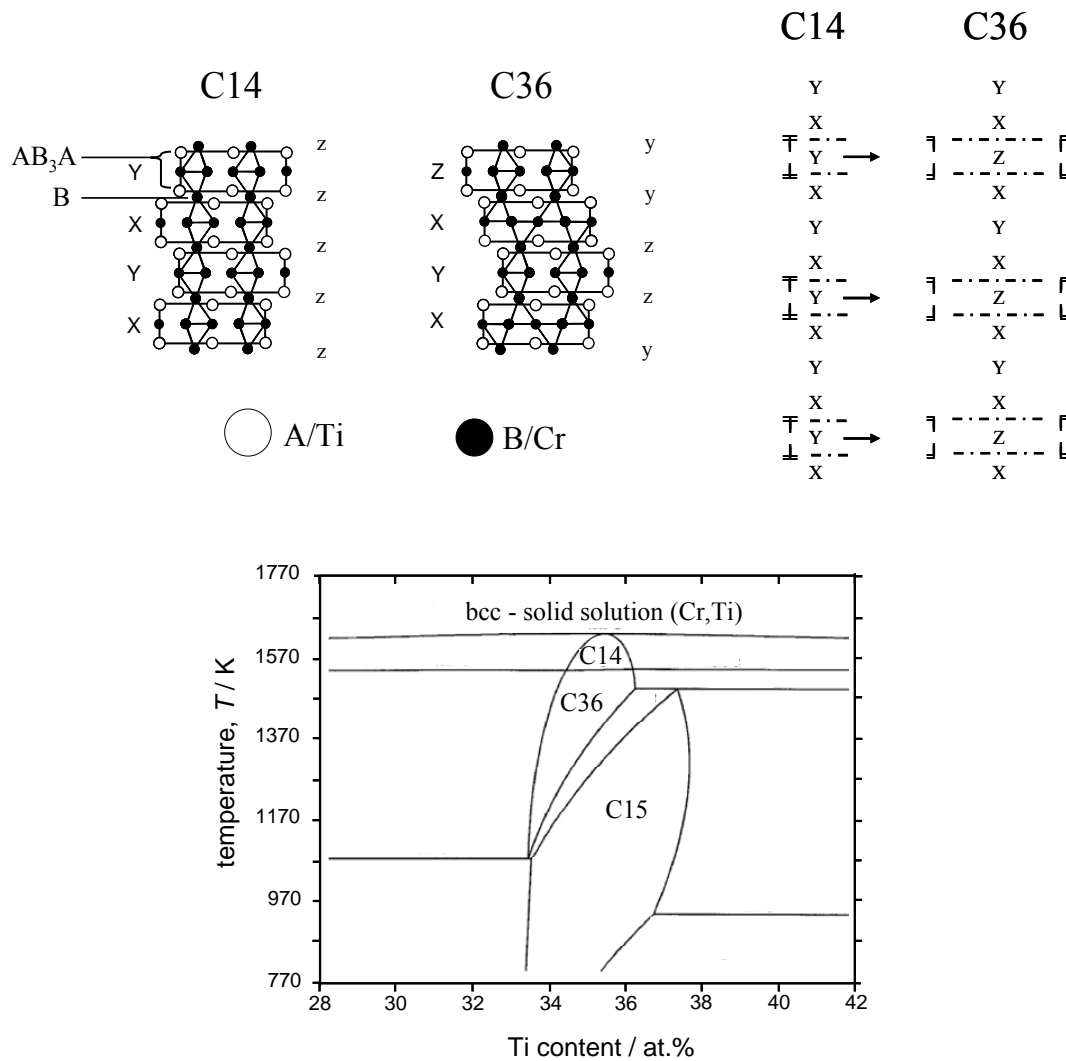
Figure 5.2: Top left: Structure and corresponding stacking sequence of the C14 and the C36 Laves phases. Top right: Ordered arrays of synchro-Shockley partial dislocation dipoles (a dipole encloses every fourth layer-sandwich unit) gliding through a C14 crystal leaving behind the C36 structure (see also Figure 5.3). Bottom: Partial Ti-Cr phase diagram [6, 7]; Laves-phase containing composition range. Note that the extremely narrow two-phase region between the C36 and C14 single phase regions has been indicated by a single line.

The structurally different Laves-phase modifications (i.e. C15, C36 and C14) often coexist in binary systems as a function of composition (e.g. $NbCo_2/ZrFe_2$) or temperature (e.g. $TiCr_2/NbCr_2/HfCr_2$) [1, 8]. The only temperature-dependent Laves-phase transformations in the absence of compositional change (i.e. in the absence of long range diffusion) are thought to occur by a coupled double shear or synchroshear process, cf. Section 5.1.2.

5.1.2 Synchroshear

The idea of synchroshear as mechanism for polytypic Laves-phase transformations stems from geometrical considerations and was firstly proposed in connection with basal slip and twinning of sapphire [9]. Allen *et al.* [10] originally proposed the concept of synchroshear as mechanism for phase transformations in Laves phases. Chisholm *et al.* found some indirect experimental evidence that synchroshear occurs in Laves phases [11]. One main idea is that the layer-stacking sequences, considering only the layer-sandwich units, are shifted by glide of partial dislocations, with six different Burgers vectors $\pm\mathbf{b}_1 = \pm\frac{1}{3}\left[01\overline{1}0\right]$, $\pm\mathbf{b}_2 = \pm\frac{1}{3}\left[\overline{1}010\right]$, and $\pm\mathbf{b}_2 = \pm\frac{1}{3}\left[1\overline{1}00\right]$ (cf. Figure 5.1; employing Miller-Bravais indices for hexagonal crystal-structure lattices), along the basal (0001) plane between two (assumedly rigid) *layer-sandwich units*. Thereby, the relative position of the layer-sandwich unit, say, "above" the (0001) glide plane becomes changed with respect to that of the layer-sandwich unit "below" the (0001) glide plane. Note that, as consequence of stacking rule (ii) indicated above, this glide process requires that the *single-layer unit* between the two *layer-sandwich units* has to move synchronously, also by glide of such a partial dislocation, in another direction, but also within the glide plane. Thus the shear process, indicated conventionally with one of the above-mentioned Burgers vectors for the partial dislocation realising glide of the layer-sandwich unit, is actually a synchroshear process [5, 11, 12]. The corresponding pair of *partial* dislocations is, therefore, called synchro-Shockley partial dislocation [11].

5.1.3 C36 $\rightleftarrows$ C14 phase transformation

The C36 $\rightleftarrows$ C14 phase transformation can be established by glide of synchro-Shockley partial dislocation *dipoles* (see Figure 5.2 top right) [13]. This hypothesis could be confirmed recently by high-resolution transmission electron microscopy investigations in combination with X-ray powder diffraction [14, 15]. These dislocation dipoles must move in ordered arrays through the crystal. The synchro-Shockley dislocation dipoles consist of two single synchro-Shockley partial dislocations of opposite Burgers vectors (e.g. $\mathbf{b}_1$ and $-\mathbf{b}_1$) which propagate above and below such a layer-sandwich unit. A set of periodically arranged synchro-Shockley dislocation dipoles can thus perform the C36 $\rightleftarrows$ C14 transformation, without that macroscopic shear occurs [14]. The motion of one synchro-Shockley dislocation dipole thus transforms a region of the crystal com-

prising four layer-sandwich units (i.e. XYXY $\rightarrow$ XYXZ; see Figure 5.2). Hence, m dislocation dipoles, such ordered that a dipole encloses every fourth layer-sandwich unit, transform a region of the parent crystal comprising $n = 4m$ layer-sandwich units.

The C36 $\rightleftarrows$ C14 first-order phase transformation takes place upon heating and cooling by passing an extremely narrow two-phase region (indicated by a single line in Figure 5.2). During isochronal heating/cooling the two-phase region is passed extremely fast. Thus one can assume that the transformation takes place partitionless upon passing the so-called "T_0 line" at which both phases of same composition are in thermodynamic equilibrium (here only the chemical, bulk Gibbs energy is considered (cf. Figure 5.4 and its discussion in Section 5.2)) [16].

5.2 Phase-transformation kinetics

The progress of a solid-state phase transformation can be traced by measuring a physical property of a material. Such measurements disclose the transformed fraction $f(t)$ as a function of time t. Generally a modular phase-transformation model that includes the three overlapping mechanisms, nucleation, growth and impingement, can be used to describe the progress of a phase transformation. In this *modular approach* each mechanism can be modelled separately [17, 18].

Assuming, hypothetically, that each individual product *particle*, emanating from a successful nucleation process, grows into an infinitely large parent phase, in the absence of other product particles, the so-called extended volume, V_e, given by the sum of the volumes of all these (hypothetical) particles, can be calculated. In a second step the extended transformed fraction, x_e ($= V_e/V_S$; with V_S as the volume of the specimen), has to be corrected for (*hard*) *impingement* to obtain the *real* transformed fraction, f, by adopting a certain impingement mode.

Within the above context, the following considerations are primarily made in view of their possible use to model the C36 $\rightleftarrows$ C14 Laves-phase transformation kinetics upon isochronal heating/cooling, i.e. with constant heating/cooling rates, Φ, implying that the temperature is a linear function of time, i.e. $T(t) = T_S + \Phi t$ with $T_S = T(t = 0)$ and $\Phi = dT(t)/dt$.

5.2.1 Nucleation

The thermodynamic model for nucleation must be compatible with the mechanism for the C36 $\rightleftarrows$ C14 transformation by glide of an ordered array of synchro-Shockley partial dislocation dipoles (cf. Sections 5.1.2 and 5.1.3). The model presented here is derived from an earlier description of nucleation of the martensitic fcc $\rightarrow$ hcp transformation in metals by dissociation of perfect dislocations [19].

Consider the periodically arranged array of m dipoles of *perfect* synchro dislocations in a C36 crystal as shown in Figure 5.3 (see also Figure 5.2). The C36 $\rightarrow$ C14 phase transformation is performed by the slip/glide of periodically arranged synchro-Shockley *partial* dislocation dipoles through the crystal lattice (see Section 5.1.3).
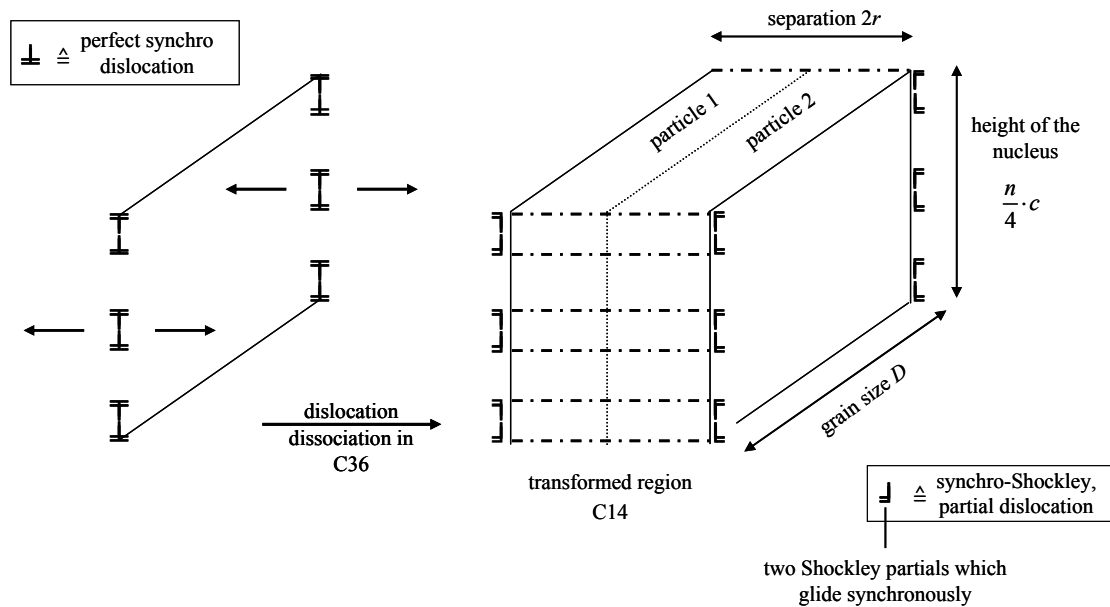
Figure 5.3: Schematic view of a C14 nucleus developing in a C36 matrix originating from dissociation of three perfect synchro dislocation dipoles. Left: Array of three perfect synchro dislocation dipoles in the C36 Laves phase (before dissociation); right: two arrays each consisting of three synchro-Shockley partial dislocation dipoles; the two arrays build up two *particles* consisting of the C14 phase, each particle having a volume determined by the grain size D, the height of the defect structure (depending on the number of synchro-Shockley partial dislocation dipoles within the array) and half of the separation distance, $2r$, realised by glide of the pairs of synchro-Shockley partial dislocation dipoles.

Initiation of a C36 $\rightarrow$ C14 transformation requires dissociation of the array of perfect synchro dislocation dipoles into two arrays of synchro-Shockley partial dislocation dipoles. The region in between these two arrays can be described as a stacking faulted region (with reference to the parent structure) or as transformed region (exhibiting the product, C14 crystal structure). As long as C36 is the stable phase, the dissociation is limited by the high energy (with reference to the parent phase) of the faulted structure lying between the two arrays of synchro-Shockley partial dislocation dipoles. This is

no longer the case if the C14 phase becomes the stable phase, i.e. by passing the "T_0 line" (see above) upon (isochronal) heating from the C36 phase field.

The region between the two separated arrays of synchro-Shockley partial dislocation dipoles can be considered as two second-phase (C14) particles each having the volume V and the interfacial area S. The total Gibbs energy change ΔG associated with the formation of this second phase particle can be given as:

$$\Delta G = V\left(\Delta G_V^{ch} + E_V^{str}\right) + S\sigma, \tag{5.1}$$

where ΔG_V^{ch} $(= \Delta G_m^{ch}/V_m$; ΔG_m^{ch} is the chemical Gibbs energy difference per mole of atoms between product phase and parent phase and V_m is the molar volume) is the chemical Gibbs energy difference between product phase and parent phase per unit volume, E_V^{str} is the elastic strain energy per unit volume and σ is the particle/matrix interface energy per unit area. For small overheating/undercooling, i.e. in the vicinity of the equilibrium phase-transformation temperature T_0, the chemical Gibbs-energy change per mole of atoms ΔG_m^{ch} can be approximately given as:

$$\Delta G_m^{ch} = \frac{\Delta H_{tot}}{T_0}\left(T_0 - T\right), \tag{5.2}$$

where ΔH_{tot} is the transformation enthalpy. This enthalpy is positive for endothermic reactions, i.e. for the C36$\rightarrow$C14 transformation occurring upon heating, and negative for exothermic reactions i.e. for the C14$\rightarrow$C36 transformation occurring upon cooling. The elastic strain energy per unit volume, E_V^{str}, can be neglected since the product and the parent phases have similar molar volumes [20-22].

The volume of a product-phase particle is given by

$$V = \frac{n}{4}crD, \tag{5.3}$$

with $nc/4$ as the height/size of the nucleus; $n/4$ is the number of synchro dislocation dipoles within the array of dipoles oriented perpendicular to the stacking direction (cf. Figures 5.2 and 5.3); n is the number of layer-sandwich units in the stack considered and c is the distance between adjacent synchro (-Shockley partial) dislocation dipoles in the dipole array parallel to the c-axis; $c = c_{C36} = 2c_{C14}$); $2r$ is the separation distance of the partial dislocations (r is the distance passed by one array of synchro-Shockley partial dislocation dipoles) and D is the grain size of the parent crystal (compare Figure 5.3).

The newly created interfacial area S of one particle is given by the top and the bottom side and the front and the rear side of the product-phase particle (as shown in Figure 5.3). Because $D \gg nc/4$ the interfacial area S is approximately given by the top and bottom sides and thus:

$$S \approx 2rD \tag{5.4}$$

It follows from Equations (5.1), (5.3) and (5.4):

$$\Delta G_A \equiv \frac{\Delta G}{rD} = n \frac{c}{4V_m} \Delta G_m^{ch} + 2\sigma . \tag{5.5}$$

The term $\dfrac{\Delta G}{rD}$ corresponds to the energy difference between the product phase/particle and parent phase per unit area top/bottom interface, ΔG_A. Note that both the volume chemical energy term as well as the interface energy term scale with r.

Evidently, a critical size (a critical value of r) does not occur (cf. Equation (5.5): The transformation can take place "spontaneously", i.e. without overcoming an energy barrier by thermal activation, provided that the energy difference between the product phase (lying in-between the dissociated dislocation arrays) and parent phase per unit area, ΔG_A, becomes negative, e.g. by a change of temperature (cf. Equations (5.2) and (5.5); see Figure 5.4). Hence, the product-phase particles develop by athermal nucleation.

The interfacial term 2σ in Equation (5.5) is independent of the height $nc/4$ of the possibly operating dislocation-dipole array, whereas the chemical Gibbs energy change for operation of the same dislocation dipole array $\left(= nc\Delta G_m^{ch}/4V_m\right)$ increases with n. For a fixed value of n the energy difference per unit area top/bottom interface, ΔG_A, equals zero at a finite value of overheating, $\Delta T = T_0 - T$, for the C36$\rightarrow$C14 transformation (see Figure 5.4; or rather undercooling, $\Delta T = T_0 - T$, for the C14$\rightarrow$C36 transformation). A distribution of heights of the arrays of dislocation dipoles (corresponding with a varying number of layer-sandwich units n in the arrays) is supposed to exist in the C36 crystal. The larger the height of the dislocation array, i.e. the larger n, the lower the required overheating in order that this dislocation dipole array starts to produce by glide a product-phase (C14) particle (see Figure 5.4). In other words, the nucleation event can be described as a kind of site saturation at each temperature, where dislocation dipole arrays of specific height start to operate.
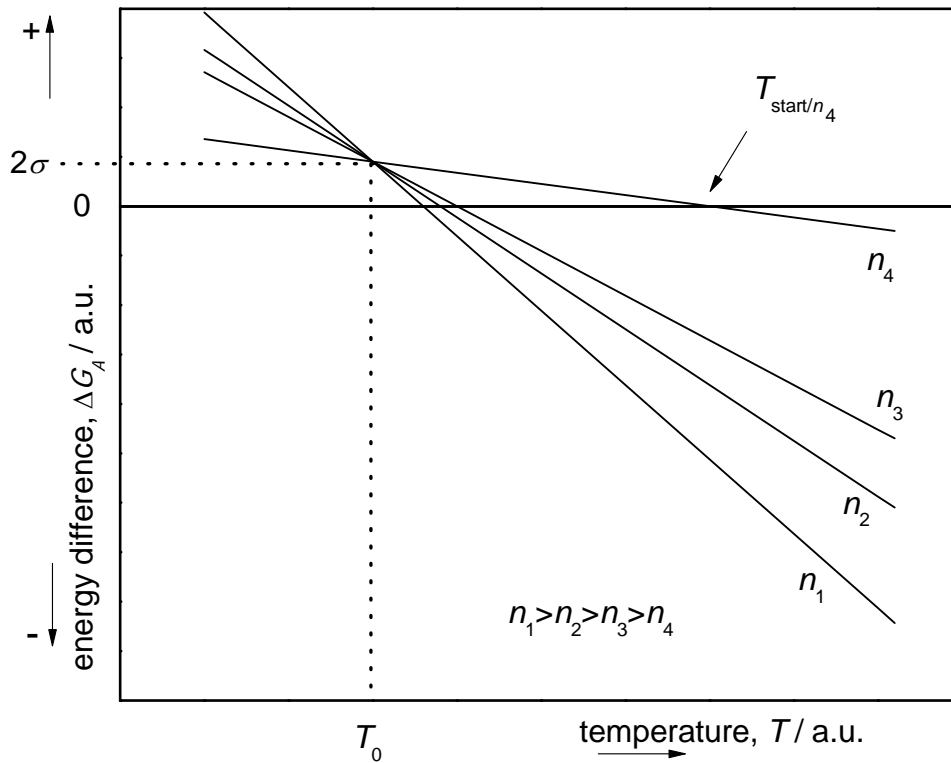
Figure 5.4: Schematic view of the energy difference between the product phase particle (C14) and parent phase (C36) per unit area top/bottom interface, ΔG_A, as function of temperature for different particle heights n (cf. Figure 5.3); as determined by Equations (5.2) and (5.5). At T_0 the chemical Gibbs energy change, ΔG_m^{ch}, is zero and the energy difference ΔG_A is given by the interfacial energy term 2σ. A viable product particle can occur (and grow) when the energy difference ΔG_A becomes negative. It follows from Equation (5.5) that the larger the height n of the dislocation dipole array, the lower is the necessary overheating. The temperature T_{start/n_4} indicates the temperature where a dipole array of height n_4 can start to produce by glide a product-phase particle.

At a given overheating, $\Delta T(t) = (T_0 - T(t))$, the critical value of n, indicating the minimal height of the dislocation-dipole array for realising by glide the C36 $\rightarrow$ C14 transformation, satisfies (see Equations (5.2) and (5.5)):

$$n^*\big(\Delta T(t)\big) = -\frac{2\sigma}{\dfrac{c}{4V_m}\big(\Delta G_m^{ch}\big)} = -\frac{2\sigma}{\dfrac{c}{4V_m}\left(\dfrac{\Delta H_{\mathrm{tot}}}{T_0}(T_0 - T)\right)}. \qquad (5.6)$$

Upon increasing temperature more and more dislocation-dipole arrays of decreasing height can become active. From experimental data for the martensitic transformation (driven by the dissociation of *normal* Shockley partials) in Fe 30.2 wt% Ni, it was proposed that the cumulative number of operating dislocation-dipole arrays, $N\big(n^*(\Delta T(t))\big)$, obeys the empirical function [23]:

$$N\left(n^*\left(\Delta T(t)\right)\right) = N_{\text{tot}} \exp\left(-n^*\left(\Delta T(t)\right)\right) \tag{5.7}$$

with N_{tot} as the total number of pre-existing synchro-Shockley partial dislocation-dipole arrays of variable height. The above treatment focussed on the C36→C14 transformation occurring upon heating. A parallel treatment holds for the C14→C36 transformation occurring upon cooling.

5.2.2 Interface-controlled growth

When an ordered array of synchro-Shockley partial dislocation dipoles glides through the crystal (as shown in Figure 5.2 (top right) and Figure 5.3) the product-phase particle grows. The dimensionality of the growth is one, i.e. the product-phase particle grows in one of the three possible $<0\overline{1}10>$ directions oriented perpendicular to the c-axis (cf. Figure 5.1). There is no composition change from parent to product phase in a polytypic phase transformation and thus the growth is controlled by atomic (jump) processes in the direct vicinity of the interface: Interface-controlled growth.

The height of a product phase particle which starts to grow at time τ is given by $n^*\left(\Delta T(\tau)\right)c/4$ (cf. Figure 5.3). Hence, at time t the volume $Y(\tau,t)$ of a product-phase particle, which starts to grow at time τ, is given by (see Figure 5.3, Equations (5.3) and (5.6))

$$Y(\tau,t) = D\frac{n^*\left(\Delta T(\tau)\right)}{4}cr\left(T(t)\right) = D\frac{n^*\left(\Delta T(\tau)\right)}{4}c\int_\tau^t v\,\mathrm{d}t \tag{5.8}$$

with v as the interface/synchro-Shockley partial dislocation-glide velocity. For small undercooling or overheating the growth velocity v is given by

$$v\left(T(t)\right) = M\left(-\Delta G_m\left(T(t)\right)\right) = M_0 \exp\left(-\frac{Q}{RT(t)}\right)\left(-\Delta G_m\left(T(t)\right)\right), \tag{5.9}$$

where M is the temperature dependent interface mobility, M_0 is the pre-exponential factor for growth and Q denotes the activation energy for growth. The net driving force $-\Delta G_m\left(T(t)\right)$ which is given as a molar quantity [18] amounts to (cf. Equations (5.1) and (5.5)):

$$-\Delta G_m\left(T(t)\right) = -\frac{\Delta G}{rDn^*\left(\Delta T(\tau)\right)\dfrac{c}{4V_m}} = -\Delta G_m^{ch}\left(T(t)\right) - \frac{2\sigma}{n^*\left(\Delta T(\tau)\right)\dfrac{c}{4V_m}} \tag{5.10}$$

It is supposed that dislocation glide is rate controlled by moving kink pairs along the dislocation line. This generally holds for materials with mixed metallic-covalent-ionic bonding type [1, 24]. Thus the activation energy Q for growth (in Equation (5.9)) is given by the activation-energy barrier for kink motion [24].

5.2.3 Numerical calculation of the extended transformed fraction

For the calculation of the time evolution of the extended transformed fraction x_e (cf. begin of Section 5.2) the time span is divided into constant time steps Δt. The simulation starts at $t = 0$ where the number of operative synchro-Shockley partial dislocation dipole arrays is $N_0\left(n^*\left(\Delta T\left(t_0\right)\right)\right) = 0$, i.e. no transformation. During the first time/temperature step ($i = 1$; $i =$ number of time steps) the number of operative synchro-Shockley partial dislocation-dipole arrays increases to $N_1\left(n^*\left(\Delta T\left(t_1\right)\right)\right)$. This means that during the first time step the number of synchro-Shockley partial dislocation-dipole arrays, which become operative, ΔN_1, is given by $\Delta N_1 = N_1\left(n^*\left(\Delta T\left(t_1\right)\right)\right) - N_0\left(n^*\left(\Delta T\left(t_0\right)\right)\right)$. The number of nuclei which become operative during the ith-time step is thus given by $\Delta N_i = N_i\left(n^*\left(\Delta T\left(t_i\right)\right)\right) - N_{i-1}\left(n^*\left(\Delta T\left(t_{i-1}\right)\right)\right)$. The nuclei ΔN_i which become operative during the time step i are able to grow starting at time $\tau_i = (i+1)\Delta t$. Accordingly, the extended transformed fraction x_e reads:

$$x_{e,i} = \sum_{j=0}^{i-1} \Delta N_j Y_{i-j} \tag{5.11}$$

where Y is given by Equation (5.8).

5.2.4 Impingement; anisotropic growth

Adopting an appropriate impingement mode the *real* transformed fraction $f_{\text{model}}\left(T\left(t\right)\right)$ can be calculated from the extended transformed fraction x_e. In the case of anisotropic growth, which pertains to the polytypic phase transformation considered here (one-dimensional growth; cf. Section 5.2.2), the (hard) impingement process can be phenomenologically described by the following impingement correction [18]:

$$\frac{\mathrm{d}f}{\mathrm{d}x_e} = (1-f)^\xi \tag{5.12}$$

where ξ is a measure for the degree of anisotropic impingement. Integration of Equation (5.12) for the case $\xi > 1$ yields:

$$f_{\mathrm{model}}(T(t)) = 1 - \left[1 + (\xi-1)x_e\right]^{-\frac{1}{\xi-1}} \tag{5.13}$$

5.3 Experimental procedure and data evaluation

5.3.1 Specimen preparation and characterisation

Three TiCr$_2$ alloys (alloy I 33.7 at.% Ti/66.3 at.% Cr; alloy II 34.3 at.% Ti/65.7 at.% Cr; alloy III 35.5 at.% Ti/64.5 at.% Cr; as determined by electron-probe microanalysis – EPMA; cf. Section 5.4.1), were prepared by arc melting high-purity metals (titanium of purity 99.999 wt%; chromium of purity 99.999 wt%) under a titanium-gettered argon atmosphere. The samples were flipped, remolten and subsequently cooled down on a water-cooled copper hearth for several times. Next, the samples were annealed for 50 h at 1668 K (in the bcc-solid solution region) to ensure chemical homogeneity and subsequently annealed for 50 h at 1473 K (in the C36 Laves-phase region). These heat treatments were performed in an induction furnace under a high-purity argon atmosphere with the sample placed in an Y$_2$O$_3$ crucible covered with three serial (one after another/cf. no.9 in Figure 1.11) Ti-getter sheets. Before carrying out the annealing the furnace was evacuated and back-filled with argon for several times (starting gas atmosphere contained 0.4 ppm O$_2$ as contaminant in the argon atmosphere of the furnace). After the anneals the samples were rapidly cooled down by switching off the furnace.

The TiCr$_2$ alloys were characterised by chemical analysis (carrier-gas hot extraction (ELTRA ONH 2000), combustion technology (ELTRA CS-800) and Inductively Coupled Plasma Optical Emission (Spectro – CIROS CCD)), electron probe micro analysis (EPMA), X-ray powder diffractometry (XRPD), and laser-granulometric analysis (Mastersizer 2000; Malvern company).

For the DTA and XRPD measurements powders of the TiCr$_2$ alloys were produced within a mortar.

5.3.2 DTA measurements

As differential thermal analysis (DTA) apparatus a DSC 404C Pegasus from Netzsch was used. The apparatus is equipped with a DSC C_p sensor (thermocouple type S) and a high-temperature noble-metal furnace. The measurements were performed under a flowing argon gas atmosphere (99.9999 %; flow rate 50 ml/min). The measured DTA signal was calibrated and desmeared as described in Refs. [25, 26] using Mo and Co as calibration materials. Approximately 120 mg of the powder was used for each DTA run. The powder was put into an Y_2O_3 pan which was itself placed within a platinum sample pan and covered by a platinum lid. For each measurement run fresh specimens were used to ensure that the specimens had the same thermal/mechanical history. The specimens were heated up to 1573 K and subsequently cooled down to 1473 K where they were again homogenised for three hours to eliminate any conceivable decomposition which might take place during cooling down the specimen after specimen preparation (note that during this first heating up the equilibrium C36-C14 phase-transformation temperature T_0 was passed). Thereafter the phase transformations C36→C14 (upon heating) and C14→C36 (upon cooling) were investigated by iso-chronal heating/cooling using different heating-/cooling-rates (± 5, 10, 15, 20 K/min).

Applying the above-mentioned calibration and desmearing procedure [26] the experimental effective heat capacity, $c_{p,\mathrm{exp}}^{\mathrm{eff}}$ as a function of temperature for the heating/cooling rates applied is obtained. The experimental effective heat capacity $c_{p,\mathrm{exp}}^{\mathrm{eff}}$ consists of the true heat capacity (caused by the sample) and of the transformation enthalpy ΔH (C36→C14 and C14→C36). Thus, for the calculation of the peak area/transformation enthalpy as function of temperature (time), $\Delta H\left(T\left(t\right)\right)$, it is necessary to determine the baseline [27], which represents the true heat capacity of the sample $c_{p,\mathrm{true}}$. Within the experimental uncertainty the heat capacities of both phases are the same. The total peak area/transformation enthalpy ΔH_{tot} can be calculated as follows:

$$\Delta H_{\mathrm{tot}} = \int_{T_{onset}}^{T_{end}} \left(c_{p,\mathrm{exp}}^{\mathrm{eff}}\left(T\left(t\right)\right) - c_{p,\mathrm{true}}\left(T\left(t\right)\right) \right)\mathrm{d}T \ . \qquad (5.14)$$

Note that for the phase transformation occurring upon heating $T_{\mathrm{onset}} < T_{\mathrm{end}}$, and for the phase transformation upon cooling $T_{\mathrm{onset}} > T_{\mathrm{end}}$. The observed transformed fraction $f_{\mathrm{exp}}(T(t))$ as function of temperature then is given by:

$$f_{\mathrm{exp}}(T(t)) = \frac{\Delta H(T(t))}{\Delta H_{\mathrm{tot}}} \qquad (5.15)$$

5.3.3 The fit procedure

The transformed fraction $f_{\mathrm{model}}(T(t))$ calculated numerically as function of temperature (time) according to the model described in Section 5.2 was fitted simultaneously to all measured curves of $f_{\mathrm{exp}}(T(t))$ obtained for the different heating rates for the C36$\rightarrow$C14 transformation and all curves of $f_{\mathrm{exp}}(T(t))$ obtained for the different cooling rates for the C14$\rightarrow$C36 transformation. Fitting was performed by minimisation of the sum of the squares of the residuals in f, refining values for the kinetic model parameters according to a simplex procedure [28]. The fitting parameters T_0 and σ were taken the same for the C36$\rightarrow$C14 transformation (occurring upon heating) and for the C14$\rightarrow$C36 transformation (occurring upon cooling). Furthermore, in the model calculations the same parameter ξ, which is a measure for the degree of anisotropic impingement, was used for the modelling of the C36$\rightarrow$C14 transformation and the C14$\rightarrow$C36 transformation. The activation energies for growth $Q_{\mathrm{heat}}^{\mathrm{C36}\rightarrow\mathrm{C14}}$ and $Q_{\mathrm{cool}}^{\mathrm{C14}\rightarrow\mathrm{C36}}$ were allowed to be different for the (forward) C36$\rightarrow$C14 transformation (upon heating) and the backward transformation C14$\rightarrow$C36 (upon cooling).

5.4 Results and discussion

5.4.1 Specimen characterisation

Chemical analysis proved that no uptake of metallic or non-metallic impurities during alloy production took place. The compositions which are lateron referred to have been determined by EPMA and have been gathered in Table 5.1.

The XRPD patterns showed that all alloys (after casting and the subsequent homogenisation annealing treatments) consist of pure C36 Laves phase, which is re-

tained (metastably) at room temperature[1]. The determined lattice parameters for the
C36 phase have been listed in Table 5.1 as well. The mean particle size d of the pow-
der was determined by the laser-granulometric measurement to be $44.3\,\mu m$. In the
following this value will be used as the mean grain size D (cf. Equations (5.3) and
(5.8) and Figure 5.3), assuming that one powder particle consists of one crystal.

Table 5.1 Nominal composition versus composition determined by EPMA of the different alloys. Lat-
tice parameters a and c of the hexagonal C36 phase as determined at room temperature.

	Nominal composition	EPMA	Phase	a_{C36}/Å	c_{C36}/Å
	Ti content/at.%	Ti content/at.%			
Alloy I	33.4	33.7 ± 0.25	C36	4.9090	15.9655
Alloy II	34.3	34.3 ± 0.20	C36	4.9138	15.9758
Alloy III	35.2	35.5 ± 0.20	C36	4.9217	15.9948

5.4.2 Differential thermal analysis

The measured DTA curves of alloy I for the heating-/cooling rates indicated, are
shown in Figure 5.5. The curves were desmeared using the procedure described in [25,
26]. The thus obtained results for the alloys I, II and III (see Figure 5.6) illustrate that
the difference between the phase-transformation start temperatures[2] of the C36→C14
and the C14→C36 transformations decreases with increasing Ti content. This differ-
ence between the start temperatures is referred to as T-hysteresis which is character-
ised by an extent of undercooling/overheating (cf. discussion in Section 5.2.1).

---

[1] In the TiCr$_2$ system the C15 phase is actually stable at room temperature, but this phase forms only
after very long heat treatment at suitable temperatures (approximately 1273 K; see Figure 5.2).
[2] The phase-transformation start temperature T_{start} is the temperature at which a detectable amount of the
new phase is formed, i.e. the temperature at which the largest arrays of synchro-Shockley partial dislo-
cation dipoles in the crystal become able to glide (see Section 5.2.1) and the transformed fraction thus
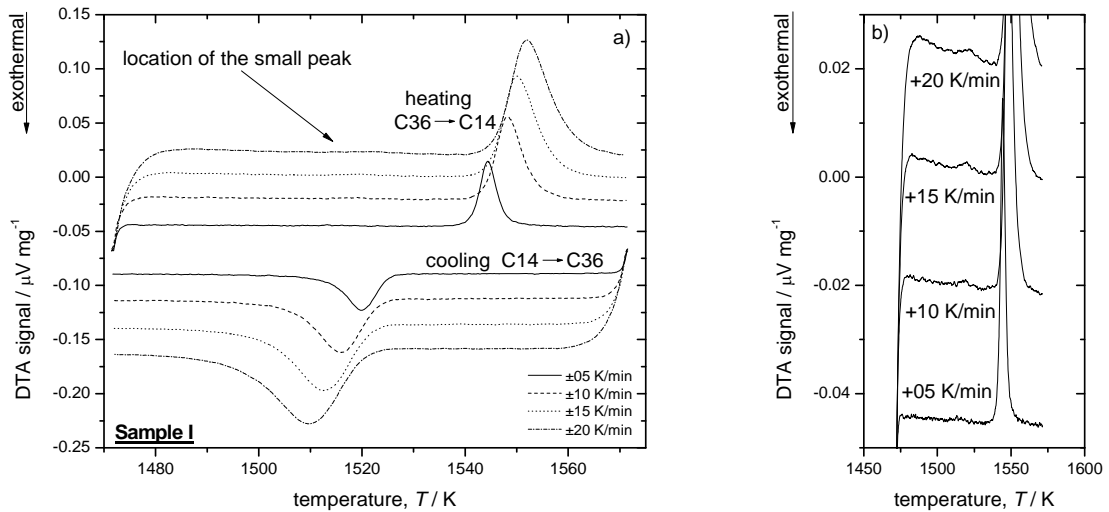starts to depart from zero during isochronal heating or isochronal cooling.

Figure 5.5: a) As-measured DTA curves for the heating/cooling rates indicated (alloy I). b) Enlarged section: A small peak is visible; the location of this small peak (see text) has also been indicated in the left plot.
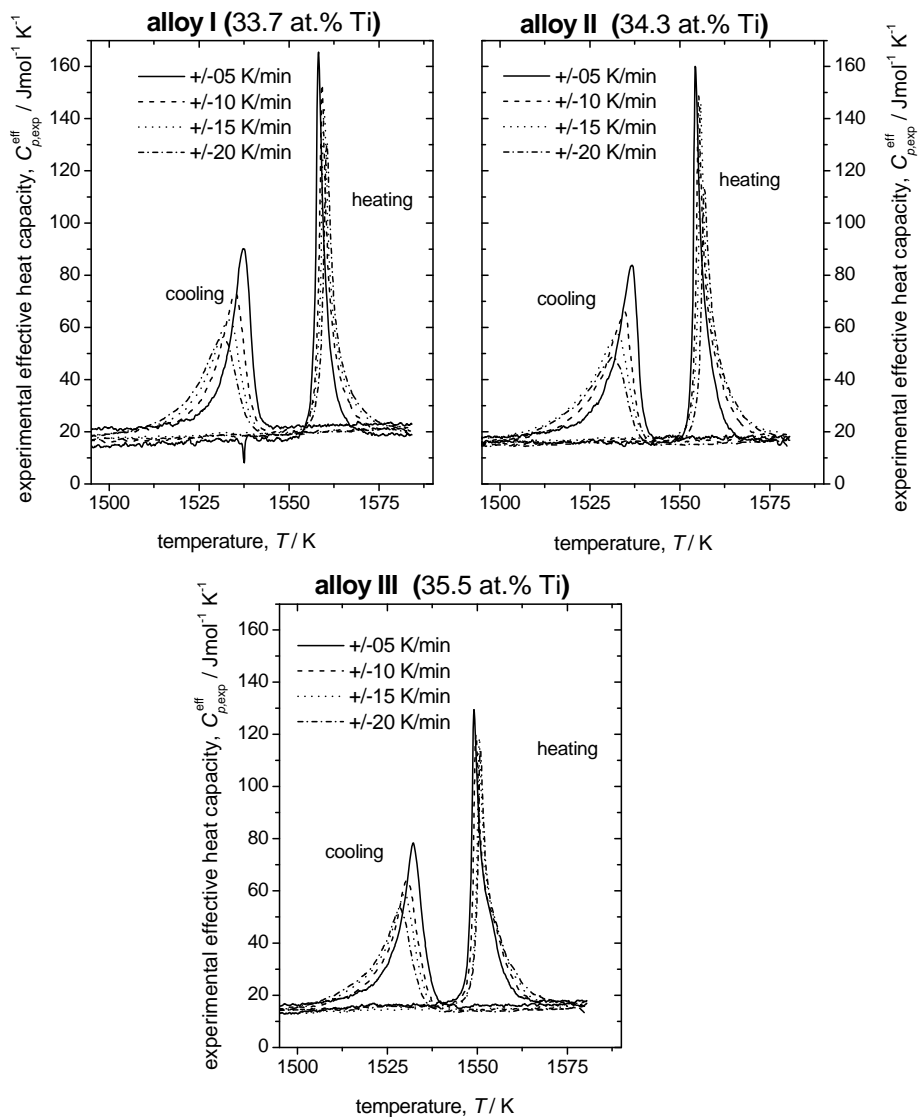

Figure 5.6: Calibrated and desmeared DTA curves as obtained for alloys I, II and III for the heating-/cooling rates indicated.

From the calibrated and desmeared DTA curves the total phase-transformation enthalpies ΔH_{tot} were determined (cf. Section 5.3.2); the results have been listed in Table 5.2. The standard deviation of the determined values of the total transformation enthalpies, as averaged from the values determined for each alloy for different heating-/cooling rates, is only 2.5 %; this deviation characterises the accuracy of the calorimetric measurements. The difference of the absolute values of the total transformation enthalpies of the C14→C36 transformation and the C36→C14 transformation is approx. 5.5 %, which is considered significant (see what follows).

Upon close inspection of the DTA curves recorded upon heating a small *pre-peak* is observed before emergence of the transformation peak (see Figure 5.5 right plot). The area of the small peak was determined to be about 25 J/mol. Hence the enthalpy change associated with this *pre-peak* appears to account for the small difference in absolute value of $\Delta H_{\text{tot}}^{\text{C14}\rightarrow 36}$ and $\Delta H_{\text{tot}}^{\text{C36}\rightarrow\text{C14}}$ with $\left|\Delta H_{\text{tot}}^{\text{C36}\rightarrow\text{C14}}\right| < \left|\Delta H_{\text{tot}}^{\text{C14}\rightarrow\text{C36}}\right|$. This suggests that a small part of the alloy already transforms from C36 to C14 before the *intrinsic* phase transformation itself takes place, i.e. the pre-peak occurs before the equilibrium phase-transformation temperature T_0 is passed during isochronal heating.

Table 5.2 Determined total phase-transformation enthalpies for the phase transformations occurring upon heating ($*$ not considering the small *pre-peak*) and cooling.

alloy	$\dfrac{\Delta H_{\text{tot}}^{\text{C36}\rightarrow\text{C14}\ *}}{\text{J/mol}}$	$\dfrac{\Delta H_{\text{tot}}^{\text{C14}\rightarrow\text{C36}}}{\text{J/mol}}$
I (33.7 at.% Ti)	511	-544
II (34.3 at.% Ti)	527	-562
III (35.5 at.% Ti)	511	-534

It may be suggested that the pre-peak is due to a dissociation (of arrays) of perfect synchro dislocation dipoles into (twice as much arrays of) synchro-Shockley partial dislocation dipoles. At $T < T_0$ there is no driving force for the C36→C14 transformation as realised by glide of (ordered arrays of) synchro-Shockley partial dislocation (dipoles); cf. Figure 5.3. However, dissociation of (arrays of) perfect synchro dislocation dipoles can occur at a temperature $T < T_0$ if the energy cost for generation of the stacking faulted area in-between the separating partial dislocation dipoles (i.e. the energy of the C14-phase region in-between the partial dislocation dipoles, as compared to a corresponding C36 phase region; note that this unfavourable energy (difference) decreases with increasing temperature (see Figure 5.4)) can be compensated by the

elastic energy gained through the dislocation dissociation (partial dislocations repel each other). Because the repulsive force of the partial dislocations decreases very rapidly with increasing separation distance of the partials [24], only a very small separation of synchro-Shockley partial dislocation dipoles is realised and thus this (premature) part of the C36 $\rightarrow$ C14 phase transformation is very small. The large peak reflects the intrinsic phase transformation which starts at $T \geq T_0$ when the energy difference ΔG_A changes its sign (i.e. becomes negative; cf. Figure 5.4).

During cooling down no pre-peak is expected for the C14 $\rightarrow$ C36 transformation: Start of this transformation occurs in the presence of (pairs of arrays of) widely separated synchro-Shockley partial dislocation dipoles, which must recombine to complete the backward, C14 $\rightarrow$ C36 transformation. Hence, in principle an *after-peak* should be expected for the C14 $\rightarrow$ C36 transformation (at the same temperature where the pre-peak occurs upon heating). However, this effect cannot be detected separately since it is covered by the large intrinsic C14 $\rightarrow$ C36 transformation peak (cf. Figure 5.5a).

5.4.3 Extraction of kinetic parameters – *the modular approach*

The transformation rates $\mathrm{d}f_{\mathrm{exp}}/\mathrm{d}T$ ($\mathrm{d}f_{\mathrm{exp}}/\mathrm{d}T = 1/\Phi\ \mathrm{d}f_{\mathrm{exp}}/\mathrm{d}t$) have been plotted in Figure 5.7 as function of the transformed fraction $f_{\mathrm{exp}}\big(T(t)\big)$ for the different alloys and the different heating/cooling rates. The corresponding curves for the experimentally determined transformed fractions $f_{\mathrm{exp}}\big(T(t)\big)$ (see Section 5.3.2, Equation (5.15)) are shown in Figure 5.8 as function of temperature $T(t)$. Evidently, the maximum transformation rate occurs at $f_{\mathrm{exp}} < 0.5$. This is a strong indication for anisotropic growth [18]; the impingement mode for anisotropic growth (introduced in Section 5.2.4) has thus been used in the kinetic model of the phase transformation. In view of the transformation mechanism this impingement mode can be expected (cf. Sections 5.2.1 and 5.2.2).
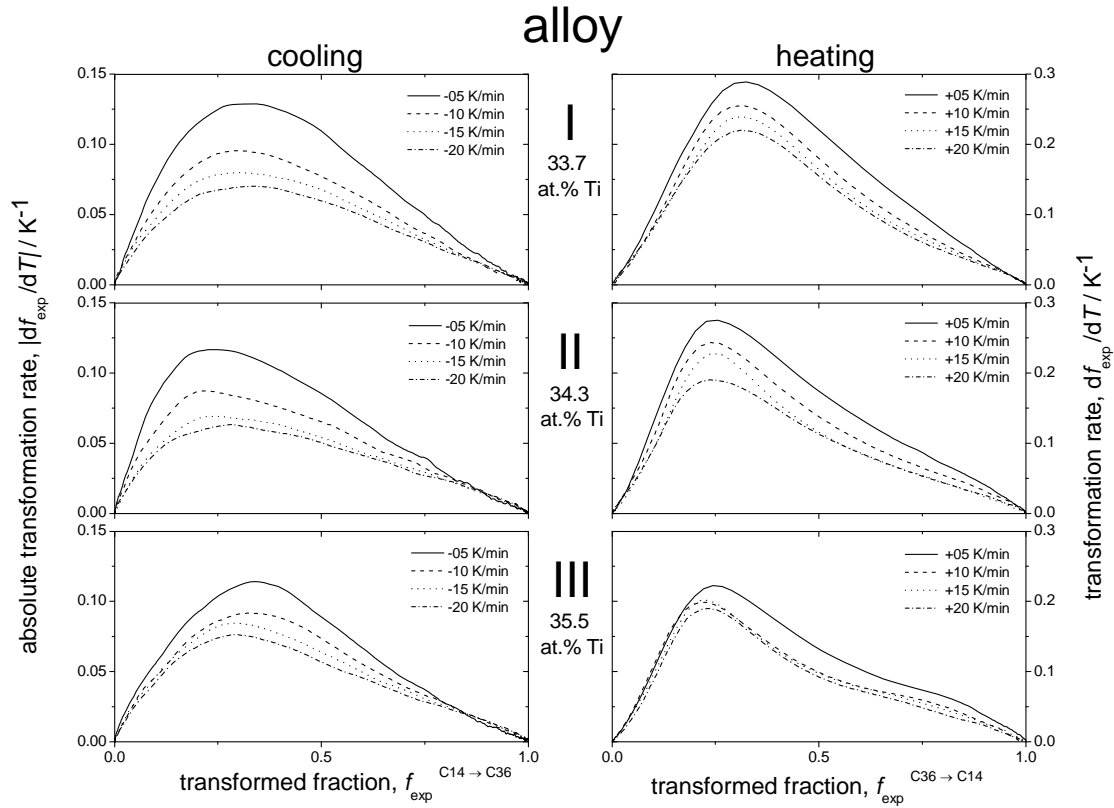
Figure 5.7: The transformation rate df_{exp}/dT as a function of the transformed fraction for the $C36 \rightarrow C14$ transformation (plots on the right side of Figure 5.7) and for the $C14 \rightarrow C36$ transformation (plots on the left side of Figure 5.7) for various heating/cooling rates. The plots show for all alloys a maximum at the left hand side of the plot which is a strong indication for impingement due to anisotropic growth.

The kinetic model description is based on the three overlapping mechanisms: nucleation described by Equation (5.6), growth described by Equation (5.10) and impingement described by Equation (5.13). The fitting parameters are $T_0, \sigma, \xi, Q_{heat}^{C36 \rightarrow C14}$ and $Q_{cool}^{C14 \rightarrow C36}$ (cf. Section 5.3.3). Adopting grains of a mean grain size D the total number of nuclei, assuming that every synchro-Shockley partial dislocation dipole necessary for the transformation is one nucleus (one perfect synchro-Shockley partial dislocation dipole corresponds with two nuclei; cf. Figure 5.3), N_{tot}, was estimated to be $2 \times 3.185 \times 10^{17}$ m^{-3}, thereby supposing that for every (fourth) layer-sandwich unit, which has to be transformed (shifted; cf. Sections 5.1.2 and 5.1.3), one perfect synchro dislocation dipole, which produces two synchro-Shockley partial dislocation dipoles, is available. This value for N_{tot} is a rough estimation as the number of synchro-Shockley partial dislocation dipoles in a nucleus is at the beginning of the transformation larger than one (cf. Section 5.2.1 and Figure 5.4). However, the values of the fit parameters do not depend strongly on the value of N_{tot} (see below). The temperature-independent

dislocation/interface velocity v_0 was estimated by using the well-known (empirical) expression for the pre-exponential factor for lattice-resistance controlled glide of dislocations via kinks, which reads $\dot{\gamma}_p = v_0/(10|\mathbf{b}|) = 1 \cdot 10^{11}$ s^{-1} with $\mathbf{b}$ as the Burgers vector (this result has been validated for a wide range of material classes [29]). For the present Laves phases this leads to $v_0 = 200$ ms^{-1}. Using this estimate for v_0 the pre-exponential factor $M_0 = v_0/RT$ [18] was assessed at 0.0167 m mol J^{-1}s^{-1}, adopting a mean value for the temperature T (and so the same M_0 was used for the phase transformations occurring on heating and on cooling). Note that the temperature dependence of M_0 is small in comparison to the temperature dependence of the exponential term in M (see Equation (5.9)) and thus the error made by adopting M_0 as temperature independent is small.

The kinetic model introduced in Section 5.2 could thus be fitted very well to the experimentally determined transformed fraction (see Figure 5.8), leading to values for the fitting parameters gathered in Table 5.3.

Table 5.3 Results of fitting the kinetic model simultaneously to all transformation curves recorded upon heating and cooling. T_0 = equilibrium phase-transformation temperature; σ = interface energy; ξ degree of anisotropic impingement. $Q_{\text{heat}}^{\text{C36}\rightarrow\text{C14}}$ = activation energy of growth for the C36 $\rightarrow$ C14 transformation; $Q_{\text{cool}}^{\text{C14}\rightarrow\text{C36}}$ = activation energy of growth for the C14 $\rightarrow$ C36 transformation.

alloy	T_0 / K	σ / 10^{-3} Jm^{-2}	ξ	$Q_{\text{heat}}^{\text{C36}\rightarrow\text{C14}}$ /kJmol^{-1}	$Q_{\text{cool}}^{\text{C14}\rightarrow\text{C36}}$ /kJmol^{-1}
I (33.7 at.% Ti)	1549.8	0.29	1.63	75	107
II (34.3 at.% Ti)	1547.0	0.20	1.67	87	112
III (35.5 at.% Ti)	1542.3	0.15	1.65	93	112

A change of the values adopted for the pre-exponential factor M_0 and N_{tot} by a factor of 10 leads to a change of the activation-energy values of about ± 29 kJ/mol. The resulting values for T_0 have been given up to the first decimal, recognising that a change of T_0 of 0.1 K leads to an increase of 2 % of the sum of the squares of the residuals in f (cf. Section 5.3.3).
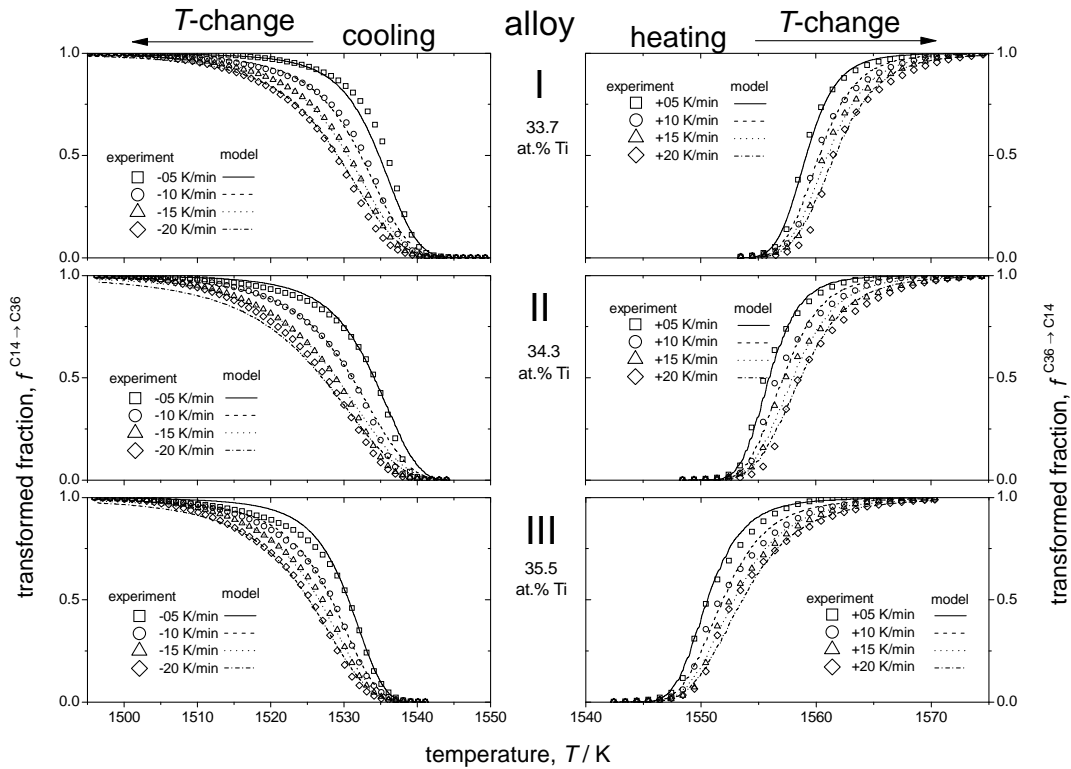
Figure 5.8: Comparison of the experimentally determined transformed fraction $f_{exp}\left(T(t)\right)$ (data points; see Equation (5.15)) and the transformed fraction $f_{model}\left(T(t)\right)$ (lines) obtained by fitting the kinetic model simultaneously to all transformation curves recorded for the $C36 \rightarrow C14$ upon heating and the $C14 \rightarrow C36$ transformation upon cooling, for the various heating/cooling rates.

The activation energy determined for the $C14 \rightarrow C36$ phase transformation occurring upon cooling is for all alloys investigated significantly larger than that for the $C36 \rightarrow C14$ phase transformation occurring upon heating. Further, both the activation energy for the $C14 \rightarrow C36$ phase transformation and the activation energy for the $C36 \rightarrow C14$ phase transformation increase with increasing Ti content (see Figure 5.9). These results could be discussed as follows.

Figure 5.9: Activation energy of the C36→C14 and the C14→C36 phase transformations as function of the Laves phase composition.

The mechanism proposed for the C36→C14 and the C14→C36 phase transformations is based on glide of synchro-Shockley partial dislocation dipoles propagating along (0001) basal planes. Generally, glide of dislocations in crystals occurs on close-packed planes in close-packed directions. The stress τ_g required for glide of a dislocation may depend exponentially on $-d/|\mathbf{b}|$ whe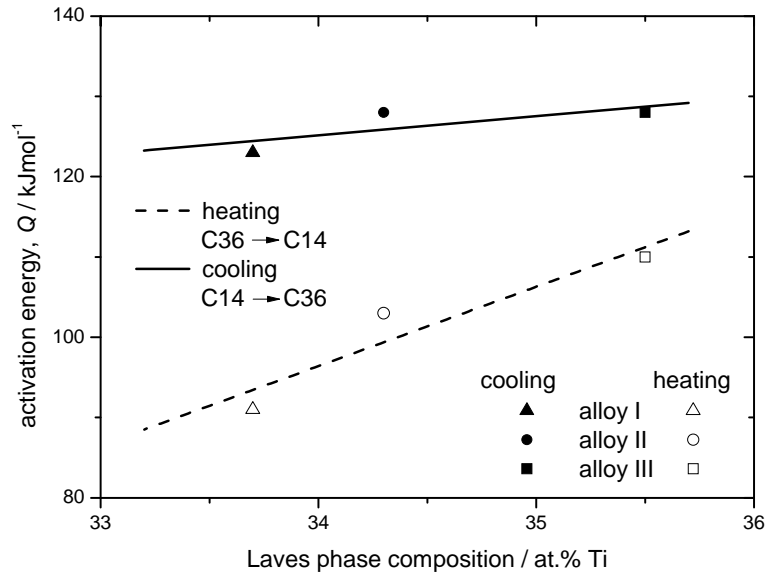re d is the spacing of the glide planes and $|\mathbf{b}|$ is the length of the Burgers vector [24]. Thus it follows for dislocation glide on the (0001) basal plane of a hexagonal pure metal that τ_g depends exponentially on $-c/a$, i.e. the larger c/a, the easier dislocation glide. For a comparison of the dihexagonal C36 and the hexagonal C14 phase, on this basis, the correspondences of the c and a lattice parameters must be considered. In view of the above discussion the c lattice parameter should encompass two layer-sandwich units. This is the case for C14; in the case of C36 the c lattice parameter comprises four layer-sandwich units and hence has to be divided by two. Considering the Kagomé net of B atoms, the a lattice parameter of both Laves phases has been defined identically. The thus defined and determined values for "c/a" are shown in Figure 5.10 as function of the Laves-phase composition. It follows that the "c/a" ratio of the C14 phase is smaller than that of the C36 phase and that the "c/a" ratio for both phases decreases with increasing Ti content. On the basis of the above discussion it may then be suggested that (i) glide of the synchro-Shockley partial dislocations along the basal plane is easier in the C36

phase than in the C14 phase and that (ii) such glide in both phases becomes more diffi-
cult with increasing Ti content. Both expectations, (i) and (ii), are consistent with the
experimental results obtained for the activation energies of growth (Table 5.3 and Fig-
ure 5.9). These results thereby also support the proposed transformation mechanism
based on glide of synchro-Shockley partial dislocations.

The ratio of the activation energy for interdiffusion and the activation energy
for dislocation glide controlled by a lattice resistance varies from metals to non-metals
from 7 to 1.5 (as calculated from data in Ref. [29]). The activation energy for (in-
ter)diffusion in the TiCr$_2$ Laves phases amounts to $Q^{\mathrm{D}}_{\mathrm{TiCr_2}} = 278$ kJ/mol [30]. The val-
ues obtained in this work for the activation energy of growth Q are about 3 times
smaller than $Q^{\mathrm{D}}_{\mathrm{TiCr_2}}$, which is compatible with the above range for the ratio of the acti-
vation energies of interdiffusion and dislocation glide, thereby providing further sup-
port for the proposed transformation mechanism based on glide of synchro-Shockley
partial dislocations.
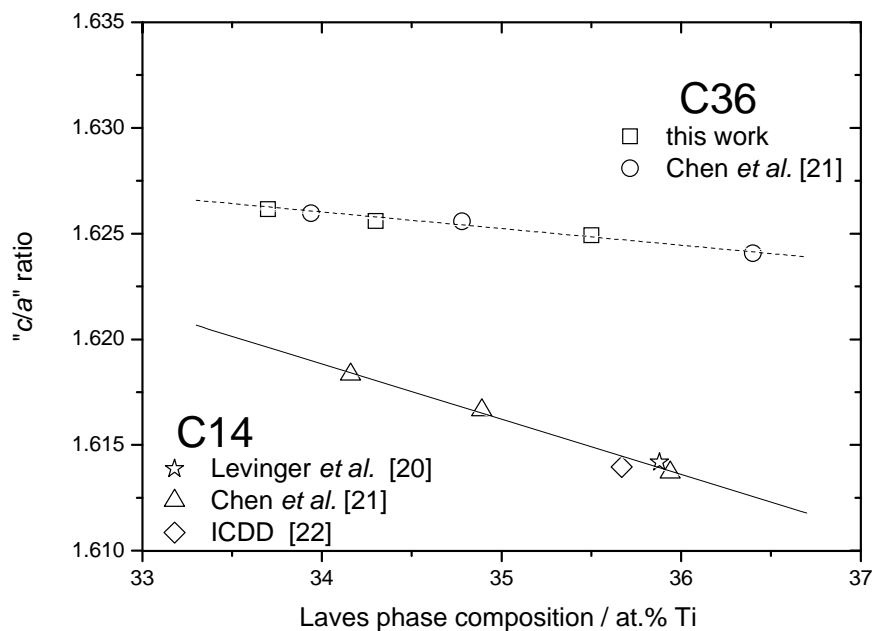
Figure 5.10: The "c/a" lattice-parameter ratio (see text) for the hexagonal C36 and C14 TiCr$_2$ Laves
phases as function of the Laves-phase composition.

Often a Kissinger-like analysis [31, 32] is used in the literature to determine ac-
tivation energies of phase transformations. Application of a Kissinger-like analysis
presupposes a large driving force for the transformation, which is not always recog-
nised. In the present case Kissinger-like analysis leads to abnormally high activation
energies. Failure of the Kissinger-like analysis applied near the equilibrium phase-

transformation temperature T_0, as holds for the present case, has been recently discussed in Ref. [33].

The value determined for the equilibrium phase-transformation temperature T_0 indicates a slight decrease of T_0 with increasing Ti content (see Table 5.3). This minor dependence of T_0 on Ti content is consistent with the extreme narrowness of the C36-C14 two-phase field, which has been represented by a single horizontal line (!) in the phase diagram [6, 7] (see Figure 5.2). Note that this observed trend for the T_0 value is opposite to the trend predicted by a thermodynamic assessment of the Ti-Cr system [6].

The value determined for the interface energy σ decreases with increasing Ti content (see Table 5.3). The kinetic model fitting made clear that this decrease of the value of σ describes the decrease of the difference between the phase-transformation start temperatures (see Footnote 2 on page 114), T_{start}, of the C36$\rightarrow$C14 and the C14$\rightarrow$C36 transformations with increasing Ti content (see Figures 5.6 and 5.8). The interfacial energy σ determines the difference $T_{\text{start}} - T_0$, i.e. the necessary overheating/undercooling: the transformation can only start if the contribution of the interfacial energy can be (over) compensated by the decrease of chemical Gibbs energy (cf. Equation (5.5)).

5.5 Conclusions

- The kinetics of the polytypic C36$\rightarrow$C14 and C14$\rightarrow$C36 phase transformations, taking place near the equilibrium phase-transformation temperature, can be well described on the basis of a modular transformation model adopting an athermal nucleation mode, and a strongly anisotropic, interface-controlled growth mode.

- All data obtained support a mechanism for both transformations involving glide of ordered arrays of synchro-Shockley partial dislocation dipoles.

- The absolute values of the total transformation enthalpies for the C36→C14 transformation (occurring upon heating) and the C14→C36 transformation (occurring upon cooling) differ significantly. The difference can be ascribed to a dissociation of the arrays of perfect synchro dislocation dipoles occurring upon heating before the intrinsic C36→C14 transformation starts, whereas the C14→C36 transformation occurring upon cooling includes the recombination of the synchro-Shockley partial dislocation dipoles into perfect synchro dislocation dipoles.

- The activation energy for glide of the synchro-Shockley partial dislocations depends distinctly on the ratio of the "corresponding" c and a lattice parameters. This ratio is smaller for the C14 phase than for the C36 phase and thus the activation energy of growth is larger for the C14→C36 transformation than for the C36→C14 transformation. The "c/a" ratio decreases for both phases with increasing Ti content. This is consistent with the observed increase of the activation energy of growth with increasing Ti content for both the C36→C14 transformation and the C14→C36 transformation.

- The difference between the start temperature of the phase transformation and the equilibrium phase-transformation temperature is governed by the interfacial energy of product phase and parent phase, which significantly decreases with increasing Ti content (above the stoichiometric value).

5.6 References

[1]   F. Stein, M. Palm, G. Sauthoff, Structure and stability of Laves phases. Part I. Critical assessment of factors controlling Laves phase stability, Intermetallics 12 (2004) 713.

[2]   G.E.R. Schulze, Zur Kristallchemie der intermetallischen AB$_2$-Verbindungen (Laves-Phasen), Z. Elektrochem. 45 (1939) 849.

[3]   G. Sauthoff, Intermetallics, Weinheim: VCH, 1995.

[4]   J.D. Livingston, Laves-phase superalloys?, Phys. Status Solidi 131 (1992) 415.

[5]   K.S. Kumar, P.M. Hazzledine, Polytypic transformations in Laves phases, Intermetallics 12 (2004) 763.

[6]   Z. Zhuang, J. Shen, Y. Liu, L. Ling, S. Shang, Y. Du, J.C. Schuster, Thermodynamic optimization of the Cr-Ti system, Z. Metallkd. 91 (2000) 121.

[7]   H. Okamoto, Chromium-Titanium, J. Phase Equilib. 23 (2002) 382.

[8]   F. Stein, M. Palm, G. Sauthoff, Structure and stability of Laves phases part II - structure type variations in binary and ternary systems, Intermetallics 13 (2005) 1056.

[9]   M.L. Kronberg, Plastic deformation of single crystals of sapphire: Basal slip and twinning, Acta Metall. 5 (1957) 507.

[10]   C.W. Allen, P. Delavignette, S. Amelinckx, Electron microscopic studies of the Laves phases TiCr$_2$ and TiCo$_2$, Phys. Status Solidi A 9 (1972) 237.

[11]   M.F. Chisholm, K.S. Kumar, P.M. Hazzledine, Dislocations in complex materials, Science 307 (2005) 701.

[12]   P.M. Hazzledine, P. Pirouz, Synchroshear transformations in Laves phases, Scr. Metall. Mater. 28 (1993) 1277.

[13]   K.C. Liao, C.W. Allen, Shear transformation in the TiCr$_2$ Laves phase, International Conference of Solid-Solid Phase Transformations (1981) 1493.

[14]   J. Aufrecht, W. Baumann, A. Leineweber, V. Duppel, E.J. Mittemeijer, Layer-stacking irregularities in C36-type Nb-Cr and Ti-Cr Laves phases and their relation with polytypic phase transformations, Phil. Mag., accepted. (2010).

[15]   J. Aufrecht, A. Leineweber, V. Duppel, E.J. Mittemeijer, Transformation-dislocation dipoles in Laves phases; a high-resolution transmission electron microscopy analysis, as submitted for publication (2010).

[16]   M. Hillert. Phase Equilibria Phase Diagrams and Phase Transformations - Their Thermodynamic Basis, Cambridge: University Press, 1998.

[17]   E.J. Mittemeijer, F. Sommer, Solid state phase transformation kinetics: a modular transformation model, Z. Metallkde 93 (2002) 352.

[18]   F. Liu, F. Sommer, C. Bos, E.J. Mittemeijer, Analysis of solid state phase transformation kinetics: models and recipes, Int. Mater. Rev. 52 (2007) 193.

[19]   M. Cohen, G.B. Olson, A general mechanism of martensitic nucleation: Part I. General concepts and the FCC→HCP transformation, Metall. Trans. A 7 (1976) 1897.

[20]   B.W. Levinger, High temperature modification of $TiCr_2$, J. Met. 5 (1953) 196.

[21]   K.C. Chen, S.M. Allen, J.D. Livingston, Stoichiometry and alloying effects on the phase stability and mechanical properties of $TiCr_2$-base Laves phase alloys, Mater. Res. Soc. Symp. Proc. 364 (1995) 1401.

[22]   ICDD database (1999) PDF-number 00-050-1514.

[23]   M. Lin, G.B. Olson, M. Cohen, Distributed-activation kinetics of heterogeneous martensitic nucleation, Metall. Trans. A 23 (1992) 2987.

[24]   J.P. Hirth, J. Lothe, Theory of Dislocations, Malabar: Mc-GrawHill, 1968.

[25]   A.T.W. Kempen, F. Sommer, E.J. Mittemeijer, Calibration and desmearing of a differential thermal analysis measurement signal upon heating and cooling, Thermochim. Acta 383 (2002) 21.

[26]   W. Baumann, A. Leineweber, E.J. Mittemeijer, Calibration and desmearing of a differential thermal analysis measurement signal - upon heating and cooling - in the high-temperature region, Thermochim. Acta 472 (2008) 50.

[27]   A.T.W. Kempen, F. Sommer, E.J. Mittemeijer, The kinetics of the austenite-ferrite phase transformation of Fe-Mn: differential thermal analysis during cooling, Acta Mater. 50 (2002) 3545.

[28]   J.C. Lagarias, J.A. Reeds, M.H. Wright, P.E. Wright, Convergence Properties of the Nelder-Mead Simplex Method in Low Dimensions, SIAM Journal of Optimization 9 (1998) 112.

[29]   H.J. Frost, M.F. Ashby, Deformation-Mechanism Maps - The Plasticity and Creep of Metals and Ceramics, Kronberg-Taunus: Pergamon Press GmbH, 1982.

[30]   M. Wein, L. Levin, S. Nadiv, The mechanism of mixing and reactive diffusion in intermetallics ($TiFe_2$, $TiCr_2$), Phil. Mag. A 38 (1978) 81.

[31]   H.E. Kissinger, Reaction Kinetics in Differential Thermal Analysis, Anal. Chem. 29 (1957) 1702.

[32]   E.J. Mittemeijer, Analysis of the kinetics of phase transformations, J. Mater. Sci. 27 (1992) 3977.

[33]   W. Baumann, A. Leineweber, E.J. Mittemeijer, as submitted for publication (2010).

Chapter 6

The influence of plastic deformation on polytypic phase transformations in TiCr$_2$ Laves phases

Wolfgang Baumann, Andreas Leineweber and Eric Jan Mittemeijer

Abstract

A systematic investigation of the kinetics of the forward and backward polymorphic C36 $\rightleftarrows$ C14 Laves-phase transformation of TiCr$_2$ close to the equilibrium phase-transformation temperature of about 1550 K was performed, on the basis of heating- and cooling-rate dependent differential thermal analysis (DTA) measurements. Plastic deformation induced by compressing (using a hydraulic press) considerably affects the C36 $\rightleftarrows$ C14 phase-transformation kinetics. This is ascribed to the presence of so-called synchro(-Shockley partial) dislocations induced upon plastic deformation during compression. The influence on the phase-transformation kinetics is shown to vary with the degree of plastic deformation, i.e. with the dislocation density as characterised by the extent of the (X-ray) diffraction-line broadening.

6.1 Introduction

The mechanism of the polytypic $C36 \rightleftarrows C14$ phase-transformation of Laves phases has been ascribed to the glide of ordered arrays of so-called synchro-Shockley partial dislocation dipoles [1-6]: A synchro-Shockley partial dislocation dipole consists of two single synchro-Shockley partial dislocations of opposite Burgers vectors, which propagate above and below a layer-sandwich unit. The array of these dipoles is ordered such that a dipole encloses every fourth layer-sandwich unit (for details, see Ref. [7]). However, a kinetic model for the phase transformation has not been presented in these works. Recent work by our group [8] led to a kinetic model for the $C36 \rightleftarrows C14$ equilibrium phase transformation on the basis of the general *modular approach* [9, 10]. The model was used successfully applying differential thermal analysis (DTA) data on the $C36 \rightleftarrows C14$ $TiCr_2$ Laves-phase transformations occurring upon heating and cooling. In this letter this approach will be used to reveal the effect of a varying degree of plastic deformation on the forward and backward $C36 \rightleftarrows C14$ phase transformation of the $TiCr_2$ Laves phase.

6.2 Experimental

The chemical composition of the (initial) $C36$-$TiCr_2$ alloy investigated in this work was (35.6 ± 0.3) at.% Ti/(64.4 ± 0.3) at.% Cr as determined by electron-probe microanalysis. For a detailed description of the specimen preparation, see Ref. [7]. For the DTA measurements and the X-ray powder diffraction (XRPD) investigations a fine powder was produced in a mortar (for details see [7, 8]). Subsequently, using a hydraulic press, some powder was compressed into slices at compressing stresses of approx. 1.5 GPa and 2.5 GPa (i.e. the force of the extrusion die per unit area); one slice compressed at 2.5 GPa was crushed and again compressed at 2.5 GPa (this specimen is labelled 2×2.5 GPa).

For the DTA experiments a DSC 404C Pegasus from Netzsch was used. The apparatus is equipped with a DSC C_p sensor (thermocouple Type S) and a high-temperature noble-metal furnace. All measurements were performed at a heating-/cooling-rate of ± 20 K/min under a dynamic argon atmosphere (99.9999 %; flow rate 50 ml/min). The raw DTA measurement curves (see Figure 6.2 for some of the data) were calibrated and desmeared as described in Refs. [8, 11, 12].

The XRPD experiments were performed at room temperature using a Philips X`Pert MPD diffractometer equipped with a germanium monochromator in the incident beam, yielding Cu-K$_{\alpha 1}$ radiation (for details see Ref. [7]). The broadened diffraction lines were corrected for instrumental line-broadening contributions [13]; for evaluation details see Ref. [7].

6.3 Results and discussion

6.3.1 X-ray diffraction line-broadening analysis

According to the classical Williamson and Hall analysis [13-15] it holds: $\dfrac{\beta_{hkl} \cos\theta_{hkl}}{\lambda} = \dfrac{1}{D_{\text{domain}}} + \dfrac{4e\sin\theta_{hkl}}{\lambda}$, where θ_{hkl} is the peak position of the corresponding *hkl*-reflection, λ is the wavelength of the X-rays, e is a measure for the microstrains within the specimen and D_{domain} is the volume-weighted mean size of the coherently diffracting domains. A plot of $\beta_{hkl} \cos\theta_{hkl}/\lambda$ vs. $4\sin\theta_{hkl}/\lambda$ for various *hkl* reflections, should yield a straight line, the slope of which gives the value of e for the specimen concerned. By means of X-ray diffraction line-broadening analysis the integral breadths β_{hkl} of the $h - k = 3N$ reflections (with integer *N*) were determined; these reflections may show line-broadening due to microstrains but not due to layer-stacking faults [7, 16]; the results obtained for these reflections are shown in Figure 6.1. Upon compressing the C36 phase powder the value of e clearly increases. If this specimen is heated to above the C36$\rightleftarrows$C14 Laves phase-transformation temperature (heating to 1573 K) the compressing-induced microstrain is reduced but not fully relieved (see Figure 6.1). If the specimen is heated up into the solid-solution bcc phase field (heating to 1673 K), the compressing-induced microstrain disappears completely. This can be discussed as follows.
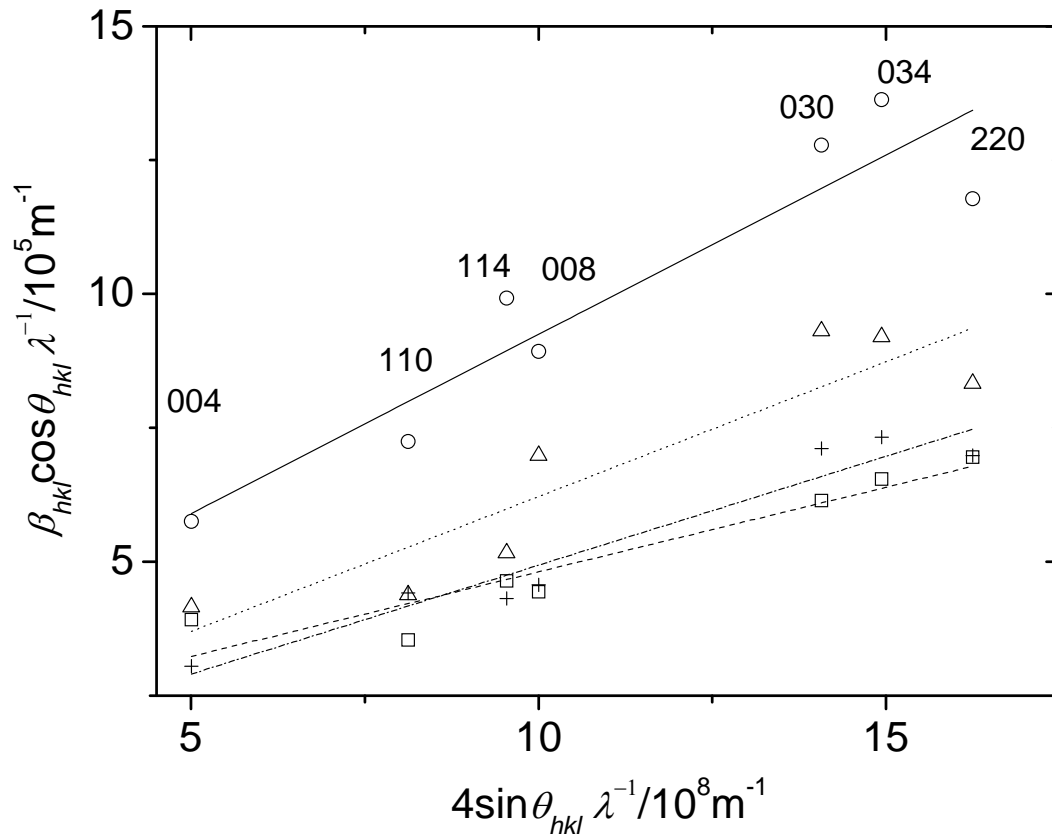
Figure 6.1: Williamson-Hall plot; the slope of the straight lines fitted to (corresponding) data points is a measure for the microstrain e (and thus the dislocation density) within the specimen. $\square$: original powder; $\bigcirc$: powder after having compressed at 1.5 GPa; $\triangle$: after having compressed at 1.5 GPa and having completed the C36 $\rightarrow$ C14 Laves phase transformation (heating to 1573 K); + after having compressed at 1.5 GPa and having entered the solid solution (bcc) region (heating to 1673 K). The Laue indices have been indicated. The XRPD experiments were performed at room temperature.

Plastic deformation in Laves phases involves more complex atomic motion than required in simple metal crystal structures: Slip by the synchroshear mechanism is realized by glide of a pair of synchro-Shockley partial dislocations [17-21]. In the case of the compressed, untransformed specimens the increase of the microstrain upon compression is ascribed to the deformation induced increase of the density of synchro dislocations (see "$\bigcirc$" points in Figure 6.1). By such plastic deformation (compressing) an excess of synchro dislocations of the same sign is generated, i.e. dipoles are not produced.

The higher the compressing stress applied or the larger the number of compressing cycles, the larger the degree of deformation and thus the (synchro) dislocation density is expected to be. By passing the forward and backward C36 $\rightleftarrows$ C14 Laves-phase transformation a part of the deformation-induced dislocations are annihilated but a considerable amount remains in the specimen (see "$\triangle$" points in Figure 6.1). Annihilation of dislocations in the Laves phases is, even at elevated temperatures, not as easy

as in simple (metal) structures. Synchro dislocations, cannot climb through the assumedly rigid *layer-sandwich units* [5], leaving glide as the only possibility for a (synchro) dislocation to meet another one on the same glide plane with opposite Burgers vector, and to annihilate.

The dislocations are removed completely upon entering the Ti-Cr bcc solid solution phase region (see "+" points in Figure 6.1), since in the transformation to bcc a totally new microstructure develops, during which lattice defects in the parent structure are simply annihilated, whereas in the C36 $\rightleftarrows$ C14 transformation the grains are preserved: Only the stacking sequences within the grains are changed by glide of synchro-Shockley partial dislocations. This interpretation of the diffraction line-broadening data is consistent with the observations made by DTA analysis (see what follows).

6.3.2 DTA measurements

The raw data of the DTA measurement runs for the uncompressed specimen (one heating/cooling cycle) and the specimen compressed at 2.5 GPa (various successive heating/cooling cycles) are shown in Figure 6.2 (the heating and the cooling run of the uncompressed specimen are presented in Figure 6.2b (solid lines)). DTA curves after calibration and desmearing (see above) determined for the uncompressed specimen and for specimens deformed under different compressing stresses (in one case two times at the same compressing stress) are shown in Figure 6.3.

A small pre-peak occurring upon heating for the uncompressed condition (see Figure 6.2c) has been attributed [8] to dissociation of (the arrays of) perfect synchro dislocation dipoles (carrying the phase transformation) into synchro-Shockley partials. This effect does not occur for the compressed specimen during the first heating run (see Figure 6.2c), but reappears in the further heating runs. This suggests that such dissociation of the arrays of perfect synchro dislocation dipoles into partials has already occurred during the plastic deformation. Indeed, stacking faults/dissociated dislocations (on the basal plane) have been frequently observed in deformed Laves phases [21, 22]. The appearance of the pre-peak in the heating runs of the subsequent cycles can be understood: Upon cooling after the first heating run (after passing the C36$\rightarrow$C14 transformation) after deformation (i.e. upon the C14$\rightarrow$C36 transformation) the synchro-Shockley partial dislocations carrying the C14$\rightarrow$C36 transformation recombine [8].

After that the compressed specimen has experienced for the first time a forward C36→C14 transformation and a backward C14→C36 transformation, the DTA peak shape and -position do not change further upon continued cycling (heating-cooling/see measurement runs 1-6 in Figure 6.2); in the first run the microstructure stabilises (i.e. some dislocations were annihilated; cf. "○" and "△" points in Figure 6.1). For the following quantitative evaluation the 5th run (a heating run) and the 6th run (the subsequent cooling run) were used (see further below).

If the compressed specimen is heated up to the solid-solution, bcc region (run 7b not shown in Figure 6.2b; i.e. the C14→bcc transformation peak is not shown), the compressing-induced microstrain, attributed to dislocations, is fully removed (see discussion in Section 6.3.1 regarding the XRPD line broadening data shown in Figure 6.1). This indicates that the existing dislocations/dislocation structure had been removed. During subsequent cooling down from the bcc region (the 8th run in Figure 6.2b; the bcc→C14 transformation peak is only partly shown) the C14→C36 transformation peak (Figure 6.2b) occurs at higher undercooling, as compared to the 2nd, 4th and 6th cooling runs. This observation is consistent with the assumption that the dislocation structures had been annihilated before (i.e. upon entering the bcc phase field in the preceding heating run) and thus no arrays of synchro-Shockley partial dislocations, able to perform the phase transformation, are initially present upon cooling, implying that the dislocation structure necessary for performing the phase transformation during the 8th measurement (cooling) run must be generated and thus the phase transformation occurs at higher undercooling. During subsequent heating (9th measurement run) the DTA peak rises more steeply and at lower temperature than in the previous (7th) heating run. This reflects the differences in the dislocation microstructures of the specimen in the 7th and 9th (heating) runs, i.e. a new dislocation microstructure has developed after entering the bcc phase field in the 7th heating run. The peak in the subsequent cooling run (10th measurement run) occurs (again) at smaller undercooling (as compared to the 8th measurement run) since the dislocation structure for establishing the C14→C36 transformation is available in the specimen. This new dislocation structure differs slightly from that of the compressed specimen (6th and earlier cooling runs) and the uncompressed specimen (cooling run; solid line in Figure 6.2b) and thus also the peak shape and position of the 10th measurement run differ slightly from cooling runs before the 6th cooling run.

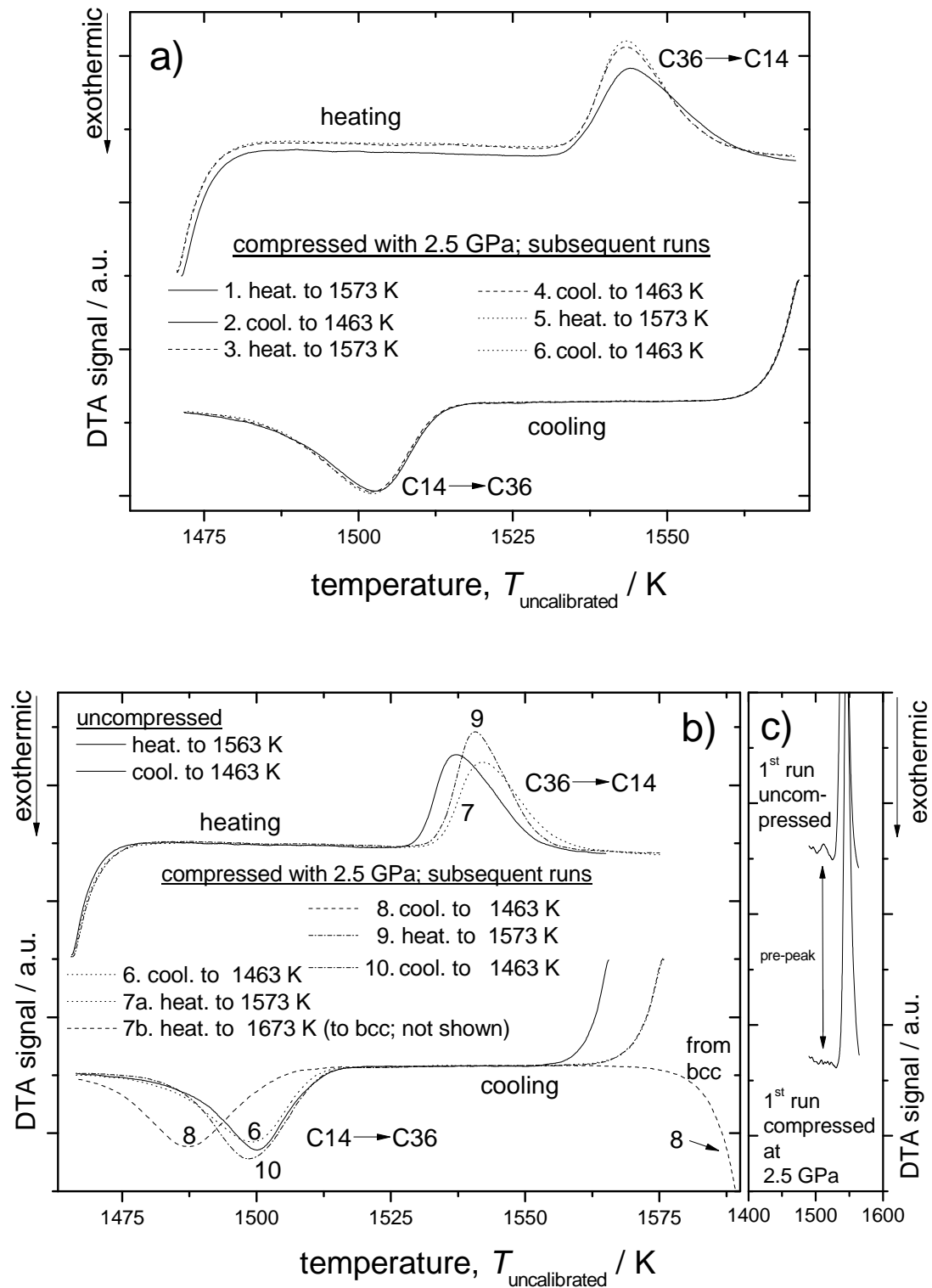**Figure 6.2:** Raw DTA measurement data of the uncompressed specimen (solid lines in Figure 6.2b) and the specimen compressed at 2.5 GPa. a) measurement runs 1-6; b) measurement runs 6-10. c) Enlargement of the pre-peak of the first heating run of the compressed specimen and of the uncompressed specimen; note that in the uncompressed specimen a small pre-peak occurs [8] (all curves pertain to a heating/cooling rate of 20 K/min).
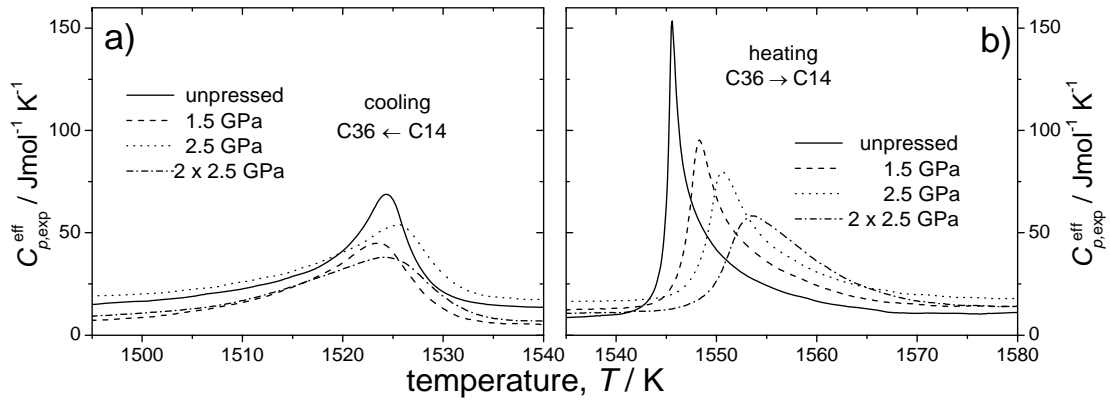
Figure 6.3: Calibrated and desmeared DTA curves as observed upon cooling (b) and heating (a) for the uncompressed specimen and the differently compressed specimens (all curves pertain to a heating-/cooling rate of ± 20 K/min).

From the calibrated and desmeared DTA measurement curves of the uncompressed specimen and the compressed specimens the absolute values of the phase-transformation enthalpies $\left|\Delta H_{tot}\right|$ (Table 6.1) were determined (as averages from the absolute enthalpy changes upon heating and cooling) as well as the transformed fractions f as a function of temperature T (see Figure 6.4; for details about the calculation procedure, see Ref. [8]).

The determined absolute values for the phase-transformation enthalpy decrease with increasing compressing stress (cf. Table 6.1). This suggests that the compressed specimens do not transform to 100 %, i.e. in the case of the specimen compressed at 2.5 GPa approximately 13 % of the specimen has not transformed (this conclusion presupposes a constant transformation enthalpy). This suggests that the *dislocations* induced by compressing constrain/inhibit the available dislocation dipoles to some extent and thus the transformation occurs incompletely.

Table 6.1 Absolute values for the phase-transformation enthalpies, $\left|\Delta H_{\text{tot}}\right|$, as obtained from the DTA curves (mean values and standard deviations calculated form the absolute values obtained for heating and cooling), and values for the activation energy for growth, Q, as determined according to the modular approach as function of the compressing stresses exerted on the specimens.

$\dfrac{\text{Stress}}{\text{GPa}}$	0	1.5	2.5	2 x 2.5
$\dfrac{\left\|\Delta H_{\text{tot}}\right\|}{\text{Jmol}^{-1}}$	567 ± 20	539 ± 9	489 ± 9	493 ± 10
$\dfrac{Q_{\text{heat.}}^{\text{C36} \to \text{C14} \ *}}{\text{kJmol}^{-1}}$	93	93	93	93
$\dfrac{Q_{\text{cool.}}^{\text{C14} \to \text{C36} \ *}}{\text{kJmol}^{-1}}$	106	109	108	110

* The difference of the activation energies of the phase transformations occurring upon heating and cooling are explained by the different c/a lattice-parameter ratios of the C14 and C36 phases ([8]/Section 5).
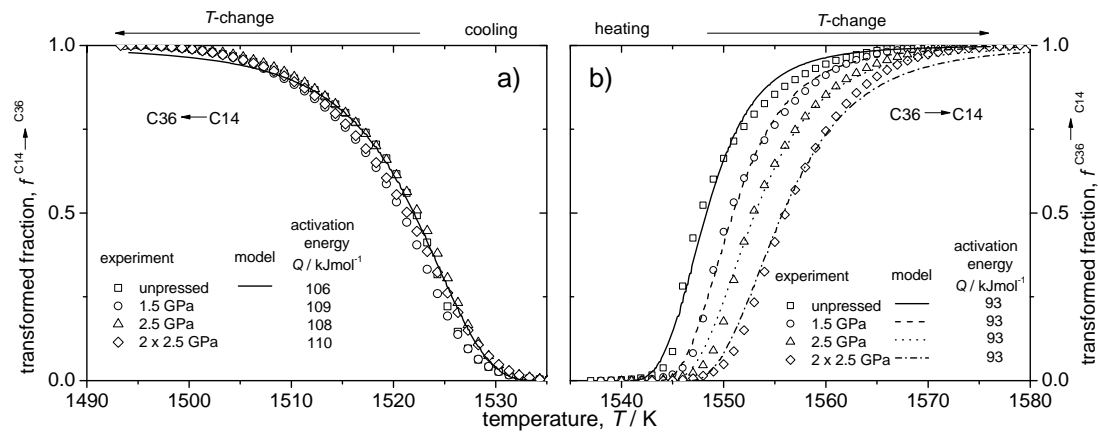

Figure 6.4: Comparison of the experimentally determined transformed fraction $f_{\text{exp}}\left(T(t)\right)$ and the transformed fraction $f_{\text{model}}\left(T(t)\right)$ obtained by fitting the kinetic model [8] to the transformation curves recorded for the specimens compressed under different conditions. All curves shown were measured with a heating-/cooling rate of ± 20 K/min. For the phase transformation occurring upon cooling the transformed fraction of the model calculation $f_{\text{model}}\left(T(t)\right)$ is only shown for the uncompressed specimen. The activation energies obtained by fitting the kinetic model to the experimental transformation curves have been listed in the figure (see also Table 6.1).

6.3.3 Modelling of the kinetics

The phase-transformation start temperature T_{start} is the temperature at which a detectable amount of the new phase is formed, i.e. the temperature at which the largest arrays of synchro-Shockley partial dislocation dipoles in the crystal become able to glide [8]. The initial compressing considerably influences the kinetics of the phase transformation occurring upon heating (i.e. the C36$\to$C14 phase transformation), whereas the reverse phase transformation occurring upon cooling is not affected to a similar extent

(see Figures 6.3 and 6.4). The temperature T_{start} for the forward (C36→C14) trans-formation occurring *upon heating* increases significantly with increasing applied com-pressing stress. This can be explained on the basis of the arrays of synchro-Shockley partial dislocation dipoles performing the phase transformation [8]: Depending on the heights of the arrays of dislocation dipoles, quantified by the variable n (correspond-ing with the number of layer-sandwich units n comprised by an array), the arrays of synchro-Shockley partial dislocation dipoles become able to glide at a certain tempera-ture, without overcoming an energy barrier by thermal activation [8]. The larger the height of the dislocation array, i.e. the larger n, the lower the required overheat-ing/undercooling ΔT in order that this dislocation dipole array starts to produce a product-phase particle by glide. In a crystal a distribution of sizes n of the arrays of perfect dislocation dipoles is expected. As discussed in Section 6.3.1, compressing generates perfect synchro dislocations of a certain Burgers vector. Such plastic defor-mation at room temperature can cause that in particular large (i.e. of large n) pre-existing arrays of synchro-Shockley partial dislocation dipoles, in the C36 phase, are fragmented. The *probability* of finding a dislocation-dipole array of large n may thus decrease with increasing applied compressing stress. Hence, because smaller arrays (i.e. of smaller n), become operative at larger overheating (see above), the temperature T_{start}, at which the C36→C14 phase transformation commences, increases with in-creasing compressing stress (see Figures 6.3 and 6.4).

For the backward (C14→C36) phase transformation occurring *upon cooling* the phase transformation start temperature, T_{start}, was hardly affected by the initial compression. This means that the (distribution of) heights n of the arrays of disloca-tion dipoles, which drive that phase transformation, are largely not affected by the compression (applied before heating). Arrays of synchro-Shockley dislocation dipoles performing the C36→C14 transformation upon heating pile up at grain boundaries or by impingement with other growing (C14) particles within a grain. Thereby, in many cases, the original (i.e. before deformation) height of the arrays is re-established. Dur-ing cooling, for establishing the backward C14→C36 transformation, the dislocations return to their starting position: The phase transformation is not finished until the dis-locations have reached their starting position (memory effect), which means that the heights of the arrays decreases during cooling (C14→C36 transformation) to the ini-tial (i.e. after deformation, before heating) height of the arrays. Hence, the phase trans-

formation start temperatures T_{start} of both the C36→C14 transformation and the C14→C36 transformation do not change during subsequent runs (see Figure 6.2a; measurement runs 3-6).

Based on the recently developed modular model [8-10] for the kinetics of the C36⇄C14 phase transformations of the TiCr$_2$-Laves phases, the experimental data shown in Figure 6.4 were fitted as function of temperature and time by this model for f [8]. For the calculations the composition-dependent interfacial energy σ was estimated for the present alloy composition by linear extrapolation using data from Ref. [8] to be $0.14 \times 10^{-3} \, \mathrm{Jm^{-2}}$. The pre-exponential factor for growth M_0 and the total number N_{tot} of pre-existing nuclei of all sizes n was estimated as in Ref. [8]. The grain size D and the degree of anisotropic impingement ξ (=1.65) were taken as determined in Ref. [8]. To describe the phase transformation occurring upon heating (C36→C14; see Figure 6.4b), the model description based on the modular approach was modified recognising that arrays of perfect synchro dislocation dipoles of large n, had been fragmented by plastic deformation.

This modification implied disregarding of the larger arrays of synchro-Shockley partial dislocation dipoles, which would become able to glide before the phase-transformation start temperature T_{start} of the compressed sample is reached, in the calculation of the transformed fraction f [8]. Consequently, as compared to the original simulations for the uncompressed state [8], during the model calculations a threshold value of (maximum) array height n was allowed to vary. Above this threshold value the arrays were assumed to be destroyed (fragmented) by the plastic deformation and were not considered as nuclei during the model calculations. As compared to the uncompressed state, this threshold value of n leads to an increased T_{start} (larger overheating). The threshold array height n was varied until the best fit to the experimental data was obtained. Thus the threshold value of n, or alternatively T_{start}, takes the role of an additional fit parameter for the compressed specimens.

As a result of the fitting it was found that the activation energies for growth for the phase transformations occurring upon heating and cooling are not significantly affected by the compression, i.e. they are equal to those of the uncompressed specimen (see Table 6.1 and Figure 6.4). This result can be understood because dislocation glide is rate controlled by moving kink pairs along the dislocation line [23] and this process is not influenced by the preceding compression.

6.4 Conclusions

A direct correlation of the density of synchro dislocations and the (kinetics of the) polytypic phase transformations in Laves phases was established: The deformation by preceding application of compressing stresses on the specimens strongly influences the C36→C14 phase transformation occurring upon heating. With increasing compressing stress the height n of the (largest) arrays of synchro dislocation dipoles decreases, and thus the overheating necessary for glide of the arrays of synchro-Shockley partial dislocation dipoles increases. Compressed specimens do not transform to 100 %, i.e. the total transformed fraction decreases with increasing compressing stress.

The (backward) C14→C36 transformation occurring upon cooling is not affected by the initial compression because (i) the arrays of synchro-Shockley dislocation dipoles performing the (forward) C36→C14 transformation upon heating have piled up at grain boundaries and by impingement within the grains, thereby restoring the initial (before deformation) dislocation array heights and (ii) the same dislocations during the backward C14→C36 transformation return to their original (i.e. after deformation, before heating) positions thereby re-establishing the (by deformation reduced) dislocation array heights.

The activation energy for growth, rate controlled by synchro-Shockley dislocation glide, is not influenced by the preceding compression.

6.5 References

[1]   P.M. Hazzledine, P. Pirouz, Synchroshear transformations in Laves phases, Scr. Metall. Mater. 28 (1993) 1277.

[2]   K.S. Kumar, P.M. Hazzledine, Polytypic transformations in Laves phases, Intermetallics 12 (2004) 763.

[3]   C.W. Allen, K.C. Liao. Shear transformations in the Laves phase $TiCr_2$, Proceedings -ICOMAT. Boston, 1979. p.124.

[4]   K.C. Liao, C.W. Allen. Shear transformation in the $TiCr_2$ Laves phase, International Conference of Solid-Solid Phase Transformations. Pittsburgh 1981. p.1493.

[5]   C.W. Allen, K.C. Liao, Dislocation models for shear transformations, Phys. Status Solidi A 74 (1982) 673.

[6]   M.F. Chisholm, K.S. Kumar, P.M. Hazzledine, Dislocations in complex materials, Science 307 (2005) 701.

[7]   J. Aufrecht, W. Baumann, A. Leineweber, V. Duppel, E.J. Mittemeijer, Phil. Mag., accepted (2010).

[8]   W. Baumann, A. Leineweber, E.J. Mittemeijer, The kinetics of a polytypic Laves phase-transformation in $TiCr_2$, as submitted for publication (2010).

[9]   E.J. Mittemeijer, F. Sommer, Solid state phase transformation kinetics: a modular transformation model, Z. Metallkd 93 (2002) 352.

[10]   F. Liu, F. Sommer, C. Bos, E.J. Mittemeijer, Analysis of solid state phase transformation kinetics: models and recipes, Int. Mater. Rev. 52 (2007) 193.

[11]   A.T.W. Kempen, F. Sommer, E.J. Mittemeijer, Calibration and desmearing of a differential thermal analysis measurement signal upon heating and cooling, Thermochim. Acta 383 (2002) 21.

[12]   W. Baumann, A. Leineweber, E.J. Mittemeijer, Calibration and desmearing of a differential thermal analysis measurement signal - upon heating and cooling - in the high-temperature region, Thermochim. Acta 472 (2008) 50.

[13]   E.J. Mittemeijer, U. Welzel, The "state of the art" of the diffraction analysis of crystallite size and lattice strain, Z. Kristallogr. 223 (2008) 552.

[14]   G.K. Williamson, W.H. Hall, X-ray line broadening from filed aluminium and wolfram, Acta Metall. 1 (1953) 22.

[15]   R. Delhez, T.H. de Keijser, E.J. Mittemeijer, Determination of crystallite size and lattice distortions through X-ray diffraction line profile analysis, Fresenius. J. Anal. Chem. 312 (1982) 1.

[16]   A. Guinier. X-ray diffraction in crystals, imperfect crystals, and amorphous bodies. New York: Dover Publications, INC, 1994.

[17]   C.W. Allen, P. Delavignette, S. Amelinckx, Electron microscopic studies of the Laves phases $TiCr_2$ and $TiCo_2$, Phys. Status Solidi A 9 (1972) 237.

[18]   J.D. Livingston, E.L. Hall, Room-temperature deformation in a Laves phase, J. Mater. Res. 5 (1990) 5.

[19]   P.M. Hazzledine, Twinning by synchroshear in the cubic laves phase, Twinning in advanced materials (1994) 403.

[20]   J.D. Livingston, Laves-phase superalloys?, Phys Status Solidi 131 (1992) 415.

[21]   Y. Liu, J.D. Livingston, S.M. Allen, Defect structures and nonbasal slip of C36 Laves phase $MgNi_2$ in a two-phase alloy, Metall. and Mater. Trans. A 26 (1995) 1441.

[22]   K.C. Chen, Chu, F., Kotula, P.G., Thoma, D., $HfCo_2$ Laves phase intermetallics - part II: elastic and mechanical properties as a function of composition, Intermetallics 9 (2001) 785.

[23]   J.P. Hirth, J. Lothe, Theory of dislocations, Malabar: Mc-GrawHill, 1968.

Chapter 7

Kurzfassung der Dissertation in deutscher Sprache

7.1 Einleitung

Laves-Phasen sind vielversprechende Kandidaten für Grundkomponenten zur Entwicklung neuer *metallischer* Materialien mit speziellen Eigenschaften. Somit sind Laves-Phasen eine aufstrebende Materialklasse, welche mit den Eigenschaften von kommerziellen Materialien konkurriert. Im Vergleich zu den meisten kommerziellen Materialien sind Laves-Phasen jedoch bislang unzureichend verstanden.

Die bekanntesten Kristallstrukturen, in welchen Laves-Phasen auftreten können, lassen sich als Stapelvarianten von verschiedenen Stapelschichten beschreiben (Polytypen); in der Literatur wurde vorgeschlagen, dass die temperaturabhängigen Phasenumwandlungen zwischen den unterschiedlichen Polytypen durch einen *synchroshear* (synchrone Scherung) Mechanismus realisiert werden. Dieser Mechanismus beruht auf der simultanen Bewegung von Shockley Partialversetzungen. Um die Eigenschaften dieser neuen Materialklasse gezielt einzustellen, ist es zwingend erforderlich, den Mechanismus und die Kinetik der Phasenumwandlungen zwischen den unterschiedlichen Polytypen zu verstehen. Folglich ist die Erforschung der Phasenumwandlungen in Laves-Phasen von großer technologischer Bedeutung, aber auch aus wissenschaftlicher Sicht äußerst interessant.

Das Ziel dieser Arbeit ist die Untersuchung der Phasenumwandlungen in Laves-Phasen, dazu wird insbesondere die $TiCr_2$ Laves-Phase als Modellsystem benutzt. Das Ti-Cr System eignet sich sehr gut als Modelsystem, da in diesem System die drei bekanntesten Laves-Phasen Polytypen als Funktion der Temperatur auftreten. Des Weiteren sind die Phasenumwandlungstemperaturen im Vergleich zu anderen Laves-Phasen vergleichsweise *niedrig*, wodurch ein relativ guter experimenteller Zugang gegeben ist.

7.2 Kalibrierung und Entschmierung eines Differenz-Thermoanalyse Messsignals – während Heizen und Kühlen – im Hochtemperaturbereich

Das zweite Kapitel dieser Dissertation behandelt experimentelle Weiterentwicklungen im Bereich der Differenz-Thermoanalyse DTA, dieser Fortschritt war notwendig um die quantitative Untersuchung der $C36 \rightleftarrows C14$ Phasenumwandlung in $TiCr_2$ Laves-Phasen zu ermöglichen.

Für die quantitative Untersuchung der Reaktions-/Umwandlungskinetik mittels DTA ist eine Temperatur- und Wärmekapazitätskalibrierung unumgänglich. Zusätzlich muss das Messsignal entschmiert werden, da es aufgrund einer (instrumentell bedingten) thermischen Verzögerung verschmiert ist (siehe Abbildung 7.1 linke Seite). Die Verschmierung wirkt sich sowohl auf die Peakposition als auch auf die Peakform aus.

Aus diesem Grund wurde in Kapitel 2 eine bereits bekannte Kalibrier- und Entschmiermethode für ein DTA Gerät erfolgreich weiterentwickelt, sodass sie im Hochtemperaturbereich angewendet werden kann (bis zu 1570 K).

Die Methode erfordert die Kenntnis von physikalischen Parametern eines Wärmeflussmodells, welches den Wärmefluss im DTA Gerät beschreibt. Diese Parameter wurden mittels einer Kalibrierung bestimmt. Als Kalibriermaterialien wurden Molybdän (zeigt eine gleichmäßige Änderung der spezifischen Wärme mit der Temperatur) und Kobalt (zeigt eine nicht-monotone Änderung der spezifischen Wärme während der ferro- zu paramagnetischen Umwandlung und umgekehrt) verwendet. Der Übergang vom ferro- zum paramagnetischen Zustand in Co wurde verwendet, da dieser Übergang keine Temperaturhysterese aufweist, und somit die Curietemperatur unabhängig von der Heiz- bzw. Kühlrate ist.

Das Ergebnis der Kalibrier-/Entschmiermethode ist die molare Wärmekapazität von Co, $C_{p,\text{Co}}$, als Funktion der Temperatur (siehe Abbildung 7.1 rechte Seite). Wie in Abbildung 7.1 (rechte Seite) gezeigt führt die „Entschmierung" zu einem Aufeinanderfallen der Kurven der unterschiedlichen Heiz- und Kühlraten. Somit tritt, wie es für solch eine Umwandlung zu erwarten ist, keine thermische Hysterese auf.
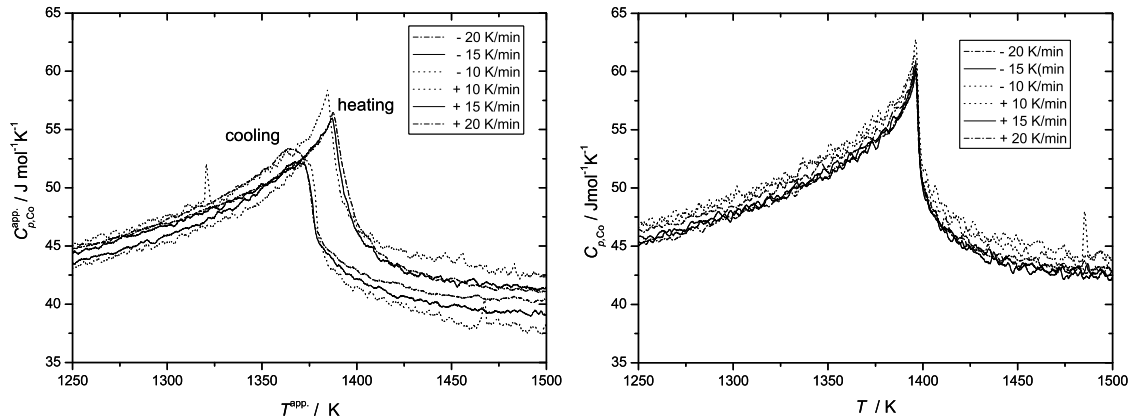
Abbildung 7.1: Links: Scheinbare molare Wärmekapazität von Co, $C_{p,Co}^{app.}$, für drei unterschiedliche Heiz- und Kühlraten. Rechts: Molare Wärmekapazität von Co, $C_{p,Co}$, für drei unterschiedliche Heiz- und Kühlraten nach der Korrektur der thermischen Verschmierung gemäß des Wärmeflussmodells.

7.3 Stapelfehler in C36 Nb-Cr und Ti-Cr Laves-Phasen und ihr Zusammenhang mit den polytypen Phasenumwandlungen

In Kapitel 3 dieser Dissertation wurden Unregelmäßigkeiten in den Stapelfolgen in C36 Laves-Phasen ($TiCr_2$, $NbCr_2$, $NbCo_2$) systematisch mittels Transmissionselektronenmikroskopie und Röntgendiffraktometrie analysiert. Es wurde festgestellt, dass die untersuchten C36-$NbCr_2$ und C36-$TiCr_2$ Laves-Phasen charakteristische Unregelmäßigkeiten in den Stapelfolgen aufweisen (siehe Abbildung 7.2 für Unregelmäßigkeiten in den Stapelfolgen in C36-$TiCr_2$ Laves-Phasen). Diese charakteristischen Unregelmäßigkeiten in den Stapelfolgen in C36-$NbCr_2$ und C36-$TiCr_2$ konnten eindeutig mit einer vorangehenden polytypen 2H (C14)$\rightarrow$4H (C36) Phasenumwandlung, welche durch das Gleiten von periodisch angeordneten synchro-Shockley Partialversetzungsdipolen realisiert wird, in Verbindung gebracht werden.

Die beobachteten Unregelmäßigkeiten in den Stapelfolgen konnten als Abweichungen von solch einer „perfekt periodischen Gleitung" identifiziert werden. Bildlich gesprochen hinterlassen die synchro-Shockley Partialversetzungsdipole einen *Fingerabdruck* im Material, der sich in den charakteristischen Stapelfehlern widerspiegelt.

Im Gegensatz dazu wurde in der C36-$NbCo_2$ Laves-Phase diese Art von Stapelfehlern nicht beobachtet. Das kann darauf zurückgeführt werden, dass während der Bildung der C36-$NbCo_2$ Laves-Phase keine 2H (C14)$\rightarrow$4H (C36) Phasenumwandlung auftritt.

Somit konnte der in der Literatur für die C14 $\rightleftarrows$ C36 Phasenumwandlung vorgeschlagene Mechanismus, welcher auf Gleitung von geordneten Reihen von synchro-Shockley Partialversetzungsdipolen beruht, bestätigt werden.
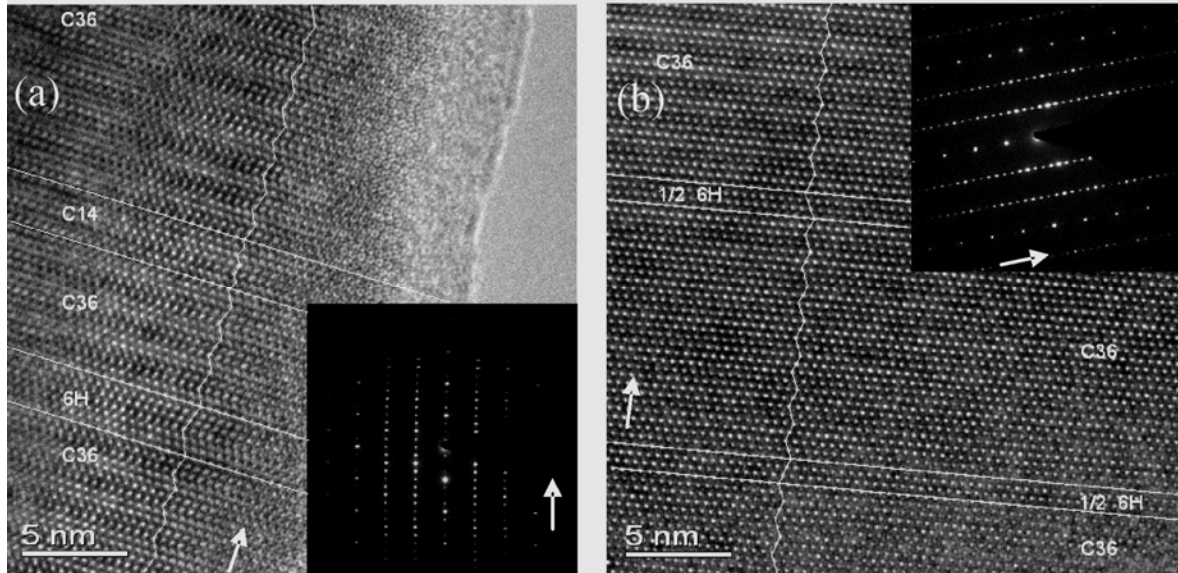

Abbildung 7.2: Hochauflösende Transmissionselektronenmikroskop Bilder (C36 Zonenachse: $\langle 11\bar{2}0 \rangle$) von homogenisierten C36-TiCr$_2$ Proben mit Unregelmäßigkeiten in den Stapelfolgen. (a) Ein *2H-Typ* (C14-Typ) und ein *6H-Typ* Stapelfehler, (b) ein "aufgespalteter" *6H-Typ* Stapelfehler. Die Pfeile zeigen in $\langle 0001 \rangle$ Richtung.

7.4 Scheitern von Kissinger(-like) Methoden zur Bestimmung von Aktivierungsenergien von Phasenumwandlungen in der Nähe der Gleichgewichtsphasenumwandlungs-temperatur

Sehr häufig werden sogenannte Kissinger(-like) Methoden verwendet, um die Aktivierungsenergie Q von heterogenen Phasenumwandlungen zu bestimmen. In Kapitel 4 wurde gezeigt, dass die Kissinger(-like) Methoden nur dann zur Bestimmung der Aktivierungsenergien einer heterogenen Phasenumwandlung angewendet werden darf, wenn diese weit entfernt von der Gleichgewichtsphasenumwandlungstemperatur T_0 auftritt, jedoch nicht wenn die Phasenumwandlung in der Nähe der Gleichgewichtsphasenumwandlungstemperatur T_0 abläuft.

Am experimentellen Beispiel der bekannten Ordnungs-Unordnungs-Umwandlung LT$\rightarrow$HT (bei T_0) und HT$\rightarrow$LT von Ni$_3$Sn$_2$ (weit weg von T_0; dafür wurden abgeschreckte Proben verwendet; LT = Tieftemperaturphase; HT = Hochtem-

peraturphase) wurde die Gültigkeit bzw. die Ungültigkeit der mittels Kissinger(-like) Methoden für beide Phasenumwandlungen im jeweiligen Temperaturbereich bestimmten Aktivierungsenergien, aufgezeigt. Während die Kissinger(-like) Analyse für die HT→LT Phasenumwandlung weit entfernt von T_0 realistische, mit der Literatur vereinbare, Werte für die Aktivierungsenergie lieferte ($Q_{HT→LT}$ = 161 kJ/mol), ergab sich für die LT→HT Phasenumwandlung (bei T_0) ein physikalisch nicht sinnvoller, hoher Wert ($Q_{LT→HT}$ = 12600 kJ/mol).

Es konnte gezeigt werden, dass der hohe Wert für die Aktivierungsenergie eine Folge der Ungültigkeit einer grundlegenden Annahme für die Ableitung der Kissinger(-like) Methode ist. Dabei handelt es sich um die Annahme einer reinen Arrhenius Temperaturabhängigkeit der Reaktionsrate, welche in der Nähe von T_0 nicht mehr getroffen werden kann.

7.5 Die Kinetik einer polytypen Laves-Phasen Umwandlung in TiCr$_2$

In Kapitel 5 wurde eine systematische Untersuchung der Kinetik der polytypen C36 ⇌ C14 Gleichgewichtsphasenumwandlung, welche bei ca. 1545 K stattfindet, durchgeführt. Die Kalibrier- und Entschmiermethode für ein Differenz-Thermoanalyse (DTA) Gerät (Kapitel 2) ermöglichte die quantitative Untersuchung des Ablaufs dieser fest-fest Phasenumwandlung mittels isochroner DTA Messungen in der Hochtemperaturregion, sowohl während des Heizens als auch während des Kühlens.

Es wurde ein kinetisches Modell auf Basis des *modularen Ansatzes* entwickelt, welches die drei überlappenden Mechanismen (Keimbildung, Wachstum und Zusammenstoß) berücksichtigt. Es wurde gezeigt, dass die Kinetik der polytypen C36→C14 und der C14→C36 Phasenumwandlungen, auf Basis des modularen Umwandlungsmodells, unter Annahme athermischer Keimbildung und stark anisotropen grenzflächenkontrollierten Wachstums sehr gut beschrieben werden kann.

Alle Daten, die durch die Modellanpassung erzielt wurden, lassen sich mit einem Mechanismus für die Phasenumwandlungen vereinbaren, welcher auf Gleitung von geordneten synchro-Shockley Partialversetzungsdipolen beruht.

Des Weiteren wurde gezeigt, dass die Aktivierungsenergie für die Gleitung von synchro-Shockley Partialversetzungen (d.h. für das Wachstum) merklich vom Verhältnis der zugehörigen *c* und *a* Gitterparameter abhängt, das heißt je größer das "*c/a*"

Verhältnis ist, desto kleiner ist die entsprechende Aktivierungsenergie (siehe Abbildung 7.3).
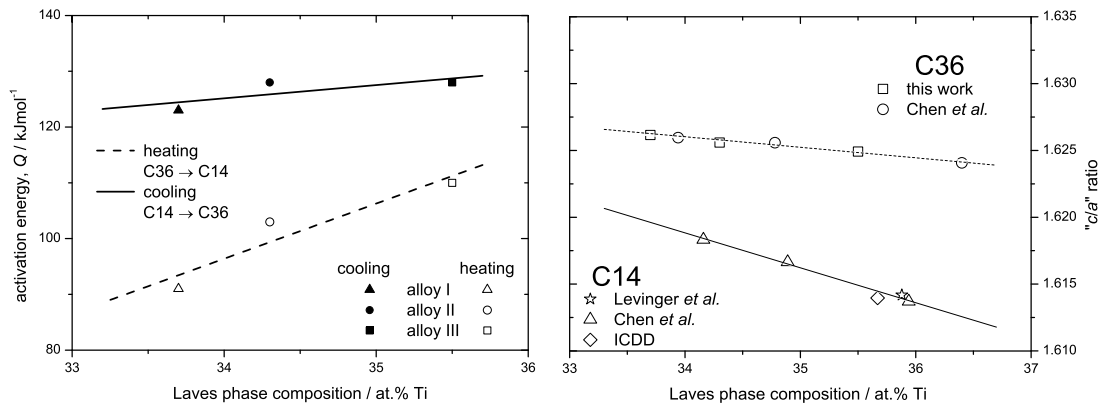

Abbildung 7.3: Links: Aktivierungsenergie der C36 → C14 und der C14 → C36 Phasenumwandlung als Funktion der Laves-Phasen Zusammensetzung. Rechts: Das „c/a" Gitterparameterverhältnis der dihexagonalen C36 und der hexagonalen C14 TiCr$_2$ Laves-Phasen als Funktion der Laves-Phasen Zusammensetzung.

Die Modellanpassung zeigte zudem, dass Grenzflächenenergie σ zwischen Ausgangs- und Produktphase mit zunehmendem Ti-Gehalt signifikant abnimmt. Die Grenzflächenenergie σ ist maßgebend für die Temperaturdifferenz zwischen der Starttemperatur der Phasenumwandlung T_{start} und der Gleichgewichtsphasenumwandlungstemperatur T_0, d.h. sie bestimmt die notwendige Unterkühlung bzw. Überhitzung, denn die Phasenumwandlung startet erst, wenn die Grenzflächenenergie durch die Abnahme an chemischer Gibbs-Energie (abhängig von der Unterkühlung bzw. Überhitzung) kompensiert werden kann.

Die Untersuchungen, die in Kapitel 6 präsentiert wurden, konnten klar aufzeigen, dass plastische Verformung die Kinetik der C36 ⇄ C14 Phasenumwandlungen beträchtlich beeinflusst. Dies konnte der Anwesenheit von synchro-Shockley Partialversetzungen, welche durch die plastische Verformung eingebracht werden, zugeschrieben werden. Die Änderung der Versetzungsdichte aufgrund der plastischen Verformung wurde mittels Röntgenlinienverbreiterung nachgewiesen.

Folglich wurde in Kapitel 6 ein direkter Zusammenhang zwischen der Versetzungsdichte und der Kinetik der polytypen Phasenumwandlungen in Laves-Phasen hergestellt. Die Anpassung des in Kapitel 5 vorgestellten Modells an experimentelle DTA Daten zeigte, dass die Aktivierungsenergie für Wachstum (für das Gleiten von synchro-Shockley Partialversetzungen) nicht durch die vorhergehende Kompression beeinflusst wird.

Chapter 8

Summary of the thesis

8.1 Introduction

Laves phases are very promising candidates as basic components for the design of new *metallic* materials with special properties. Consequently, Laves phases are an upcoming class of materials with a wide range of properties competing with commercial materials. But in comparison to (most) important commercial materials Laves phases are not well understood.

The most prominent crystal structures of Laves phases can be described by different stacking variants of layers (polytypes); in literature it was proposed that the temperature dependent phase-transformations between these polytypes occur by a *synchroshear mechanism*, which involves the cooperative, *synchronous* movement of Shockley-partial dislocations. In order to tailor the properties of *new class* materials it is necessary to understand the mechanism and the kinetics of the phase transformations between the different stacking variants since a precise tuning of materials is only feasible by the understanding of the corresponding phase transformations. Thus the investigation of the phase transformations of Laves phases is of great technological importance, but also very interesting from a scientific point of view.

The aim of this work is to study the phase transformations (kinetics) of Laves phases using in particular the $TiCr_2$ Laves phase as model system. This is a well-suited model system because of the occurrence of the three most prominent Laves phase polytypes as a function of temperature. Furthermore, the phase transformation temperatures between the Laves-phase polytypes are comparatively *low* for Laves phases. This provides a relative good experimental access.

8.2 Calibration and desmearing of a differential thermal analysis measurement signal - upon heating and cooling - in the high-temperature region

The second chapter of this thesis deals with experimental progress in the field of differential thermal analysis DTA. This progress was necessary to enable the quantitative investigation of the $C36 \rightleftarrows C14$ phase transformation in $TiCr_2$ Laves phases.

For quantitative analysis of reaction/transformation kinetics using DTA a calibration of the DTA apparatus in terms of temperature and heat capacity is inevitable. Moreover, the measurement signal has to be desmeared, since the measurement signal is smeared due to thermal lag (see Figure 8.1 left side), which affects the peak position and the peak shape.

For this reason in Chapter 2 a previously reported calibration and desmearing method for a DTA apparatus applicable to heating and cooling was successfully modified to be used in the high-temperature region (up to 1570 K). This method requires knowledge of parameters, which have a physical meaning, of a heat-flux model appropriate for the DTA apparatus. Values for these physical parameters were determined by calibration. As calibration materials Mo (exhibiting a smooth variation of specific heat with temperature) and Co (exhibiting a non-monotonic change of specific heat upon the ferro- to paramagnetic transition and vice versa) were employed. The ferro- to paramagnetic transition of cobalt was used since this transition shows no temperature hysteresis, so that the Curie temperature is heating- and cooling-rate independent.

Application of the present calibration and desmearing method based on the heat-flux model led to results for the molar heat capacity of Co, $C_{p,\text{Co}}$, as function of temperature shown in Figure 8.1 (right side). Evidently, the desmearing procedure leads to coincidence of the curves pertaining to the different heating and cooling rates. Thus an apparent thermal hysteresis of the ferro- to paramagnetic transition does not occur, as it should be.
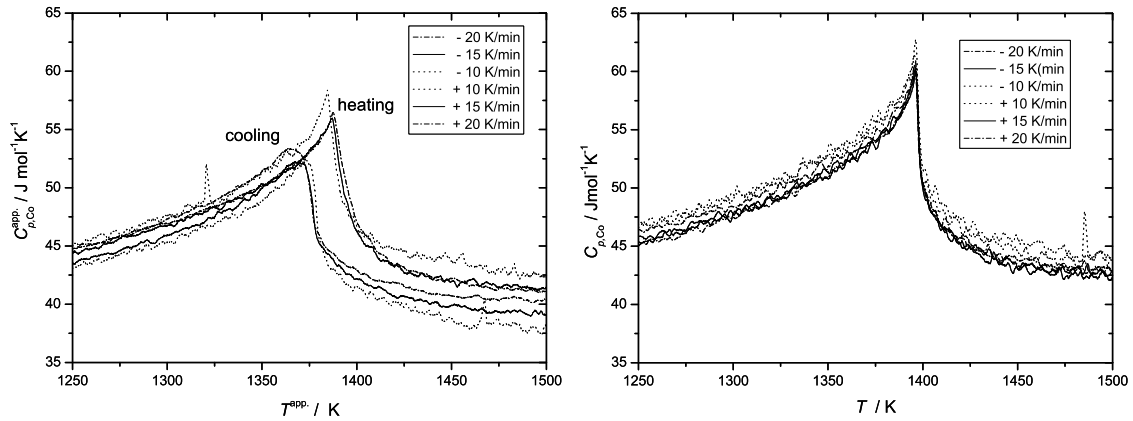
Figure 8.1: Left: Apparent molar heat capacity of Co, $C_{p,\text{Co}}^{\text{app.}}$, for three different heating and cooling rates. Right: Molar heat capacity of Co, $C_{p,\text{Co}}$, for different heating/cooling rates after correction for thermal smearing according to the heat flux model.

8.3 Layer-stacking irregularities in C36-type Nb-Cr and Ti-Cr Laves phases and their relation with polytypic phase transformations

In Chapter 3 of this thesis layer-stacking irregularities in three hexagonal C36-type Laves phases (NbCr$_2$, TiCr$_2$, NbCo$_2$) have been studied by transmission electron microscopy and X-ray powder diffraction. It was found that the investigated C36-NbCr$_2$ and C36-TiCr$_2$ Laves phases contain specific layer-stacking irregularities (see Figure 8.2 for stacking irregularities in C36-TiCr$_2$ Laves phase). These layer-stacking irregularities in both C36-NbCr$_2$ and C36-TiCr$_2$ can be associated with a preceding C14 (2H)→C36 (4H) phase transformation carried out by glide of mobile synchro-Shockley partial dislocation dipoles in an ordered fashion. The stacking irregularities observed can be interpreted as deviations from such perfect "ordered glide". In contrast with these observations, the C36-NbCo$_2$ Laves phase does not contain such layer-stacking faults. This can be ascribed to the fact that a 2H (C14)→4H (C36) transformation does not occur during formation of C36-NbCo$_2$.

Thus the proposed mechanism for the C14→C36 phase transformation by glide of a series of ordered synchro-Shockley partial dislocation dipoles ("ordered glide") was validated.
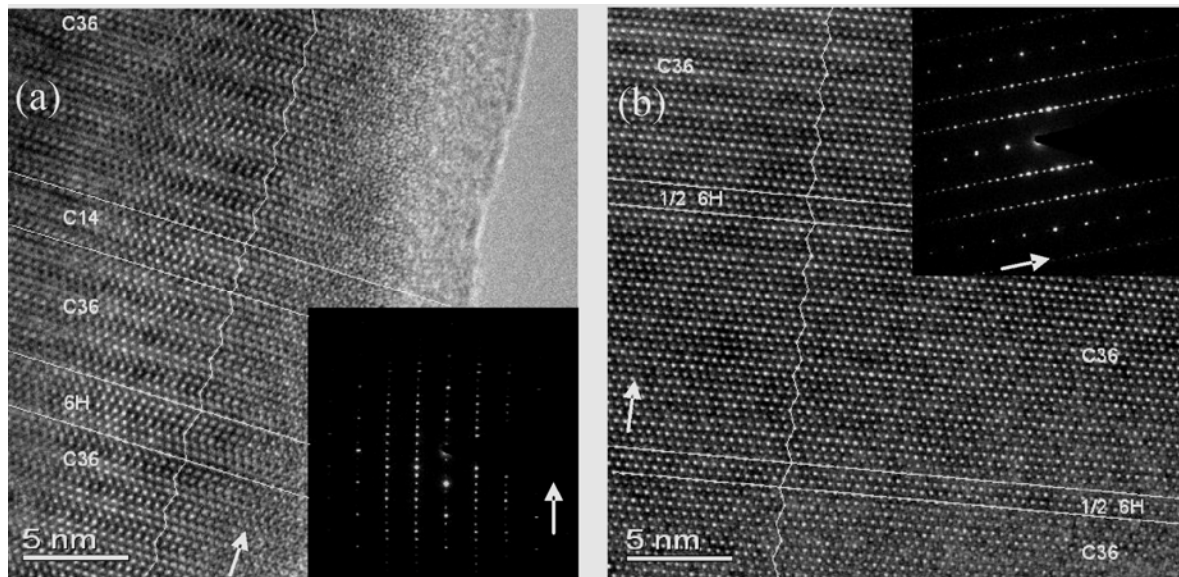
Figure 8.2: High-resolution transmission-electron microscopy HRTEM images (C36 zone axis: $\langle 11\bar{2}0 \rangle$) of annealed C36-TiCr$_2$ specimens containing stacking irregularities. (a) A *2H-type* (C14-type) and a *6H-type* stacking irregularity, (b) a "split" *6H-type* stacking irregularity. The arrows indicate the $\langle 0001 \rangle$ direction.

8.4 Failure of Kissinger(-like) methods for determination of the activation energy of phase transformations in the vicinity of the equilibrium phase-transformation temperature

The activation energies of heterogeneous equilibrium phase transformations have been frequently determined by Kissinger(-like) analysis. Chapter 4 of this work demonstrates that the applicability of Kissinger(-like) method(s) to determine activation energies of heterogeneous phase transformations is only justified if the phase transformation occurs far away from the equilibrium phase-transformation temperature T_0 but not if the phase transformation is investigated in the vicinity of the equilibrium phase-transformation temperature T_0. Experimental results on the kinetics of the order-disorder transformation in Ni$_3$Sn$_2$ obtained both near the equilibrium phase transformation temperature and considerably below it (using quenched samples) exposed the non-validity and confirmed the validity, respectively, of activation-energy values obtained by Kissinger(-like) analyses applied in the corresponding temperature ranges. Application of the Kissinger(-like) analysis in a temperature range close to the equilibrium phase-transformation temperature T_0 led to erroneous, abnormally high values for the activation energy that appear to have no physical meaning. It was shown that the un-

reasonably high activation-energy values are a consequence of non-validity of (one of) the cardinal assumption(s) made in the derivation of the Kissinger-like method and its variants, namely the assumption of a pure Arrhenius-type temperature dependence.

8.5 The kinetics of a polytypic Laves-phase transformation in TiCr$_2$

In Chapter 5 a systematic investigation of the kinetics of the polytypic $C36 \rightleftarrows C14$ equilibrium phase (shear) transformation occurring at about 1545 K was performed. The calibration and desmearing procedure for a differential thermal analysis (DTA) apparatus, as presented in Chapter 2, enabled the investigation of the progress of this solid-solid phase transformation in the high-temperature region by isochronal DTA measurements, both upon heating and cooling.

A kinetic model was developed on basis of *the modular approach*, which considers three overlapping mechanisms (nucleation, growth and impingement), where each sub-step was modelled separately. It was shown that the kinetics of the polytypic $C36 \rightarrow C14$ and $C14 \rightarrow C36$ phase transformations, can be well described on the basis of the developed modular transformation model, which adopts an athermal nucleation mode and a strongly anisotropic, interface-controlled growth mode. All data obtained by the model fitting support a mechanism for both transformations involving glide of ordered arrays of synchro-Shockley partial dislocation dipoles.

The model fitting revealed that the activation energy for glide of the synchro-Shockley partial dislocations (i.e. the activation energy for growth), depends distinctly on the ratio of the "corresponding" c and a lattice parameters. This means the larger the "c/a" ratio, the smaller the activation energy for growth (see Figure 8.3).

Furthermore, it has been found that the interfacial energy σ between product phase and parent phase decreases with increasing Ti content. The interfacial energy σ governs the difference between the start temperature of the phase transformation T_{start} and the equilibrium phase-transformation temperature T_0, i.e. the necessary overheating/undercooling: the transformation can only start if the contribution of the interfacial energy can be (over) compensated by the decrease of chemical Gibbs energy (which depends on the undercooling/overheating).
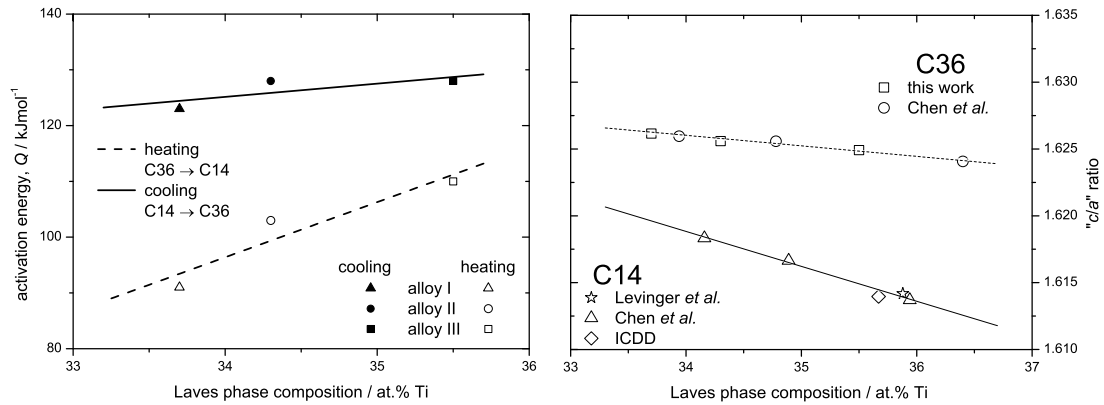
Figure 8.3: Left: Activation energy of the C36 $\rightarrow$ C14 and the C14 $\rightarrow$ C36 phase transformations as function of the Laves phase composition. Right: The "c/a" lattice-parameter ratio (see text) for the hexagonal C36 and C14 TiCr$_2$ Laves phases as function of the Laves-phase composition.

The investigations presented in Chapter 6 clearly showed that plastic deformation considerably affects the C36 $\rightleftarrows$ C14 phase-transformation kinetics of TiCr$_2$ Laves phases. This was ascribed to the presence of synchro-Shockley partial dislocations induced upon plastic deformation during compressing the samples (using a hydraulic press). The influence on the phase-transformation kinetics was shown to vary with the degree of plastic deformation, i.e. with the dislocation density as characterised by the extent of the (X-ray) diffraction-line broadening.

Thus, a direct correlation between the density of perfect synchro dislocations and the (kinetics of the) polytypic phase transformations in Laves phases was established. Fitting of the kinetic model, introduced in Chapter 5, to DTA data demonstrated that the activation energy for growth (for glide of synchro-Shockley partial dislocations) is not influenced by the preceding compression.

List of Publications

[1]   A. Kumar, U. Welzel, M. Wohlschlogel, W. Baumann, E.J. Mittemeijer, An X-ray diffraction method to determine stress at constant penetration/information depth, Berlin: Trans Tech Publications Ltd, 2006. p.13-18.

[2]   M. Wohlschlogel, W. Baumann, U. Welzel, E.J. Mittemeijer, Mechanical stress gradients in thin films analyzed employing X-ray diffraction measurements at constant penetration/information depths, Berlin: Trans Tech Publications Ltd, 2006. p.19-24.

[3]   M. Wohlschlogel, W. Baumann, U. Welzel, E.J. Mittemeijer, Determination of depth gradients of grain interaction and stress in Cu thin films, J. Appl. Crystallogr. 41 (2008) 1067.

[4]   W. Baumann, A. Leineweber, E.J. Mittemeijer, Calibration and desmearing of a differential thermal analysis measurement signal - upon heating and cooling - in the high-temperature region, Thermochim. Acta 472 (2008) 50.

[5]   J. Aufrecht, W. Baumann, A. Leineweber, V. Duppel, E.J. Mittemeijer, Layer-stacking irregularities in C36-type Nb-Cr and Ti-Cr Laves phases and their relation with polytypic phase transformations, Philosophical Magazine, accepted (2010).

[6]   W. Baumann, A. Leineweber, E.J. Mittemeijer, Failure of Kissinger(-like) methods for determination of the activation energy of phase transformations in the vicinity of the equilibrium phase-transformation temperature, Journal of Material Science, accepted (2010).

[7]   W. Baumann, A. Leineweber, E.J. Mittemeijer, The kinetics of a polytypic Laves phase transformation in $TiCr_2$, submitted, Chapter 5 of this thesis.

[8]   W. Baumann, A. Leineweber, E.J. Mittemeijer, The influence of plastic deformation on polytypic phase transformations in $TiCr_2$ Laves phases". submitted, Chapter 6 of this thesis.

[9]   W. Baumann, A. Leineweber, Solid solubility by anti-site atoms in the $C36$-$TiCr_2$ Laves Phase revealed by single-crystal X-ray diffractometry, submitted.

[10] R. Bauer, E.A. Jägle, W. Baumann, E.J. Mittemeijer, Kinetics of allotropic hcp-fcc phase transformation in Cobalt, in preparation.

Danksagung

Diese Arbeit wurde im Rahmen der institutsübergreifenden Forschungsinitiative "The Nature of Laves Phases", finanziert von der Max-Planck-Gesellschaft, am Institut für Materialwissenschaft der Universität Stuttgart und am Max-Planck-Institut für Metallforschung angefertigt. An dieser Stelle möchte ich mich bei Allen bedanken die mich bei der Anfertigung dieser Arbeit unterstützt haben und somit zum Gelingen beigetragen haben.

Zunächst möchte ich mich herzlichst bei Herrn Prof. Dr. Ir. E.J. Mittemeijer für die Möglichkeit diese Arbeit anzufertigen und somit für das mir entgegengebrachte Vertrauen besonders bedanken. Seine außergewöhnliche Betreuung der Arbeit, seine stete Unterstützung, die zahlreichen Diskussionen sowie die mir gewährte wissenschaftliche Freiheit haben wesentlich zum Gelingen der Arbeit beigetragen.

Herrn Prof. Dr. J. Bill möchte ich für die freundliche Übernahme des Mitberichts danken und Herrn Prof. Dr. T. Schleid danke ich für die Zusage, den Prüfungsvorsitz zu übernehmen.

Herrn Prof. Dr. F. Sommer gilt mein besonders herzlicher Dank. Er hat immer die Zeit gefunden mit mir in einer freundlichen Atmosphäre über wissenschaftliche Probleme zu diskutieren, dabei hatte er stets ein offenes Ohr für neue Ideen. Sein wertvoller Rat war ein entscheidender Faktor bei der Entstehung dieser Arbeit.

Weiterhin möchte ich mich herzlich bei Dr. A. Leineweber für die Übernahme der Betreuung und die Zusammenarbeit bei der Ausarbeitung der Manuskripte bedanken.

Allen Kollegen des Laves-Phasen Projektes und Mitarbeitern des Max-Planck-Instituts, besonders den Kollegen der Abteilung Mittemeijer, gilt mein besonderer Dank. Ich habe die Zeit mit meinen Kollegen sehr genossen, nicht zuletzt aufgrund der äußerst angenehmen Arbeitsatmosphäre und der tollen Zusammenarbeit. Namentlich möchte ich mich bei Thomas Meisner für die tatkräftige, unermüdliche Unterstützung bei der Probenherstellung bedanken.

Den größten Dank bin ich meinen Eltern und meiner Freundin Meike schuldig. Sie haben mich immer unterstützt und mir geholfen meine Ziele zu erreichen.

Curriculum Vitae

Persönliche Daten

Wolfgang Baumann   Geboren am 03.02.1979 in Aalen
Steigweg 7
73485 Zipplingen

Schulbildung

1985 - 1989   Grundschule Unterschneidheim - Zipplingen

1989 - 1998   Ostalbgymnasium Bopfingen
                       Abschluss: Allgemeine Hochschulreife 07/1998

Wehrdienst

1998 – 1999   Grundwehrdienst beim Transport-/Nachschubbataillon in Ell-
                       wangen

Hochschulausbildung

1999 - 2006   Studium der Werkstoffwissenschaft an der Universität Stuttgart

2005 - 2006   Diplomarbeit am Institut für Metallkunde, Universität Stuttgart
                       Thema: „Analyse von Spannungsgradienten in dünnen Schich-
                       ten mittels Röntgenbeugungsmessungen" Hauptberichter: Prof.
                       Dr. Ir. E.J. Mittemeijer

2006   Akademischer Grad: Diplom-Ingenieur

Promotion

2006 – 2010   im Rahmen der institutsübergreifenden Forschungsinitiative der
                       Max-Planck-Gesellschaft „The Nature of Laves Phases"
                       (http://laves.mpie.de) am Max-Planck-Institut für Metallfor-
                       schung, Stuttgart, Abt. Mittemeijer und am Institut für Materi-
                       alwissenschaft, Lehrstuhl 1, Universität Stuttgart Thema: „Pha-
                       se-Transformation Kinetics of $TiCr_2$ Laves Phases"

                       Hauptberichter: Prof. Dr. Ir. E.J. Mittemeijer